CORTICAL CIRCUITS FOR VISUAL PROCESSING AND EPILEPTIC ACTIVITY PROPAGATION

by

Luigi Federico Rossi

A dissertation submitted in partial fulfilment

of the requirements for the degree of

Doctor of Philosophy

Supervisor: Prof. Matteo Carandini

Department of Visual Neuroscience

University College London

I, Luigi Federico Rossi, confirm that the work presented in this thesis is my own. Where information has been derived from other sources, I confirm that this has been indicated in the thesis.

To Letizia, and my parents

Abstract

The thesis focuses on the relationship between cortical connectivity and cortical function. The first part investigates how the fine scale connectivity between visual neurons determines their functional responses during physiological sensory processing. The second part ascertains how the mesoscopic scale connectivity between brain areas constrains the spread of abnormal activity during the propagation of focal cortical seizures.

Part 1: Neurons in the primary visual cortex (V1) are tuned to retinotopic location, orientation and direction of motion. Such selectivity stems from the integration of inputs from hundreds of presynaptic neurons distributed across cortical layers. Yet, the functional principles that organize such presynaptic networks have only begun to be understood. To uncover them, I used monosynaptic rabies virus tracing to target a single pyramidal neuron in L2/3 (starter neuron) and trace its presynaptic partners. I combined this approach with two-photon microscopy in V1 to investigate the relationship between the activity of the starter cell, its presynaptic neurons and the surrounding excitatory population across cortical layers in awake animals.

Part 2: Focal epilepsy involves excessive and synchronous cortical activity that propagates both locally and distally. Does this propagation follow the same functional circuits as normal cortical activity? I induced focal seizures in primary visual cortex (V1) of awake mice, and compared their propagation to the retinotopic organization of V1 and higher visual areas. I measured activity through simultaneous local field potential recordings and widefield calcium imaging, and observed prolonged seizures that were orders of magnitude larger than normal visual responses. I demonstrate that seizure start as standing waves (synchronous elevated activity in the focal V1 region and in corresponding retinotopic locations in higher areas) and then propagate both locally and into distal regions. These regions matched each other in retinotopy. I conclude that seizure propagation respects the connectivity underlying normal visual processing.

Acknowledgements

When I embarked on PhD research, I thought that science was all about finding the right answers. My advisor Matteo Carandini taught me instead that science is about asking the right questions. Matteo nurtured my passion for beauty in scientific observations, and among many things, taught me the importance of clarity of thought and communication. For his support and mentorship, I am grateful.

I would also like to thank Kenneth Harris for his volcanic scientific exuberance. His approach constantly inspired and reminded me that knowledge of the details is key in formulating hypotheses and seeing the bigger picture.

Thanks also to my collaborators Dimitri Kullmann and Rob Wykes for sharing their outstanding expertise in translational research, and my secondary supervisor Samuel Solomon for mentoring me in crucial times along the way.

A PhD thesis might be written by a single person, but the research behind it is certainly not the task of a single man. My research would not have been possible without the remarkable expertise of all the members of the CortexLab. Particularly, I am thankful to Aman Saleem, Andrea Benucci, Michael 'Mush' Okun, and Bilal Haider - they provided an example to look up to and offered precious guidance that helped me steer my research in the right direction. A special thanks goes to Charu Reddy, whose assistance and friendship made me feel welcome in the lab from the very start. Michael Krumin, Sylvia Schroeder, Armin Lak, Nick Steinmetz, Matteo Rizzi and Daisuke Shimaoka gave me plenty of advice and experimental help on countless occasions, and I thank them for their help. I spent beautiful times working with Andrea Pisauro, Chris Burgess, Mario Dipoppa, Mika Diamanti and I-Chun Lin. Thanks to them, daily work in the lab turned into pleasant and fun memories.

I was lucky enough to share the PhD track with Archy De Berker and Francis Carpenter, two of the brightest young scientist I have met, and most importantly, two friends, who made 5 years of graduate school a great experience.

Finally, I would like to thank Letizia, for her constant support and love, and for sharing with me the daily joys and struggles of research.

Preface

This dissertation is an effort to investigate the relationship between cortical connectivity and cortical function. While linked by this common thread, the chapters fall into two distinct thematic units: each focusing on a separate research project which I conducted with the precious supervision of Prof. Matteo Carandini, starting in 2013 and continuing through 2017. As such, my goal is to keep each thematic block self-sufficient: this implies some discontinuity between the two part of the Thesis, which I hope the reader will excuse.

The first half of the Thesis investigates the principles that organise the connectivity between visual neurons and underlie their functional responses during physiological sensory processing. It comprises unpublished findings, that will be presented for the first time at the upcoming Society for Neuroscience Meeting (Rossi et al., 2017a).

This part opens with the introductory Chapter 1, that discusses the architecture of connections in the visual cortex, delineating three levels of specificity of synaptic connectivity: topographic specificity, cell-type specificity and functional specificity. In parallel, I review recent advances in neuronal recording and circuit mapping technologies and offer an outlook on how they can be used to improve our understanding of conserved neuronal connectivity rules and their relationship to the principles of cortical computation.

In Chapter 3 and Chapter 4 I present the main results of the project, which share the methods presented in the preceding Chapter 2. In Chapter 3, I describe an innovative experimental strategy to improve the success rate of single neuron initiated monosynaptic circuit tracing and combine it with volumetric two-photon imaging recordings in vivo. In Chapter 4, I deploy these methods to dissect the functional organisation of presynaptic networks upstream to L2/3 pyramidal neurons in the primary visual cortex of awake mice, and reveal a potential novel mechanism for orientation selectivity in the primary visual cortex.

The second half of the Thesis asks if the principles of cortical connectivity that constrain the flow of activity during physiological processing are respected during focal cortical epilepsy, a common neurological disorder characterised by escalating neuronal activity. This work resulted from the collaborative effort

between the laboratories of Prof. Matteo Carandini and Prof. Dimitri Kullmann, which I led with the help of Dr. Rob Wykes.

Chapter 4 bridges into this topic, and offers a perspective on how novel functional optical imaging technologies can be used to reveal the principles governing epileptic networks, from the interaction between brain areas, down to the contribution of different neuronal classes to seizure initiation, propagation and termination. I review the results of pioneering studies and outline how innovative imaging approaches will drive future investigations and help design novel therapeutic avenues.

In Chapter 6, and the adjoined methodological Chapter 5, I present the core results of the project, which are essentially identical to the paper 'Focal cortical seizures start as standing waves and propagates respecting homotopic connectivity' (Rossi et al., 2017b and two conference abstracts: Rossi et al, 2014; Rossi et al, 2013).

Finally, in the Conclusions, I sum up the two lines of research: I discuss the significance of our results, and argue that studying cortical neuronal connectivity at multiple scales is crucial for understanding physiological and pathological brain function; finally, I outline future avenues of investigation that will stem from this Thesis work.

Table of Contents

Table of figures

Chapter 1

Principles of cortical connectivity in the mouse primary visual cortex

The brain is arguably the most powerful information processing entity, capable of incredible computational feats. Even the apparently seamless act of reading these words is in fact carried out by a hierarchy of circuits wired from billions of neurons. Sensory information is funnelled through the eyes into the brain; here the contours of letters are extracted and combined into shapes, words are formed and their significance is retrieved from memory, old concepts are combined to discern new meaning and the decision to keep reading or not is finally taken. Such a complex task is mostly impenetrable to most modern artificial intelligences, but hopefully not to the reader.

Within the brain, the cerebral cortex is the structure that is believed to support our complex cognitive abilities. It is composed by interconnected sensory, associative and motor areas, which together extract salient features of sensory scenes, form a unitary representation of different sensory inputs and integrate them with cognitive processes to finally generate behavioural responses. Within each area, a myriad of different neuronal types wire circuits that carry out and broadcast the result of specific computations.

Despite such overwhelming complexity, many features of the neural architecture of the neocortex appears to be conserved across cortical areas within species, and across species (Douglas and Martin, 2004; Harris and Shepherd, 2015). Neural circuits devoted to different functions share striking commonalities in their constituent cell types and in the incidence and properties of synaptic connections between them (Thomson and Lamy, 2007). These similarities suggest that complex cortical functions might have evolved by serial homology,

repurposing similar 'canonical circuits' to process multiple types of information with similar 'canonical computations'(Carandini and Heeger, 2012; Harris and Mrsic-Flogel, 2013). Hence, neuroscientists often postulate they can discover the general principles that organize the circuits at the basis of our unique cognitive abilities by dissecting the simpler structure of more tractable cortices.

In this chapter I will illustrate the current understanding of the organizing principles of cortical connectivity drawing examples from the mouse visual cortex. While vision is certainly not the mice 'forte', it is now established that the mouse visual cortex is endowed with similar functional properties to the one of higher mammals (Niell and Stryker, 2008), and that mice use vision not just for event detection, but to guide complex behaviours and discriminations (Carandini and Churchland, 2013). Moreover, the mouse visual system has received increasing attention over the years, stimulated by the advances in genetics that allowed to classify, identify and manipulate different classes of cortical neurons (Hübener, 2003). The highly selective response properties of mouse visual neurons, combined with the expansion of the neuroscience toolbox, made of the mouse visual system the prime model system to study the relationship between cortical connectivity and cortical processing (Niell, 2015).

I will discuss the architecture of connections in the visual cortex delineating three levels of complexity, or specificity (Reid, 2012): topographic specificity, cell-type specificity and functional specificity. Topographic specificity refers to the anatomical grouping of neurons with similar response properties in functional maps, defining the functional architecture of the cortex. Cell-type specificity describes the conserved neuronal types that wire cortical circuits and the statistics of connectivity between them. Functional specificity identifies rules of synaptic connectivity that only relate to the response properties of the pre- and post-synaptic neurons. While these different levels of analysis are somewhat artificial, and hugely related to each other, they offer a useful multilevel conceptual simplification to describe the principles governing cortical connectivity. In parallel, I will describe the novel neuronal recording and circuit mapping technologies that are revealing conserved connectivity rules and their

relationship to the principles of cortical computation. I will conclude by outlining the major open questions and proposing strategies to direct future research in this field.

1.1 Receptive fields properties of mouse V1 neurons

The response properties of neurons in the primary visual cortex represent perhaps the most studied and better understood stage of cortical sensory processing (Carandini et al., 2005). Decades of vision research in cats and primates has been quickly adapted toward the understanding of the response properties of visual neurons in the mouse. Despite some differences in the peripheral visual system, including the lack of the fovea and relative dominance of retino-tectal projections over the retino-geniculate pathway, the mouse visual system shares a similar basic blueprint with its homologous in higher mammals (Niell, 2015; Niell and Stryker, 2008). Visual processing starts at the retina, where photoreceptors transduce photons from the external world into neural activity. The output from retinal ganglion cells travels then to the lateral geniculate nucleus (LGN) of the thalamus and is relayed to the visual cortex, where is analysed in increasing detail by visual neurons (Hübener, 2003).

Visual neurons respond to stimuli in restricted regions of the visual field termed receptive fields (Hartline, 1937; Hubel and Wiesel, 1962; Sherrington, 1906). The receptive field (RF) is defined as the domain of sensory space where a stimulus can trigger a change in firing rate. Stimulation outside the 'classical' RF cannot evoke a response directly, although it can significantly modulate the responses to stimuli within the 'classical' RF via subthreshold effects or lateral inhibition between neurons. Within the RF, the precise spatial pattern of contrast, as well as the temporal pattern of illumination, determines if the neuronal firing will be enhanced or suppressed. Therefore, the concept of RF is often generalised to indicate not just the region of visual space where stimuli affect neuronal firing, but also to spatio-temporal structure of the stimulus within such region. However, a clear divide between 'classical' and 'extra-classical' RF is debatable: for example, the 'classical' RF size strongly depend on the stimulus contrast, and

it can be more than twice as large when measured with low contrast stimuli as oppose to high contrast stimuli (Cavanaugh, 2002).

Cortical visual neurons are classified as simple cells or complex cells, depending on the degree to which the contributions from different regions of their receptive field sum linearly (Hubel and Wiesel, 1962). Simple cells tend to sum inputs in their receptive fields linearly. Simple receptive fields are composed by one or more ON and OFF subfield. ON subfields comprise regions where a response is triggered when illumination is higher than background; in OFF subfields, instead, lower illumination enhances firing (Martinez and Alonso, 2003). Complex cells, instead, integrate their inputs non-linearly. A feature of their receptive fields is that any change in contrast will trigger a response, as if ON and OFF subfields coincided in space (Martinez and Alonso, 2003). Accordingly, visual neurons can be classified as simple or complex based on their responses to drifting visual gratings (Skottun et al., 1991). Simple cells responses are periodic, because the grating alternates perfect superposition with the ON and OFF fields to epochs of complete offset, whereas in complex cells they are steady in time. When this assay is applied to the spike responses of the neurons, it classifies simple and complex cells as distinct groups. However, in terms of the underlying synaptic inputs, V1 cells fall along a continuum, suggesting that the distinction between simple and complex may be one of degree rather than kind, and might crucially depend on spiking threshold (Mechler and Ringach, 2002; Priebe et al., 2004).

The properties of the RF determine which stimuli are best at triggering each neuron, hence defining their 'stimulus selectivity'. Visual neurons in the mouse visual cortex display the hallmark selectivity that have been characterized in cats and primates (Drager, 1975; Niell and Stryker, 2008): retinotopically localized RF (Bonin et al., 2011), linear (simple) or non-linear (complex) integration of inputs (Niell and Stryker, 2008), contrast dependency (Busse et al., 2011), selectivity for oriented edges and selectivity for directional movement of oriented edges (Sun et al., 2015), spatial and temporal frequency selectivity (Marshel et al., 2011). Despite these similarities, visual neurons in the mouse cortex have a much lower

spatial resolution: an average RF size of ~15deg, with few RF smaller than 5 deg and many can be activated by stimuli in regions as large as half the size of one hemifield (Van Hooser, 2007; Hübener, 2003).

Finally, in addition to inputs from the visual pathway, neurons in V1 also integrate feedback inputs from higher order visual cortices, different sensory or motor areas, inputs from higher order thalamic nuclei, and neuromodulatory inputs from the raphe system, the locus coeruleus and the nucleus basalis (Harris and Thiele, 2011). The functional roles of these secondary inputs in shaping visual responses are only beginning to be understood. For instance, cholinergic and adrenergic inputs change the excitability of visual neurons and are thought to be related to alertness or attention (Harris and Thiele, 2011; Reimer et al., 2016).

1.2 Functional architecture of mouse visual cortex

The orderly topographic tiling of the visual field by neuronal RF creates the hallmark functional architecture of the visual cortex: the retinotopic map (Figure 1.1a) . The centre of the RF of neighbouring neurons represent close parts of the visual field, creating a precise two-dimensional map of the visual field on the cortical surface (Bonin et al., 2011; Hubel and Wiesel, 1962). This map is preserved across the cortical layers, so that a vertical electrode penetration encounters neurons with RF in a common location (Hubel and Wiesel, 1962). Retinotopy is derived from the connectivity of retinal ganglion cells to the two-dimensional array of photoreceptors in the retina (Horton and Adams, 2005) and is preserved at every stage of visual processing up to higher visual areas (*Figure 1.1*a) (Garrett et al., 2014). Such functional organisation has suggested that neurons with similar RF are grouped into cortical columns, modular units of cortical processing.

Functional maps like retinotopy have been traditionally measured with optical imaging recordings of population activity over the cortical surface (Benucci et al., 2007; Garrett et al., 2014; Ohki et al., 2005; Tsodyks et al., 1999): such maps provide a good mean-field approximation of the functional properties of individual neurons in a cortical column. However, single cell recordings revealed that functional maps break down at the microscopic scale (Bonin et al., 2011;

Hubel and Wiesel, 1962; Reid, 2012; Smith and Häusser, 2010). While, on average, RF similarity and overlap decreases steadily with cortical distance, there is in-fact significant RF jitter at the scale of individual neuron, with RF centres deviating from the prediction of a smooth retinotopic map even by half the size of their RF (Bonin et al., 2011). The same effect has been reported in all species, and also for different functional maps like the orientation map in cat (Martin and Schroder, 2013). These measurements have suggested that, the retinotopy, and functional maps in general, might be disordered at the microscopic scale: weather such jitter results from measurement error or ontogenetic error, and if it is at all important for brain function is a matter of debate (Kaschube, 2014).

Retinotopy is the only known functional map in the mouse visual cortex (Kalatsky and Stryker, 2003; Ohki et al., 2005). Other topographical maps exist in the visual cortex of higher mammals: the iconic orientation columns group together neurons with similar orientation preference, but functional maps have been also reported for direction selectivity, ocular dominance, spatial frequency and binocular disparity. Instead, in the mouse visual cortex, neurons responding selectively to features such as orientation and direction of movement appear interspersed in a salt and pepper organisation (Ohki et al., 2005). One hypothesis for the lack of orientation columns in mice poses that the small size limits the number of neurons that can be devoted to the representation of different stimulus features (Harris and Mrsic-Flogel, 2013): if mice were to have orientation columns, there would not be enough space (i.e. enough neurons) to represent more than one orientation for each part of the visual field. On the other hand, other work suggests that clustering of functionally similar neurons, for the sake of wiring length economy, is not necessary in the small mouse visual cortex (Kaschube, 2014). Nonetheless, recent reports of a degree of vertical clustering of neurons with similar orientation tuning has been interpreted as evidence for orientation mini-columns in the mouse visual cortex (Kondo et al., 2016).

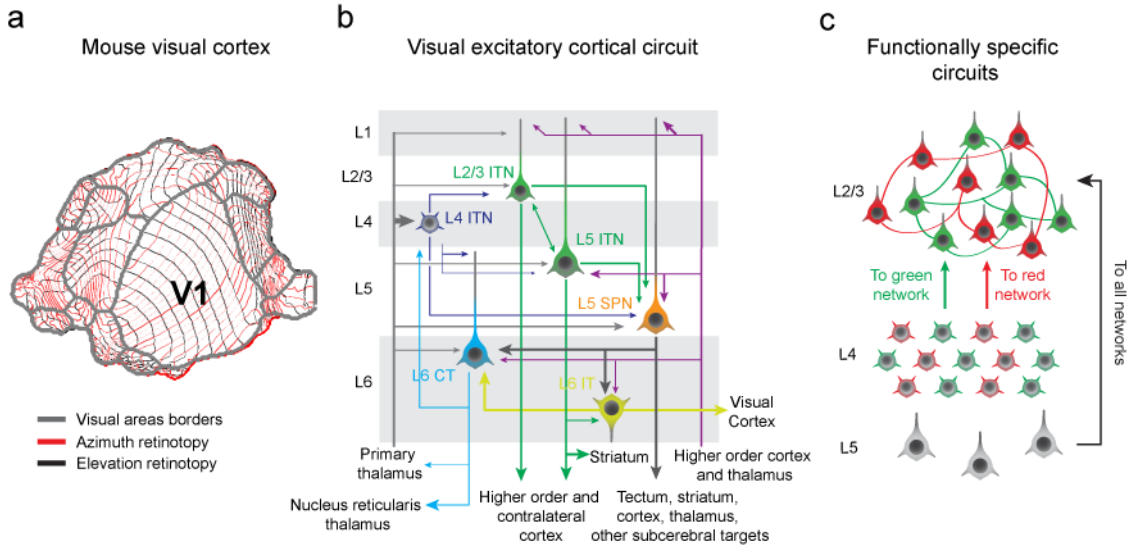

Figure 1.1: Three levels of specificity of synaptic connectivity in the mouse visual cortex. (**a**) Retinotopic organisation of the mouse visual cortex. Grey outlines represent the primary visual cortex (V1) and higher visual areas. The retinotopic map is shown as red iso-azimuth contours and black iso-elevation contours spaced by 5 degrees. (**b**) Wiring diagram of the visual cortical column. Neurons in different colour and shape represent different classes of excitatory visual neurons. Lines and arrows indicate synaptic connections; the thickness of the line indicates the strength of the connection. (**c**) Functional organisation of cortical connectivity. Excitatory connections from L4 to L2/3 and within L2/3 define functionally specific sub-networks. Excitation from L5 targets all sub-networks. Panel **a** was reproduced from Garret et al., 2014. Panel **b** was adapted and modified from Harris & Mrsic-Flogel, 2013. Panel **c** was adapted from Yoshimura et al., 2005.

The functional architecture of the cat primary visual cortex, retinotopy and orientation columns in particular, inspired Hubel and Wiesel famous hierarchical connectivity models to explain the receptive field properties of simple and complex neurons (Hubel and Wiesel, 1962; Reid, 2012). Retinotopy suggests a basic feature of cortical connectivity in the visual stream: neurons that process inputs from similar parts of the retina are likely to share similar inputs and be connected to each other. Accordingly, the Hubel and Wiesel model of simple cells posed that LGN centre-surround receptive fields arranged in a row would converge onto a simple cell whose receptive field was elongated with the same orientation. Such model was verified by several anatomical and electrophysiological studies: in the cat (Alonso et al., 2001) and in the mouse (Lien and Scanziani, 2013) such convergence happens between LGN and L4, while in

the ferret happens between L4 and L2/3 in the cortex (Mooser et al., 2004). On the other hand, orientation columns suggested that simple neurons with similar orientation and staggered RF might converge onto common postsynaptic cells to create complex cells with phase invariant representation of orientation over a larger RF (Hubel and Wiesel, 1962). While such model is yet to be confirmed by data, it certainly demonstrates how detailed understanding of the functional architecture can inform models of connectivity to explain the RF properties of single neurons.

Mesoscale functional architecture is clearly an important determinant of the connectivity of visual cortical neurons, yet it fails at explaining how visual neurons respond selectively for stimulus features that are not represented in the cortical map (Harris and Mrsic-Flogel, 2013; Ohki et al., 2005). Because the pairwise connection probability between neurons falls off with distance, the functional map is likely to bias the tuning of the local input. Accordingly, the membrane potential tuning for orientation is quite broad in the mouse visual cortex (Cossell et al., 2015; Lien and Scanziani, 2013). Nonetheless, the spiking output is still highly orientation selective. This suggests that selective tuning of excitatory neurons can occur irrespectively of whether a stimulus feature is mapped by the mesoscale functional architecture: possible mechanisms include functional specific connectivity between similarly tuned neurons, nonlinear neuronal integration, tuned inputs from the thalamus, and appropriately tuned inhibition (Haider et al., 2013; Harris and Mrsic-Flogel, 2013). Therefore, topographic connectivity cannot be the sole organising principle of connectivity in cortical columns.

1.3 Cell type specificity of cortical connections

In the visual cortex, neurons with RF localized in the same part of the visual field are organized in cortical columns, which have been proposed to form fundamental units of cortical processing (Horton and Adams, 2005; Mountcastle, 1956). Different visual columns are thought to process, largely in parallel, inputs from adjacent part of the visual space, tiling the full visual field. The wiring

diagram connecting different classes of neurons within the visual column defines how the information delivered by afferent inputs is transformed by the local circuits to yield a different representation which is then transmitted to downstream targets.

In the past 25 years, the wiring diagram of the visual column has been greatly refined with the dissection of a diverse array of cortical cell types and the incidence and properties of synaptic connections between them. Neuronal types have been classified based on the laminar organization, biophysical properties, dendritic morphology, axonal morphology and genetic profiling (Douglas and Martin, 2004; Thomson and Lamy, 2007). Entire studies have been devoted to linking together these properties and defining rules of pairwise input and output connectivity between the identified neuronal types (Jiang et al., 2015; Pfeffer et al., 2013).

Lamination in six cortical layers constitute the basic consolidated organizing principle of the cortical circuit (Douglas and Martin, 2004). Lamination suggests the simplistic, yet powerful, concept of segregation of cortical processing in separate stages, each carried out by a separate neuronal layer.

Another emerging organizing principle of neuronal circuits is their hodology (Harris and Shepherd, 2015): the specific rules of connectivity between different classes of neurons in the cortical columns. Indeed, it has been proposed that while different classes might be interspersed or segregated in different layers depending on the brain region, the connectivity rules between them may be preserved (Harris and Shepherd, 2015). The definition of cell classes is entirely an open question and intense area of research, fuelled by modern advances in genetics (Zeng and Sanes, 2017).

Finally, not all connections count the same: another important discriminant of the wiring diagram is the strength of synaptic connections between cell classes (Douglas and Martin, 2004). It has been proposed that excitatory neurons engage in two different types of synapses: ‘drivers’ and ‘modulators’. Driver synapses are strong, and can affect qualitative aspects of the RF. For instance, thalamic

synapses form just a minority of inputs onto L4 neurons, yet they provide >30% of the driving input (Lien and Scanziani, 2013). Modulatory synapses instead are weak, and can change the quantitative response of target neurons, but do not alter the qualitative RF properties.

In the following section, I will describe the current 'canonical' wiring diagram of the excitatory circuit in the mouse visual cortex (***Figure 1.1***b). Different classes of principal neurons will be placed at different nodes in such wiring diagram based on their neuroanatomical properties (lamination, dendritic and axonal morphology), weather they receive cortical or subcortical inputs, and which outputs they provide intra-cortical (intra-telenchephalic neurons, IT) or subcortical output (sub-cerebral projecting neurons SPN). Finally, I will refer to their RF field properties to highlight how visual processing changes the representation of the visual scene across the cortical column. While the rules of connectivity of inhibitory cell types provide an outstanding example of how cellular and compartmental connection specificity is crucial for neuronal computations, they will not be a matter of discussion of this thesis (for a review, see Harris and Mrsic-Flogel, 2013; Thomson and Lamy, 2007; Zeng and Sanes, 2017).

1.3.1 Canonical connectivity of excitatory V1 neurons

Principal neurons (PNs) release the excitatory neurotransmitter glutamate, usually present a somatic pyramidal shape and comprise approximately the 80% of the cortical neurons in rodents. PNs respond selectively to specific features of sensory stimuli, and their local and long-range connectivity forms the backbone of communication within and between cortical areas and hemispheres (Harris and Mrsic-Flogel, 2013). Therefore, the wiring diagram connecting PC (***Figure 1.1***b) is usually thought of as the substrate of the computations performed by the cortical column. In this view, the information delivered by afferent inputs is processed and recombined to yield a different representation of this information which is then transmitted to downstream targets (Reid, 2012). The simultaneous understanding of principal cells anatomical organization, connectivity and

functional properties promise to reveal how sensory representation are computed and transformed at each processing stage.

Layer four (L4) is usually recognized as the first stage of processing of cortical inputs, as it is the main recipients of the thalamo-cortical (TC) sensory afferents (***Figure 1.1b***) (Harris and Shepherd, 2015; Kondo and Ohki, 2015; Sun et al., 2015). Indeed, L4 is greatly expanded in the visual cortex, and other sensory areas. L4 contains two morphological subclasses of IT neurons: star pyramidal and spiny stellate cells (Thomson and Lamy, 2007). L4 IT neurons appear to be situated upstream in the local excitatory network, because they project heavily to L2/3 and also to L5, but receive little excitatory input in return (Harris and Mrsic-Flogel, 2013; Thomson and Lamy, 2007). L4 neurons are specialized for the processing of primary sensory inputs and weakly modulated by behaviour. In the mouse visual cortex, L4 is the first layer where direction and orientation selectivity emerge: L4 neurons build elongated orientation selective RF by pooling centre-surround thalamic inputs, in accordance with Hubel and Wiesel model of simple cells (Lien and Scanziani, 2013; Ya-tang et al., 2013).

L2/3 IT neurons are usually thought as the second stage of local excitatory circuit, because they receive the bulk of L4 excitation, and integrate it with multiple TC and cortico-cortical (CC) inputs (***Figure 1.1b***). In mice, PNs both in L2 and L3 receive TC sensory inputs and L4 inputs on their basal dendrites and contextual (higher thalamic and cortical) inputs on their apical dendrites (Kondo and Ohki, 2015). Interestingly, the apical dendrites receive monosynaptic connections from the neurons in the shell of the LGN, which relay inputs from direction selective retinal ganglion cells (Cruz-Martín et al., 2014; Hillier et al., 2017). L2/3 neurons send a major descending inter-laminar axonal projection that branches extensively and densely in L5, but not in L4 (Thomson and Lamy, 2007). L2/3 neurons are characterized by highly selective receptive fields and sparse firing: hence they are thought to be crucial for efficient representation of stimulus features and learning (Harris and Mrsic-Flogel, 2013).

Similarly to L2/3 IT neurons, L5 IT neurons integrate sensory signals from thalamus and L4 with higher order inputs (***Figure 1.1***b). Moreover, they are usually heavily interconnected, often bi-directionally, with L2/3 principal cells and even their projections resemble those of L2/3 IT neurons, with more connections to the striatum. However, because of their functional properties, they are placed a step further than L2/3 IT in the processing hierarchy. Indeed, L5 cells usually have larger, broadly tuned and non-linear (complex) RFs, and encode information with dense firing (Niell and Stryker, 2008). Moreover, recent reports indicate that a separate class of L5 IT, which do not project to the striatum, shows denser projection to higher visual areas, and higher stimulus selectivity (Kim et al., 2015). For these reasons, L5 IT have been proposed to convey information for image recognition to higher cortices.

L5 subcerebral projecting neurons (SPN, also known as pyramidal tract neurons in the motor cortex, PT) represent the first output stage of the local excitatory circuit (***Figure 1.1***b). These large neurons receive extensive inputs from local IT neurons of multiple layers but give little back locally(Brown and Hestrin, 2009). They receive direct TC inputs, which are strong enough to drive them even without inputs from local L2/3 IT cells. In the visual cortex, PT axons tend to be multi-projectional, branching to multiple subcerebral destinations as well as cortex, striatum and thalamus; nonetheless cortico-tectal neurons target specifically the superior colliculus (Kim et al., 2015). Even more than L5 IT neurons, L5 PT neuron fire densely and send strong 'driver' synapses. These properties have been proposed to be suited for the role of downstream elements in the local circuit: integrating the results of local computations with direct thalamic inputs and efficiently broadcasting the results, mainly to distant subcortical structures (Harris and Shepherd, 2015). Interestingly, as these neurons tend to be very direction selective, it has been proposed that they might play a role in sensory gating of movements (Kim et al., 2015).

L6 neurons are perhaps the least understood and studied. As L5, L6 contains both a class of IT neurons, and one that project outside the cortex, the cortico-thalamic neurons (CT cells) the second extra-cortical outlet of the circuit (***Figure***

*1.1*b) (Harris and Shepherd, 2015; Vélez-Fort et al., 2014). L6 IT neurons have small dendritic trees which gather >90% of the inputs locally from L5 and L6, and occasionally bizarre morphologies such as inverted somas. They have large horizontal axons that project locally and to higher order visual areas. IT neurons are broadly tuned, fire densely, receive broadly tuned input. In contrast, CT neurons, receive scarce local inputs and abundant inputs from higher visual areas. They have highly selective RF and fire very rarely. Differently from the 'driver' role of L5 PT neurons, they send weak and slow projections to the LGN and thalamic reticular nucleus (TRN), suggesting a role as 'modulators' of subcortical inputs. Consistently with this view, they feedback inhibitory projections to L4, which suppress cortical activity, suggesting a role of this layer in gain control or translaminar inhibition.

1.4 Functional specificity of excitatory cortical connectivity

1.4.1 Cortical connectivity is not random

The functional architecture and the wiring diagram of cortical columns provide a powerful framework to link the anatomy and physiology of cortical circuits. However, they fail to capture the fine scale organization of connectivity within the cortical columns. Functional architecture identifies cortical columns processing similar inputs, but the similarity in RF break down at the microscale (Bonin et al., 2011; Hubel and Wiesel, 1962), and cells with different RF properties sit close to each other (Kondo et al., 2016). On the other hand, the wiring diagram describes the statistics of connectivity between different cell classes in a probabilistic manner. However, such statistical approach might suggest that synaptic connectivity is random. This is hard to reconcile with cortex functionality, which must rely on functionally specific connections.

Connectivity among homogeneous neurons in the same layer is not random, rather organized in interlaced small networks or modules. The probability of connection among local pyramidal neurons is around 20%, and falls off with distance with a spatial constant of ~100um (Perin et al., 2011; Song et al., 2005).

In a randomly connected network, the existence of a synapse between any pair of neurons (N) is independently drawn from a uniform probability distribution (p, number of connected pairs Np, number of unconnected pairs N(1-p)^2, bidirectional pairs Np^2, triplets and so on). However, in practice, bidirectional connections appear three times more than chance; moreover, even higher order connectivity motifs are significantly enriched (Song et al., 2005). Neurons that share a connected neighbour are more likely to be connected themselves: this effect is particularly strong for neurons that receive inputs from a neighbour, rather than send input to common neighbours (Perin et al., 2011). In addition, synaptic strength seems correlated with how many connections or neighbours a pair of neurons shares (Perin et al., 2011). These results, supported by recent large scale EM network reconstruction of L2/3 (Lee et al., 2016), confirmed that the network is organised in modules that share higher connectivity within than across modules.

The fine scale organization of connections between excitatory neurons also extends across layers. Paired patch recordings combined with glutamate uncaging photostimulation demonstrated that connected L2/3 neurons share very similar inputs from L2/3 and L4. In contrast, probability of stimulating a common input was very low for unconnected pairs (Yoshimura and Callaway, 2005; Yoshimura et al., 2005). Similarity in inputs from L5 was instead found not to be dependent on connectivity. These results suggested that excitatory connections from L4 to L2/3 pyramidal cells and within L2/3 are highly specific on a fine scale, creating groups of selectively interconnected neurons, while connections from L5 could link together different functional modules (***Figure 1.1***c)(Yoshimura et al., 2005).

1.4.2 Methods for functional connectomics

'At present we have no direct evidence on how the cortex transforms the incoming visual information. Ideally, one should determine the properties of a cortical cell, and then examine one by one the receptive fields of all the afferents projecting upon that cell.' (Hubel and Wiesel, 1962).

In the discussion of their elegant 1962 article, Hubel and Wiesel wished for the advent of techniques that would trace neuronal connections between neurons and characterize the functional properties of the same neurons. The demonstration that cortical connectivity is not random prompted a field of research whose aim was to correlate physiological measurements with the probability of connections between neurons and vice versa: functional connectomics.

Functional connectomics requires at least two methodological steps (**Figure 1.2**). First, it requires characterization of the functional properties of the neurons of interest *in vivo* and with the greatest detail possible. Detailed characterization includes: position in the functional map, selectivity to relevant variables and statistics of activation during spontaneous activity. The second step requires reconstruction of the connectivity matrix between the functionally characterized neurons. Desirable supplementary measures are the genetic profiling of the recorded neurons and the measure of the synaptic strength of the connections assayed. Ultimately, the holy grail of functional connectomics is the full molecular, anatomical and functional reconstruction of the circuit.

Two-photon calcium imaging

The method of choice to record neuronal responses is two-photon (2P) *in vivo* calcium imaging (**Figure 1.2a**)(Denk et al., 1990; Svoboda and Yasuda, 2006). 2P scanning microscopy, combined with an ever-improving palette of genetically encoded calcium indicators (Lin and Schnitzer, 2016), can achieve recording from 10'000 neurons in a densely packed cortical column (Pachitariu et al., 2016), an impossible target even for the most advanced electrode array. Efforts to engineer adaptive optics and 3-photon microscopy systems are pushing this limit further, achieving two-photon recordings in the mouse hippocampus (Ouzounov et al., 2017). In addition, cranial windows can be customized with prisms (Andermann et al., 2013), GRIN lenses or periscopes (Barretto et al., 2009) to allow coronal imaging of cortical layers or recordings from deep brain structures, respectively. Recently, high speed resonant scanners have been combined with piezo-electric

scanning of the microscope objective to achieve 3D volumetric imaging of entire ~1mm^3 cortical columns (Göbel et al., 2007). Alternatively, ultra-wide field 2P microscopes allow imaging over almost an entire hemisphere of the mouse brain (Ji et al., 2016). Finally, chronic imaging from a circuit is becoming increasingly robust (Goldey et al., 2014), so that activity can be monitored for many hours over the course of weeks, allowing detailed functional and structural characterization of the recorded neurons. To tackle the size and complexity of the resulting datasets, automated pipelines for image registration, segmentation of ROIs and deconvolution of neuronal activity are also constantly improving and freely available (Pachitariu et al., 2016).

The most widely used calcium reporters are GCaMPs, a family of genetically encoded calcium (Ca^{2+}) indicators based on the enhanced green fluorescent protein (eGFP) and the calcium binding protein calmodulin (CaM)(Akerboom et al., 2012; Chen et al., 2013; Nakai et al., 2001; Tian et al., 2009). In GCaMP, the eGFP protein moiety, a beta-barrel wrapped around the chromophore, has been circularly permuted (cpeGFP), minimising structural consequences: the native C and N termini have been linked with a spacer; the beta strands of the eGFP barrel has been interrupted with an amino acid deletion, creating novel C and N termini abutting directly on the chromophore (Akerboom et al., 2009). To achieve Ca^{2+} sensitivity, the C terminus of cpeGFP was linked to a CaM domain, while the N terminus was joined with the M13 fragment of the myosin light chain kinase, which is a target of CaM (Nakai et al., 2001). In the absence of Ca^{2+}, the CaM domain does not interact with the M13 peptide: in this conformation, the C and N termini of cpeGFP grant solvent access to the chromophore, which is stabilised in its protonated form. Upon binding of four Ca^{2+}, the calmodulin domains binds the M13 fragment, triggering a conformational change that bring closer the C and N termini of cpeGFP, occluding the chromophore from the solvent and triggering un-protonation (Akerboom et al., 2009). Importantly, both isomers of GCaMP are fluorescent, either upon single or two-photon excitation. However, Ca^{2+} binding and chromophore un-protonation change the fluorescence properties of GCaMP: the calcium-bound isomer differs in excitation spectra and has increased

quantum yield (Dana et al., 2016). Such changes define the dynamic range of the indicator at each excitation wavelength, which measures the fluorescence ratio (F_{max}/F_{min}) between Ca^{2+} free and Ca^{2+} saturated samples of the indicator, under constant illumination in stationary conditions. A high dynamic range is crucial to achieve high signal to noise ratio recordings.

The capture of calcium ions by any indicator *Ind* is described by the following reaction:

$$[Ca^{2+}] + [Ind] \underset{k_{off}}{\overset{k_{on}}{\rightleftarrows}} [Ind - Ca^{2+}]$$

where k_{on} is the rate constant of binding of *Ind* and Ca^{2+} (M^{-1}/s) and k_{off} is the dissociation rate constant of the $Ind - Ca^{2+}$complex (s^{-1}). At stationary equilibrium, the number of binding and dissociation events are equal:

$$k_{on}[Ca^{2+}][Ind] = k_{off}[Ind - Ca^{2+}]$$

bearing in mind that:

$$[Ind_{Tot}] = [Ind] + [Ind - Ca]$$

the equation rearranges to:

$$\frac{[Ind - Ca^{2+}]}{[Ind_{Tot}]} = \frac{[Ca^{2+}]}{K_d + [Ca^{2+}]}$$

where $K_d = k_{off}/k_{on}$ is the equilibrium dissociation constant, measured in units of concentration (M), most commonly defined as the affinity of the indicator for its ligand.

Affinity determines how easily a fluorescent indicator captures Ca^{2+}. Simplification of this equation in the case of $[Ind - Ca^{2+}]/[Ind_{Tot}] = 0.5$ reveals that the K_d, is equivalent to the $[Ca^{2+}]$ at which half of the indicator is bound to its ligand. Noticeably, for $[Ca^{2+}] \ll K_d$, the occupancy of the indicator increases near-linearly with $[Ca^{2+}]$.

However, the equations above describe the equilibrium of an indicator with a single Ca^{2+} binding site, while CaM, the Ca^{2+} binding domain of GCaMP, bears four Ca^{2+} binding sites. Importantly, binding of Ca^{2+} to any such site triggers

conformational changes in CaM that enhance the affinity for Ca^{2+} of the remainder sites. The latter effect is termed cooperative binding: its equilibrium is approximated by the Hill equation:

$$\frac{[GCaMP - Ca^{2+}]}{[GCaMP_{Tot}]} = \frac{[Ca^{2+}]^n}{{K_d}^n + [Ca^{2+}]^n} = \frac{[Ca^{2+}]^n}{K_{ad} + [Ca^{2+}]^n}$$

where K_d is the microscopic dissociation constant (i.e. the $[Ca^{2+}]$ at which half of the binding sites are occupied), K_{ad} is the apparent dissociation equilibrium constant measured experimentally, and n is termed Hill coefficient, which quantifies the degree of interaction between the Ca^{2+} binding sites. n greater than 1 describes positive cooperative binding, whereby capture of one ligand increases the affinity of further ligand binding. Conversely, n smaller than 1 describes negative cooperative binding, whereby capture of one ligand decreases the affinity of further ligand binding. Finally, n = 1 returns a non-cooperative binding equilibrium. Increasing cooperativity yields increasingly non-linear indicator response functions to $[Ca^{2+}]$ changes, with an approximately sigmoidal relationship.

Nonetheless, calcium concentration in neurons is rarely at stationary equilibrium: hence, the kinetics of capture and release of Ca^{2+} from and indicator *Ind* are crucial to determine the rise time and decay time of the fluorescence in response to calcium changes, and ultimately, the temporal resolution each indicator is going to be able to report. Indicators with similar equilibrium affinity might differ greatly in their kinetics to reach equilibrium. Some indicators have extremely high binding rates, meaning there is very little energy needed to capture calcium, but also very high dissociation rates, meaning once the calcium is bound, the interaction is relatively weak. Other indicators have much lower binding rates, meaning it is harder for them to get into a conformation to interact with calcium, but once they do, the interaction is extremely strong so they release calcium slowly, and the dissociation rate is very low. At any given time:

$$\frac{d[Ind - Ca^{2+}](t)}{dt} = k_{on}[Ca^{2+}](t) \cdot [Ind](t) - k_{off}[Ind - Ca^{2+}](t)$$

Assuming instantaneous changes in calcium and $[Ca^{2+}] \gg [Ind_{Tot}]$, $[Ca^{2+}](t)$ can be considered constant and the equation solves to:

$$[Ind - Ca^{2+}](t) = \frac{[Ca^{2+}][Ind_{Tot}]}{K_d + [Ca^{2+}]} + A_0 e^{-t/\tau}$$

where A_0 depends on initial conditions, and the indicator response to an instantaneous change in $[Ca^{2+}]$ progresses with a time constant

$$\tau = \frac{1}{(k_{on}[Ca^{2+}] + k_{off})}$$

Because $[Ca^{2+}]$ levels in neurons are typically very low, the temporal filtering of a calcium indicator is dominated by k_{off}. Noticeably, for $t \to \infty$, the system reaches equilibrium and the solution returns the law of mass action.

To further complicate the matter, any calcium indicator will itself act as an added Ca^{2+} buffer and interfere with the dynamics of $[Ca^{2+}]$ changes (Maravall et al., 2000; Neher and Augustine, 1992; Yasuda et al., 2004). At any given time, a variation in total $[Ca^{2+}]$ can be expressed as

$$\frac{d[Ca^{2+}]_{tot}}{dt} = \frac{d[Ca^{2+}]}{dt} + \frac{d[BCa^{2+}]}{dt} + \frac{d[Ind - Ca^{2+}]}{dt} = (1 + \kappa_B + \kappa_{Ind}) \frac{d[Ca^{2+}]}{dt}$$

where B lumps together all endogenous buffers. Here, the buffer capacity (κ) represents the ratio of $[Ca^{2+}]$ sequestered by a buffer over the $[Ca^{2+}]$ that remains free upon a change in $[Ca^{2+}]_{tot}$,and depends on the indicator affinity and concentration:

$$\kappa_{Ind} = \frac{\partial[Ind - Ca]}{\partial[Ca^{2+}]} = \frac{K_d[Ind-]_{tot}}{(K_d + [Ca^{2+}])^2}$$

Increased buffer capacity, achieved for instance through a higher concentration of indicator, results in reduced fluorescent changes in response to similar $d[Ca^{2+}]_{tot}$ and smeared temporal dynamics read out (as more Ca^{2+} is sequestered and slowly released by the buffer).

The latest generation of GCaMP indicators, GCaMP6 fast and GCaMP6 slow, has been optimised for in vivo imaging of $d[Ca^{2+}]$ resulting from neuronal spikes, focusing on sensitivity to single action potential firing, high dynamic

range and fast kinetics (Chen et al., 2013). Resting $[Ca^{2+}]$ in neurons is ~40-50nM, while $d[Ca^{2+}]$ associated with single action potentials are in the order of 50-300 nM (Helmchen et al., 1996; Koester and Sakmann, 2000; Maravall et al., 2000), peaking near the somatic membrane, proximal dendrites or axonal boutons, while much smaller in distal dendrites and spines (Yasuda et al., 2004). Accordingly, GCaMP6 variants have the following properties (Chen et al., 2013):

- GCaMP6s: K_d= 144 nM; Hill coefficient = 2.9; F_{max}/F_{min}= 63; rise $\tau_{1/2}$1AP = 180ms; decay $\tau_{1/2}$1AP = 550ms),
- GCaMP6f: K_d = 375 nM, Hill coefficient = 2.3; F_{max}/F_{min}= 52, rise $\tau_{1/2}$1AP = 45ms, decay $\tau_{1/2}$1AP = 140ms).

K_ds are in the range of single action potential variations, and high cooperativity ensures that few action potentials are enough to exploit of the full dynamic range of the indicator.

High sensitivity and pronounced cooperativity of GCaMP6 variants result in responses saturation and sharp sigmoidal transfer function between $[Ca^{2+}]$ and GCaMP fluorescence: these effects complicate the estimation of the underlying firing rates and need to be taken into account when drawing comparisons between the activity recorded from different neurons (Nauhaus et al., 2012). Recordings from single wavelength Ca^{2+} indicators are typically expressed as ratios of fluorescence changes over baseline fluorescence (Maravall et al., 2000):

$$\frac{\Delta F}{F_0}(t) = \frac{F(t) - F_0}{F_0}$$

If one operates in the linear regime of the calcium indicator ($[Ca^{2+}] \ll K_d$,), $\Delta F(t)/F_0$ behaves as a robust estimator of $d[Ca^{2+}]$, which is independent of dye concentration, optical path length, excitation intensity and detector efficiency. However, when $[Ca^{2+}] > K_d$, $\Delta F(t)/F_0$ becomes a sublinear function of $d[Ca^{2+}]$, because the indicator approaches saturation. Moreover, the high cooperativity of GCaMP6 produces a steep sigmoidal transfer function, which restricts the linear regime to $[Ca^{2+}] \sim K_d$. In these conditions, $\Delta F(t)/F_0$ is very sensitive to variations in resting $[Ca^{2+}]$, which are common across neurons due to different baseline

firing rates; at the same time, also variations in $[GCaMP]_{tot}$, caused by variable transgenic expression of GCaMP6 across neuron, could result in very different readout of $[Ca^{2+}]$ dynamics due to buffering.

Tracing neuronal connectivity of functionally identified neurons

Three different strategies have been developed so far to trace the connectivity between neurons, each with his own advantages and limitations (**Figure 1.2b-d**).

The first method deploys multiple patch recordings in slices (**Figure 1.2b**) (Ko et al., 2011). After *in vivo* imaging, the imaged cortex is extracted and sliced for electrophysiological recordings. This method requires the post-hoc identification, by image registration, of the patched neurons in a structural z-stack acquired *in vivo*. Although multiple patch recordings of up to 12 neurons have been systematically achieved, the main limitation of the technique is the low yield of possible connection tested for each neuron. Moreover, slice physiology suffers from several pitfalls (Barth et al., 2016): loss of severed connections, biased toward distal ones; distance between recorded multiplets determines the spatial scale of the sampled connections; space clamp problems hide weaker connections. Nonetheless, for every recorded cell is in principle possible to obtain morphological reconstruction, biophysical characterization and genetic profiling (Petersen, 2017). Moreover, the combination with anterograde or retrograde viral tracing allows to classify neurons based on their synaptic targets or their inputs (Kim et al., 2017).

The second approach is serial electron microscopy (EM) circuit reconstruction (**Figure 1.2c**) (Bock et al., 2011; Lee et al., 2016). After *in vivo* imaging, the imaged cortex is extracted and processed in a myriad of thin sections suitable for EM imaging. The whole process is extremely demanding in terms of infrastructure, labour and time to process, image, store and trace a single sample. In order to collect three-dimensional nanoscale data from a circuit that spans hundreds of micrometres, terabytes of data need to be collected, with minimum margin of error for slice loss and annotation. Finally, the greatest challenge comes from image segmentation, which has not been fully automated yet. Nonetheless, the

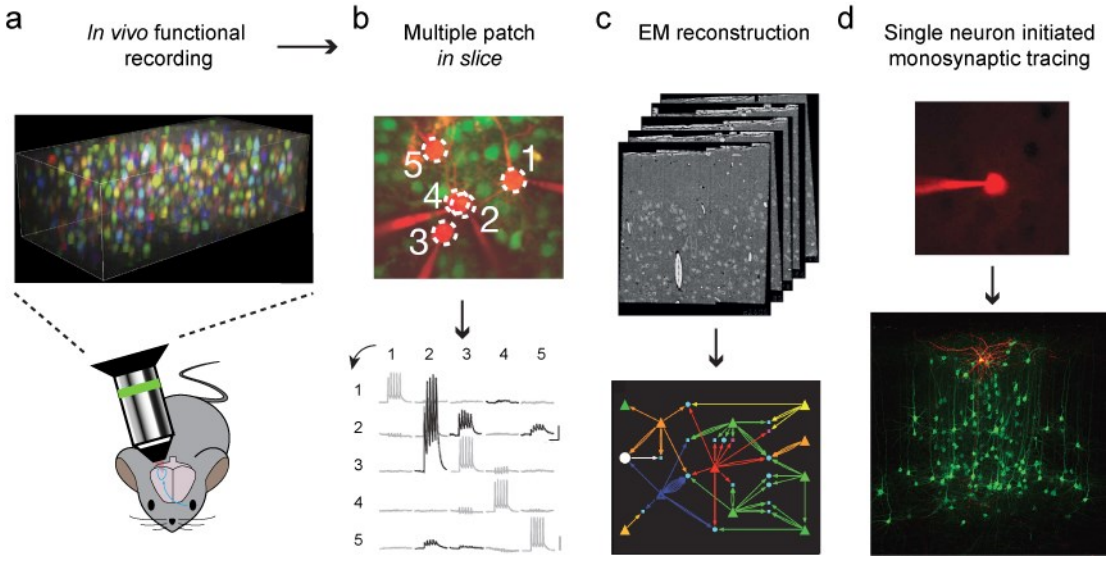

Figure 1.2: Methods for functional connectomics. (a) Two-photon imaging *in vivo* is used to characterise the response properties of visual neurons. The 3D reconstruction shows a volume imaged in V1, where each neuron is colour-coded according to its orientation selectivity. (b) Measure of connectivity by parallel multiple patch recordings in slices from the cortical volume recorded *in vivo*. Simultaneous recording of 5 identified visual neurons: the matrix shows the average postsynaptic potential traces evoked by the action potential firing in each of the neurons. Rows are presynaptic neurons, columns postsynaptic neurons. (c) Connectivity tracing by electron microscopy reconstruction. The volume imaged *in vivo* is cut in EM section and traced to recognise the imaged neurons and the number of connections between them (d) Single neuron initiated monosynaptic tracing. A single starter neuron is electroporated and tagged for tracing with a pseudotyped rabies virus. The transsynaptic spread of the virus reveals hundreds of presynaptic partners to the starter neuron. Panel **a** was adapted and modified from Kondo et al., 2016. Panel **b** was adapted from Cossell et al., 2015. Panel **c** was adapted from Bock et al., 2011 and Lee et al., 2016. Panel **d** was adapted from Judkevitz et al., 2009 and Wertz et al., 2015.

approach promises the potential to reconstruct the entire structure of a cortical circuit, mapping thousands of connections. Although it does not allow to measure synaptic strength, it grants precise morphological reconstruction, analysis of synapse number, clustering and size. However, given its limitations, up to know only two small cortical volumes have been partially reconstructed (Bock et al., 2011; Lee et al., 2016), with the resulting spatial bias in connection sampling (if an axon exits the reconstructed volume, all its connections are lost).

The last approach is single cell initiated rabies virus monosynaptic tracing (**Figure 1.2d**) (Marshel et al., 2010; Vélez-Fort et al., 2014; Wertz et al., 2015), which

allows to trace a large subset (up to several hundreds) of the inputs to a single neuron of choice (starter neuron). The starter neuron is targeted for *in vivo* transfection of three plasmids: the avian receptor TVA, the rabies virus glycoprotein oG and a fluorescent reporter (Wickersham et al., 2007a). Then a pseudotyped deletion mutant rabies virus is injected: such virus has been coated (pseudotyped) with the glycoprotein EnvA, while its envelope glycoprotein (G) gene required for trans-synaptic spread has been substituted with a reporter transgene of interest (Osakada and Callaway, 2013). At this point, the selective interaction EnvA-TVA restricts rabies virus infection to the starter cell. In the starter neuron, complementation of the G protein allows virus replication and transynaptic spread to the presynaptic partners of the starter neurons. Although limited to assay the connection of a single cell, this method traces the most connections per single neuron and is devised to fully operate *in vivo*. Moreover, when combined with the expression of GCaMP, this technique holds the promise to fulfil the wish of Hubel and Wiesel (Wertz et al., 2015). Despite the conceptual simplicity of the technique, it has proven difficult so far to apply routinely, due to the hurdles of delivering multiple genes to a single target neuron *in vivo*, complicated surgeries and due to the cytotoxicity of the rabies virus, which kills the starter cell in few days and the presynaptic neurons in a couple of weeks. However, the development of novel variants of non-cytotoxic may grant life-long stable rabies virus mediated circuit tracing and manipulation (Ciabatti et al., 2017).

1.4.3 Functionally specific networks in the mouse visual cortex

The mouse visual cortex represents the ideal model system to identify the principles of functional specific connectivity (Niell, 2015; Reid, 2012). Besides the retinotopic functional architecture, the mouse visual cortex lacks orientation columns: therefore, neurons that respond to different orientations, directions of movement and have different RF configurations are intermingled in a salt and pepper manner (Ohki et al., 2005). In this context, the generation of orientation or direction selective responses cannot rely on random pooling of local inputs, rather must be based on functional specificity of synaptic connections. Several

recent studies reconstructed the connectivity between visual neurons in L2/3 of the mouse visual cortex after recording their responses *in vivo*: the results outline some principles that organise functional synaptic specificity in the visual cortex.

First, visually driven neurons are wired into more densely connected subnetworks when compared to unresponsive units (Ko et al., 2011). Ko and colleagues recorded responses to drifting gratings and sequences of naturalistic images and classified L2/3 neurons in V1 as visually driven or unresponsive units. Then they mapped *in slice* the connections between the neurons recorded *in vivo*, and found that visually responsive neurons connected at significantly higher rate than the non-responsive ones. Accordingly, neurons that received more connections from their neighbours also displayed tighter coupling to the population activity (Okun et al., 2015). Such results indicate that strongly visually responsive neurons might form functionally relevant highly interconnected local subnetworks. Interestingly, the purpose of non-visually responsive neurons in the visual cortex remains unclear: it is unclear if these neurons are simply not activated by the paucity of stimuli classically used in experiments, or if their activity depends on the behavioural state, or anaesthesia, of the animal during the recording. The fact that they are less connected to the surrounding local population suggest that might be neurons integrating higher or contextual inputs, or form a 'reserve' pool of neurons available for plastic changes.

Most specifically, neurons with high response correlation to naturalistic stimuli connect more frequently with strong and reciprocal connections that amplify salient RF features, while most of the connection between neurons with dissimilar RF are weak synapses (Cossell et al., 2015). Building on the dataset of Ko et al., Cossel et al. observed that the distribution of pairwise correlation, synaptic strength and RF similarity between V1 L2/3 neurons are all highly skewed across the population. Accordingly, they found that the best functional predictor of synaptic connectivity was correlation of the response to natural images, closely followed by the similarity in the estimated linear RF. Surprisingly, the analysis of the of the connection strength revealed that correlations in responses to natural movies is also the best predictor of synaptic

strength, when a connection existed. Considering bidirectional connectivity only accentuated the results. Notably, most inputs had poor RF correlation with the postsynaptic cell, but a minority (~10%) of inputs carried >50% synaptic weight and strong RF correlation.

In both studies, orientation tuning similarity was reported as a significant, but much weaker, predictor of pairwise connectivity and synaptic connection strength (Cossell et al., 2015; Ko et al., 2011). Not all neurons that respond to similar orientation were connected, and a substantial amount of connections was observed among neurons with very different orientation tuning. However, the same was not observed for direction selectivity, indication that direction selectivity cannot be explained by excitatory synaptic connections in the same layer. The significant rate of connectivity between neurons with different tuning might explain the broader orientation tuning of mouse visual neurons when compared to those of mammals with orientation columns. Moreover, it also hints at a possible local circuit mechanism for feature binding in response to natural stimuli.

Surprisingly, even though pairwise noise correlations were a good predictor of connectivity (Ko et al., 2011), only weak or no correlation was found between connectivity and spontaneous correlations (Hofer et al., 2011). Interestingly, there seems to be only a weak resemblance between patterns of pyramidal cell co-activation during spontaneous activity and the structure of noise correlations during the presentation of stimuli. Moreover, even the structure of noise correlations changes under different stimulus regimes. This suggests that local connectivity does not impose a fixed structure on how population of neurons respond to sensory input: variable feedforward or top-down input might be able to regroup patterns of co-activations and shift the circuit between different modes of operation. Such configurations would allow individual neurons to participate in different ensembles, recruited to different channels or modes of cortical processing.

A recent study suggested that these principles might not generalize to connectivity across layers (Wertz et al., 2015). Wertz et al. reconstructed and recorded activity from the presynaptic network to single L2/3 starter neurons, using GCaMP6 functionalized monosynaptic rabies virus tracing. They found that the majority (70%) of the reconstructed networks were 'untuned', that is neurons did not show a significant bias toward the preferred orientation of the starter neuron. In the remaining minority of 'tuned' networks, presynaptic neurons were more likely to share similar orientation tuning with the starter cell. L2/3 neurons in all networks tended to share the orientation preference of the starter cell. Interestingly, in untuned networks, modules of neurons in L4, and to a lesser extent in L5, were also biased toward a common orientation preference: such preference however differed from the selectivity of the starter cell. The authors conclude that L2/3 neurons can receive inputs from 'feature locked' or 'feature variant' presynaptic networks. In 'feature locked' networks, local cortical synaptic input shares the same tuning of the postsynaptic neuron. In 'feature variant' networks local cortical synaptic input is organized in modules tuned to different orientation selectivity. While the functional relevance of feature-variant networks remains unclear, it certainly indicates that measurements of orientation preference alone are not a good paradigm to capture the logic of functional connectivity between visual neurons.

1.4.4 Computational relevance of functionally specific connections

Data so far suggest that mouse V1 is embedded with interconnected subnetworks of neurons that span the cortical layers and that are largely, but not exclusively, tuned for similar sensory features. What is the computational purpose such functionally specific connectivity servers for cortical processing?

A first hypothesis proposes that recurrent excitation amplifies cortical responses to salient stimulus features (Han and Mrsic-flogel, 2013). This sharpens the tuning of neurons, reduces susceptibility to noise and increases the efficiency with which they can drive downstream targets (Harris and Mrsic-Flogel, 2013). Consistent with this hypothesis, voltage clamp recordings in L4 neurons showed that the incoming orientation tuned thalamic inputs is amplified approximately

threefold by recurrent cortical excitatory connections (Lien and Scanziani, 2013; Ya-tang et al., 2013). These studies deployed *in vivo* voltage-clamp recordings in single L4 neurons, in combination with rapid and reversible silencing of cortical excitatory activity, which enabled them to isolate putative thalamo-cortical and intra-cortical components contributing to the total excitation in response to a sensory stimulus. They first demonstrated that the peak of thalamic excitation was orientation and direction tuned. Then, notably, they showed that the excitatory drive provided by intra-cortical circuitry was twice as strong and closely matched the orientation and direction tuning of thalamic excitation.

Second, recurrent excitation may allow for more complex feature integration in sensory scenes. For instance, recurrent connectivity between neurons that share the same orientation preference but receive inputs from different retinotopic locations will generate more 'abstract' receptive fields, able to respond to an oriented edge irrespective of its location in the visual field (Martinez and Alonso, 2003). Although connection probabilities are elevated between neurons of the same feature preference, substantial connectivity also exists among neurons with different feature preference. If these connections link neurons driven by features whose combination is of behavioural relevance (for example, features forming extended visual contours, corners or intersections), recurrent connectivity may allow the subnetwork to specifically amplify responses to these combinations. This hypothesis is supported by a recent study that measured the visual responses of synaptic inputs to single L2/3 V1 neurons by means of two photon imaging of calcium signals in dendritic spines (Iacaruso et al., 2017). Such inputs were on average biased toward the orientation preference of the postsynaptic cell. Interestingly, they showed that inputs representing the same orientation tended to be displaced retinotopically along the axis of their preferred orientation: such organisation would facilitate firing in response to an extended contrast edge.

Finally, recurrent excitation prolongs sensory responses. A sustained response is more robust and may allow responses to weak stimuli in the crowded visual flow to be maintained in order to interact with subsequent sensory inputs as well

as later-arriving feedback from higher-order regions. Moreover, a prolonged response provides with an extended window of synaptic integration, that could be crucial for adaptation, synaptic plasticity, and learning.

1.5 Open questions and future directions

Recent advances in physiology, connectomics and genetics are revealing the principles that organise the functional architecture of circuits of the visual cortex, how neurons that wire these circuit encode information and what computations are performed at each stage of processing. I conclude this chapter by outlining some of the major open questions to be addressed by future studies, and suggesting how emerging methods can help in this endeavour.

First, it remains unclear how the RF properties of visual neuron stem from the integration of inputs from hundreds of presynaptic neurons distributed across cortical layers. So far, technical limitations restricted the measures of connectivity to local circuits, often to a single cortical layer. Therefore, functional connectomics needs to widen its range to larger cortical volumes. Large scale EM reconstruction, optogenetically assisted circuit mapping, and novel viral tracing tools will assist in extending investigation to connections spanning all cortical layers and different brain areas.

Second, it is not known whether the presynaptic networks to visual neurons are uniform in cortical space, or if there are anisotropies, perhaps related to the postsynaptic neuron position in the functional map and to its orientation preference. It is also unclear what is the relationship between the dendritic morphology and the spatial distribution of the presynaptic inputs. While functional connectomics aims to predict connectivity from functional responses, it would be very powerful to predict the neuronal physiology based just on how the neuro-anatomical blueprint and presynaptic network are embedded in the functional map.

Third, we are still lacking a systematic categorisation of excitatory and inhibitory neuronal classes in the cortex, which display extremely diverse molecular, morphological, connectional and functional properties. Identifying

the principal dimensions underlying this complexity will require the analysis of genetic, epigenetic and developmental signatures, as well as anatomical and physiological recordings. Such intense area of research will benefit from novel high yield single cell transcriptomic approaches, large scale recordings and machine learning to discern structure in the resulting vast datasets. As our understanding of neuronal classes becomes less rudimentary, functional connectomics will need to provide the detailed input-output connectivity pattern of each cell type.

Fourth, it remains an open question how connection probability depends on long range neuronal input and output connectivity. Unpublished results (Kim et al., 2017) suggest that visual neurons that project to common higher visual area are more likely to be connected and represent similar stimulus features. However, it is still unknown how connectivity is shaped by incoming long range bottom-up and top down inputs.

Fifth, it remains an open question if the interlaced subnetworks revealed by connectomics correspond to patterns of neurons that tend to be coactive, and how such patterns of neuronal activation vary with brain state. Most of the functional connectomics studies so far measured neuronal responses under anaesthesia. It remains to be determined if neurons that are connected or share a synaptic partner are more likely to participate in the same functional assembly than neurons that are not, both during responses to sensory stimuli, but also spontaneous activity and behaviour. Indeed, driver and modulatory synapses (which are weaker but constitute the bulk of the inputs) might be weighted differently during different brain states. Answering these questions will require large scale recordings of population activity matched with large scale connectivity reconstruction.

The sixth question relates to how rules of connectivity between neurons are sculpted by experience and learning. Answering such question will require a combination of behavioural protocols and techniques to manipulate synaptic plasticity, stable long term recordings from the same neuronal population and

the development of techniques that allow repeated assessment of neuronal connectivity over time, such as optogenetically assisted connectivity mapping or self-inactivating non cytotoxic rabies viruses.

Finally, once we have a detailed description of the functional determinants of the probability of connections between neurons, the next big challenge will be to endow computational models of the visual cortex with these circuit rules to create a unified framework for testing the contribution of identified network components to the representation and transformation of visual information.

Chapter 2

Methods

All experimental procedures were conducted in accordance with the UK Animals Scientific Procedures Act (1986). Experiments were performed at University College London under personal and project licenses released by the Home Office following appropriate ethics review.

2.1 Part 1

In this section, I detail the methods used in the experiments described in Chapter 3 and Chapter 4.

2.1.1 Transgenic mice breeding

Experiments were performed on 8-12 week old female and male mice that were maintained on a 12 hours light/dark cycle. We used the following mouse lines: Camk2a-tTA; EMX1-Cre; Ai93(TITL-GCamp6f) triple transgenic mice (Madisen et al., 2015), expressing calcium indicator GCaMP6f in all cortical Camk2a-positive excitatory neurons; Camk2a-tTA; EMX1-Cre; Ai94(TITL-GCamp6s) triple transgenic mice (Madisen et al., 2015), expressing calcium indicator GCaMP6fs in all cortical Camk2a-positive excitatory neurons; Camk2a-tTA; tetO-GCamp6f double transgenic mice (Wekselblatt et al., 2016), expressing calcium indicator GCaMP6s in all cortical Camk2a-positive excitatory neurons; or in wild type C57BL6/j mice.

The final transgenics were generated from the following parental lines: Emx1-IRES-Cre, expressing Cre recombinase under the Emx1 promoter (catalog #005628, The Jackson Laboratory), driving recombination in all excitatory neurons of the neocortex and hippocampus (Gorski et al., 2002; Vanni and Murphy, 2014); CamKIIa-tta, expressing the bacterial tetracycline transactivator (TTA) under the control of the CamKIIa promoter, which drives expression in all pyramidal neurons of the neocortex; Ai93(TITL-GCamp6s) mice, carrying a copy

of the genetically encoded calcium indicator GCaMP6f in the TIGER locus, whose expression is activated by flex recombination and controlled by the tetracycline response element (TRE); Ai94(TITL-GCamp6s), analogous to Ai93 for GCaMP6s; tetO-GCamp6f mice, carrying a copy of the genetically encoded calcium indicator GCaMP6s in the TIGER (ROSA?) locus under the transpcriptional control of the TRE.

2.1.2 Surgical procedures

Using aseptic techniques, mice were implanted with a cranial window over the right visual cortex as previously described (Goldey et al., 2014).

The complete experiment entailed three surgical procedures, each carried out under isoflurane anaesthesia (1-2% in Oxygen), while the body temperature was monitored and kept at 37-38 ˚C using a closed-loop heating pad, and the eyes were protected with ophthalmic gel (Viscotears Liquid Gel, Alcon Inc.). An analgesic (Rimadyl, 5 mg/kg, SC) was administered on the day of the surgical procedure and in subsequent days, as needed. Whenever the procedure involved the direct exposure of the brain, Dexamethasone (0.5 mg/kg, IM) was administered 30 min prior to the procedure to prevent brain oedema. The exposed brain was washed and kept perfused with fresh artificial cerebrospinal fluid at all times (150 mM NaCl, 2.5 mM KCl, 10 mM HEPES, 2mM $CaCl_2$, 1mM $MgCl_2$; pH 7.3 adjusted with NaOH, 300mOsm).

The major surgery consisted of the implantation of a stainless steel headplate over the right hemisphere of the cranium. The head was shaved and disinfected, the cranium was exposed and covered with biocompatible cyanoacrylate glue (Vetbond). A stainless-steel head plate with a 7 mm round opening was secured over the skull using dental cement (Super-Bond C&B, 10 Sun Medical Co. Ltd., Japan). The exposed bone inside the chamber was covered by a thin layer of dental cement and sealed off with silicone elastomer (KwicKast). The animal was then allowed to recover for at least 4 days before further experimental procedures.

On the day of the electroporation, a 1.5-2 mm wide square craniotomy was opened over the visual cortex (centered at -3.3mm AP, 2.8 ML from bregma). The animal was then transferred to the two-photon microscope setup for the single neuron electroporation procedure. Finally, the craniotomy was sealed with a glass cranial window, attached to the skull using cyanoacrylate glue and dental cement. The window was assembled from a 3 mm diameter round cover glass cured to 1 smaller custom made glass square insert (1.5-2 mm wide, 300 um thickness) with index-matched UV curing adhesive (Norland #61).

In some animals, if the electroporation was successful, I performed monosynaptic transynaptic tracing using rabies virus. The cranial glass window was removed (Goldey et al., 2014) and a durotomy performed using a recurved insulin needle. Then, 100-200nL of EnvA-dG-dsRed-RV (~10^9 particles/ml) were injected using a pneumatic injector (Nanoject, Drummond Scientific Company) through a 30-50 µm borosilicate capillary. I targeted the injection to ~200 µmfrom the electroporated cell using a reference image of the brain vasculature. Finally, a new glass window was implanted as described before.

2.1.3 Two-photon guided single cell electroporation

The targeted single neuron electroporation procedure was adapted from published protocols for single cell electroporation *in vivo* (Judkewitz et al., 2009; Kitamura et al., 2008). *In vivo* two-photon imaging during the experiment was conducted under a Sutter-MOM two-photon microscope, equipped with a 16X high NA (0.8) water immersion objective lens (Nikon), and a femtosecond pulsed tunable laser (Chameleon Ultra II, Coherent). The microscope was controlled using ScanImage v3.8 (Pologruto et al., 2003). An epifluorescence imaging module and camera (sCMOS, PCOedge) was used to take reference pictures of the vasculature and guide the electroporation to a brain region devoid of big blood vessels.

Borosilicate pipettes (resistance 10-14 mOhm) were pulled with a vertical pipette puller (Narishige) and filled with $KMeSO_4$ based intracellular solution (133 mM $KMeSO_4$, 7 mM KCl, 10 mM HEPES, 2 mM Mg-ATP, 2 mM Na_2-ATP,

0.5 mM Na_2-GTP, 0.05 mM EGTA; pH 7.2 (adjusted with KOH), 280–290 mOsm; filtered using a 0.45 mm syringe filter). The intracellular solution also contained 50 µM of the red fluorescent dye AlexaFluo 594 and 3 plasmids with the following concentrations: 100ug/uL pCAG-dsRed2 (Addgene #15777), 200ug/uL pCMV-oG(Addgene 74288) (or pCMV-G, Addgene 15785), 100ug/uL pCAG-TVA800(Addgene 15788).

The pipette was guided to the brain surface with a micromanipulator (Luigs&Neumann) and targeted to a cortical region devoid of blood vessels. I then switched to two-photon imaging at 830 nm wavelength, suitable to excite both Alexa 594 and GCaMP6. The pipette was pushed through the dura, while applying positive pressure (~150 mBar) to prevent clogging. The diffusion of the red dye in the extracellular space counterstained neurons as 'solid' shadows; GCaMP fluorescence was used to target the pipette to excitatory cells. I monitored the resistance of the pipette with an electroporator for *in vivo* transfections (Axoporator 800A, Molecular Devices). The pipette tip was pushed on the membrane of neurons until I measured an increase in ~30% of resistance. Then I delivered a single pulse train at -12 V, 100 Hz, 0.5 ms pulse width, 1 s duration. The signature of electroporation is the immediate filling of the soma with AlexaFluo 594. I discarded from further imaging and analysis cells whose membrane was clearly pulled away when I withdrew the pipette after electroporation. Neurons were then imaged for 1-10 min, switching between 830 nm and 920 nm wavelength to measure the intracellular dynamics of GCaMP and assess the cell recovery from electroporation.

Transgene expression of electroporated cells was assessed 1-5 days after electroporation.

2.1.4 Two-photon imaging of neuronal responses

Two-photon imaging recordings of neuronal activity were performed under a resonant-scanning two-photon microscope (B-Scope, Thorlabs). Mice were head fixed and free to run on an airflow-suspended spherical treadmill during the imaging sessions. The microscope was controlled using ScanImage v4.2

(Pologruto, Sabatini, and Svoboda 2003). A low magnification (x16) high NA (0.8) water immersion objective lens (Nikon) was mounted on a piezoelectric z-drive (PIFOC P- 725.4CA, Physik Instrumente) allowing multi-plane imaging. Excitation light (920-970 nm, depending on the experiment, 30-100 mW at the sample depending on cortical depth) was provided by a femtosecond laser (Chameleon Ultra II, Coherent). Laser power was depth-adjusted and synchronized with piezo position using an electro-optical modulator (M350-80LA, Conoptics Inc.). The imaging objective and the piezo device were light shielded using a custom-made metal cone, a tube, and black cloth to prevent contamination of the fluorescent signal caused by the monitors' light.

Fields of view between 200-850µmwere imaged with a resolution of 512X512 pixels at 30 Hz. For volumetric imaging in GCaMP6s mice, I divided this frame rate across 10 simultaneously imaged planes, spaced by 15-35 microns in z, resulting on an effective sampling rate of 3Hz; instead, for GCaMP6f mice, I imaged 5 planes at a time, 15-35 microns apart in z, with an effective sampling rate of 6 Hz. For dense imaging of cortical columns, I used planes spaced 15µm and serially tiled the whole cortical depth between L2 and L5.

2.1.5 Visual stimulation

Visual stimuli were generated in Matlab (MathWorks) using the Psychophysics Toolbox (Brainard 1997; Kleiner et al. 2007) and displayed on 3 gamma-corrected LCD monitors (refresh rate 60Hz) arranged at 90 degrees to each other. The LCD screens were coated with Fresnels lenses to correct for viewing angle inhomogeneity of the LCD luminance. The mouse was positioned at the center of this U-shaped monitor arrangement at the distance of 20 cm from all three monitors so that the monitors spanned ±135 degrees of horizontal and ±35 degrees of the vertical visual field of the mouse.

We first used sparse spatial white noise stimuli to map the receptive field of the imaged area. Patterns of sparse black and white squares (4.5 degrees of visual field) on grey background were presented at 5 Hz. The probability of each square to be not grey was 2-5% and independent of other squares. For orientation tuning

experiments I presented 1 s long drifting gratings (size 30-60 degrees, contrast 100%, spatial frequency 0.05 cpd, temporal frequency 2 Hz). The position of the grating was selected to match the retinotopic location of the imaged region.

2.1.6 z-Stacks, morphological and neuroanatomical tracing

Structural z-stacks of were acquired under the same resonant-scanning two-photon microscope (B-Scope, Thorlabs) used for functional recordings. The piezoelectric z-drive was used to move the objective in steps of 1μm and image 10-500 repetitions of the same cortical volume. The range of the piezoelectric z-drive was 400 μm; to record deeper z-stack, I repeated the procedure after moving the objective 400μm down using the microscope motors.

To correct for image motion across repetitions of the same z-stack, individual imaging planes were first registered individually; then, starting from the middle of the z-stack, I re-aligned neighbouring frames to each other. Image registration was carried out using a fft-based subpixel image registration algorithm (Guizar-Sicairos et al., 2008). Finally, the red-channel of each z-stack was corrected for the bleed-through of GCaMP6 fluorescence, by subtracting a scaled copy of the green-channel: the scaling coefficient was computed with robust regression between the 20% brightest pixels of the green channel against the corresponding pixels in the red-channel.

Structural z-stack of electroporated neurons were traced using neuTube, a semi-automated neuron reconstruction software based on the SWC format (Feng et al., 2014). The resulting graphs were imported and analysed with custom software in Matlab (MathWorks). Structural z-Stack of presynaptic networks were analysed manually, selecting ROIs around the traced neurons. The resulting spatial coordinates where imported and analysed with custom software in Matlab (MathWorks). Reconstructions of starter neurons and presynaptic networks were aligned using salient reference points. Final fluorescence images were curated in Fiji (Schindelin et al., 2012).

2.1.7 Processing of two-photon data

Pre-processing of the two-photon data routinely included registration, segmentation into active region of interest (ROIs), and neuropil correction estimation. These analyses were performed in Matlab (MathWorks), using a publicly available pipeline whose details are explained in Pachitariu et al., 2016. The resulting selection of ROIs was curated manually, to distinguish active neuronal somas from spurious ROIs corresponding to dendrites, axons and blood vessels: the selection was based on the ROI morphology and the constant comparison with the matched average projection of the recorded field of view. Accordingly, traced cells expressing dsRed2 were also selected manually by inspecting the average projection of the red-channel of each acquisition.

To correct the fluorescence time-courses of each ROI from the contamination of the surrounding neuropil, I estimated a scaling factor of the neuropil trace by examining the lower envelope of the relationship between neuropil and somatic fluorescence. Then, each ROI was subtracted the scaled version of the respective neuropil trace (Peron et al., 2015). Finally, fluorescence time-courses were high-pass filtered above 0.05Hz and z-scored.

Dense volumetric imaging often resulted in the same neurons being imaged in multiple imaging planes. To exclude multiple samples of the same neurons, I combined the piezoelectric z-drive signal with calibrated measurements of the FOV size at each magnification to calculate the exact 3D position of each ROI. I considered duplicates the ROIs whose centre of mass was closer that 5min XZ and closer than 20µmin Z, and had a signal correlation in responses to drifting gratings higher than 0.5. Amongst duplicates, the ROI with higher SNR of responses was chosen for further analysis.

2.1.8 Classification of excitatory and inhibitory neurons

Functional imaging time-series were averaged to obtain high signal to noise ratio z-stacks, that were pre-processed as structural z-stacks, producing a green GCaMP6 channel, highlighting GCaMP6 expressing neurons, and a red dsRed2 channel, highlighting neurons traced by the rabies. Then, a custom semi-

automatic algorithm was used to segment and classify red cells as GCaMP6 positive or negative. The red fluorescence channel was used to segment masks of neurons of interest: first a top-hat filter was applied to correct for background inhomogeneities, adjusting the scale of the filter to enhance features of the size of neuronal somas. Then, red cells were segmented with iterative thresholding: a 'local threshold' stack was computed applying a 100 µm wide local standard deviation filter to the stack. Target features were detected as round blobs including at least a five 8-connected pixels exceeding the local pixel mean, computed in a 100 µm neighbourhood, by at least the local standard deviation scaled by a factor n; such blobs were segmented as red cells and subtracted from the processed stack. This procedure was repeated iteratively four times, gradually decreasing the thresholding factor n from 5 to 3. Finally, in a supervised step, each ROI was inspected and either accepted as a valid cell, refined to best match the red channel image, or discarded in case of false positives or out of focus cells. The centroid of each detected neuron was used to cut 100 µm wide snippets from the GCaMP6 channel, the dsRed2 channel, and to create a binary mask of the soma. Finally, the algorithm computed the whitened cross-correlation (i.e. phase correlation) map between the binary mask of each neuron and the GCaMP6 fluorescence image. Several statistics were derived from these images: the size of the central correlation peak, the standard deviation of the cross correlation values inside a 5 µm annulus around the peak, the prominence of the central peak (computed as the percentile corresponding to the central peak with respect to the rest of the pixels of the cross correlation mask), the signal to background ratio of each somatic mask in the GCaMP6 image. These statistics were used to seed a k-mean clustering to separate putative excitatory and inhibitory units.

2.1.9 Analysis of visual responses

Responses kernels to drifting gratings and sparse noise stimuli were computed by stimulus triggered average (STA). The response to each stimulus was defined by the difference between the z-scored fluorescent trace and the 20^{th} percentile of the baseline activity 1s prior to stimulus presentation. Stimulus triggered

averages and s.e.m. were obtained by averaging responses across the same type of stimuli.

For drifting gratings, responses were calculated as the integral below the response kernel in the 2 second window after stimulus onset. A neuron was defined to have a significant response to drifting grating if it had EITHER a maximum response greater than 2 times the standard deviation of the fluorescent trace measured during baseline OR if it had an OSI or DSI >0.2; moreover, it was required to pass a one-way ANOVA across stimuli, including blanks, AND a t-test of the hypothesis that the maximum stimulus response and the response to blank came from population with equal mean. The direction selectivity index (DSI) and orientation selectivity index (OSI) were defined for each neuron as the modulus of vector sum of the responses to gratings drifting at different angles. The preferred direction and orientation were defined as the angle of the vector sum of the responses to gratings drifting at different angles. Only for starter neurons, the preferred direction and orientation of motion were computed by fitting a double Gaussian tuning curve to the data.

To compute retinotopic map from sparse noise stimuli, I considered the black and white squares presented at the same position as the same stimulus. For each stimulus position, responses were calculated as the maximum of the response kernel in the 2 second window after stimulus onset. The resulting STA receptive field maps were thresholded at the 75^{th} response percentile: the weighted average of the pixels surviving thresholding was considered the preferred retinotopic position of the map.

Chapter 3

Improved methods for single cell initiated monosynaptic circuit tracing and recording *in vivo*

3.1 Introduction

Discovering the principles that govern neuronal connectivity and how these rules underlie the computations performed by cortical networks is a long-standing challenge in neuroscience (Harris and Mrsic-Flogel, 2013; Reid, 2012). Cortical neurons integrate hundreds of inputs to compute sensory, cognitive and behavioural variables: visual neurons respond selectively to stimulus position and motion (Hubel and Wiesel, 1962); hippocampal neurons represent space (O'Keefe and Dostrovsky, 1971); sequences of neuronal activations in association areas signal the progression through tasks (Harvey et al., 2012); motor neurons trigger specific motions (Georgopoulos et al., 1986). Understanding how these coding strategies arise from neuronal circuits across cortical layers requires measuring the functional properties of cortical cells, and then examining one by one the responses of all the afferents projecting upon those cells (Hubel and Wiesel, 1962).

Single neuron initiated monosynaptic tracing is a powerful technique to target the expression of genetic tools to selected neurons and their monosynaptically connected inputs (Marshel et al., 2010; Vélez-Fort et al., 2014; Wertz et al., 2015). The core technique relies on two experimental steps (Wickersham et al., 2007a, 2007b). First, the starter neuron is targeted for *in vivo* transfection of 3 plasmids: the avian receptor TVA, the rabies virus glycoprotein G and a fluorescent

reporter. Then, an engineered rabies virus is injected: its viral envelope has been coated (i.e. pseudotyped) with the avian glycoprotein EnvA, while the gene coding for the native viral glycoprotein G, which is required for trans-synaptic spread, has been deleted from the viral genome and substituted with a reporter transgene of interest. The selective interaction between EnvA and TVA restricts rabies virus infection to the starter cell. In the starter neuron, complementation of the G protein allows virus replication and transsynaptic spread to the presynaptic partners of the starter neuron.

Despite its conceptual elegance, single neuron initiated monosynaptic tracing has proven difficult to apply routinely due to several experimental hurdles (Reid, 2012). First, single cell transfection *in vivo* requires physical access through a patch pipette, which results in irreversible damage to the target cell in ~20-60% of the attempts (Judkewitz et al., 2009; Kitamura et al., 2008; Oyama et al., 2013; Rancz et al., 2011). Even when the pipette is correctly guided and retracted under imaging guidance (Judkewitz et al., 2009), membrane destabilisation causes depolarisation and sustained firing that can last up to minutes, and eventually causes excitotoxicity and cell death (DeBruin and Krassowska, 1999; Nevian and Helmchen, 2007; Teruel and Meyer, 1997). This limitation is detrimental to experiments that strictly require the labelling of a single neuron, dramatically decreasing the success rate. Second, the implantation of chronic windows for imaging requires the rabies virus to be injected straight after the starter neuron transfection (Wertz et al., 2015): the scarce tissue penetration and high immunogenicity of the enveloped rabies viruses (Packer et al., 2013), combined with the low TVA and G expression levels reached in the starter cell, cause low multiplicity or failure of infection, and, consequently, unsatisfactory tracing yield. These complications take a heavy experimental toll: time and frustration of experimenter, animals, expensive reagents.

Rabies virus can be endowed with the expression of GCaMP and combined with two-photon volumetric imaging to achieve both anatomical and functional characterisation of the traced neurons *in vivo* (Osakada et al., 2011; Wertz et al., 2015). However, the cytotoxicity of rabies virus poses further complications for

these experiments. In the starter neurons, simultaneous delivery of multiple plasmids and infection with rabies virus results in cytotoxicity often within a few days. In the traced presynaptic partners, the continuous replication of the rabies virus harms physiology in a couple of weeks. These effects are exacerbated for rabies viruses functionalised with GCaMP6 due to the known cytotoxic effect of calcium buffering. While non-cytotoxic rabies variants might overcome these limitations (Ciabatti et al., 2017), it has been very hard so far to record simultaneously from the starter neurons and the presynaptic network ensemble *in vivo*. Finally, and perhaps most importantly, this approach limits the recordings to the traced network, preventing functional measurements from the surrounding population, which would provide important context to the results.

In this chapter, I present novel experimental strategies to improve the success rate and the yield of single neuron initiated monosynaptic circuit tracing and recording *in vivo*. I deploy transgenic mouse lines expressing the genetically encoded calcium indicator GCaMP6 to overcome many of the technical obstacles of the technique. First, I describe a new optical method to assess with >80% confidence whether neurons survived single cell transfection *in vivo*, based on the comparison between the intracellular dynamics of GCaMP6 and the surrounding neuropil. This improvement nearly triples the success rate of single neuron initiated monosynaptic tracing. Second, I demonstrate an improved experimental protocol to maximise the yield of the rabies virus tracing and allow simultaneous recording of the responses from the starter cells, its presynaptic neurons and the surrounding population.

3.2 Results

3.2.1 Targeted neuron electroporation with robust cell survival control *in vivo*

I performed targeted single neuron electroporation in the cortex of mice expressing the genetically encoded calcium indicator GCaMP6 in all cortical

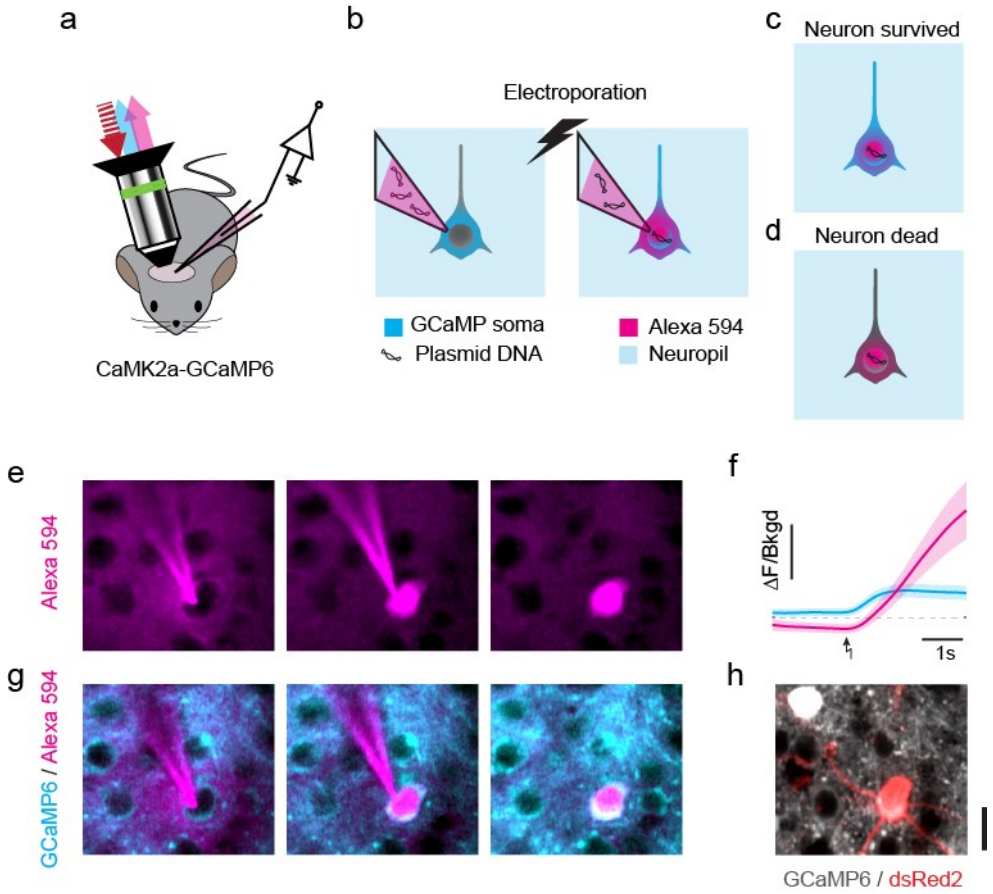

Figure 3.1: Targeted single neuron electroporation with survival control *in vivo*. (**a**) Electroporation performed on a transgenic mouse expressing GCaMP6 in cortical excitatory neurons. A pipette connected to an electroporator, filled with Alexa 594, is targeted to a craniotomy over the cortex under 2P imaging. An infrared laser at 830 nm (*red dashed line*) excites Alexa 594 fluorescence (*magenta*) and GCaMP6 fluorescence (*cyan*). (**b-d**) Neuron survival control based on GCaMP6 fluorescence. A single cortical neuron expressing GCaMP6 is approached with the pipette containing Alexa 594 (*magenta*) and the transgene plasmid (**b**, *left panel*). Upon electroporation, the strong electric field drives the Alexa 594 and the transgene plasmid inside neuron (**b**, *right panel*). (**c**) Survived neurons maintain GCaMP6 fluorescence. (**d**) Irreversibly damaged neurons disappear leaving a dark hole on the GCaMP6 neuropil background. (**e**) Alexa 594 negative contrast time-lapse of single neuron electroporation in layer 2/3 of the mouse V1 *in vivo*: approach (*left panel*), electroporation (*middle panel*), pipette withdrawal (*right panel*). (**f**) Average fluorescence change measured in the target neuron during the electroporation procedure (n = 10). Magenta trace represents Alexa 594 fluorescence; cyan trace indicates GCaMP6 fluorescence. Fluorescence values are normalised to the background fluorescence (*Bkgd*). Arrow indicates electroporation onset and dashed line indicates unity of cell to background ration. (**g**) Same as in **e**, merged with GCaMP6 fluorescence channel at 830 nm excitation. (**h**) Same neuron as in **e**, **g**, imaged at 920 nm 2 days after electroporation, expressing the electroporated transgene dsRed2 (*red channel*) and maintaining healthy GCaMP6 expression levels (*grey channel*). Scale bar 30 µm, same for all the plots. Example data from a Camk2a-tTA; EMX1-Cre; Ai94 mouse.

excitatory neurons (**Figure 3.1**). I implanted the animals with a cranial stainless-steel recording chamber and drilled a craniotomy over the right visual cortex. Then, under a two-photon microscope, I penetrated the dura with borosilicate patch pipettes. Pipettes were filled with intracellular solution complemented with the red dye Alexa Fluo 594 and plasmids coding for the red fluorescent protein dsRed2 (working concentration 100-200 µg/µl) (**Figure 3.1a**).

I reasoned that the successful recovery of a neuron from the electroporation could be read out by comparing the dynamics of the intracellular calcium indicator to the fluorescence of the surrounding cells and neuropil(**Figure 3.1b**). Indeed, electroporation results in sustained firing and a repolarisation phase that could last up to several minutes (DeBruin and Krassowska, 1999; Nevian and Helmchen, 2007). Therefore, I predicted that a cell that successfully recovered from the electroporation procedure should maintain high levels of fluorescence of the intracellular calcium indicator (**Figure 3.1c**). On the other hand, if the electroporation resulted in unrecoverable membrane damage, I should observe a darkening of the cell because the indicator would eventually diffuse out of the cell (Fig 1d).

To test my method, I targeted single neuron electroporation to excitatory neurons in layer 2/3 by means of negative contrast imaging and GCaMP6 imaging (**Figure 3.1e-g**). The injection of the red membrane impermeable dye in the extracellular space counterstained neuronal somas as dark shadows (**Figure 3.1e**). Moreover, I measured the classic hallmark of electroporation: sharp transfer of the red dye inside the target cell, indicative of successful membrane permeabilisation (**Figure 3.1f**).

The GCaMP fluorescence in CaMK2a-GCaMP6 transgenic mice allowed to distinguish excitatory from inhibitory cells, to read out the intracellular calcium dynamics, to gauge the intracellular concentration of GCaMP6 and ultimately evaluate the viability of cells (**Figure 3.1e**). During the electroporation, I imaged GCaMP6 fluorescence at 830 nm, an unusual choice for this sensor, to excite fluorescence both in the calcium-bound and calcium-free isoforms of GCaMP6.

Specifically, 830 nm lies very close to an isosbestic point of the two-photon excitation of the GCaMP6 isomers (2P action cross section spectra available from Harris Lab website), where the calcium-bound sensor is only ~1.5 times brighter than the calcium free isomer. Hence, to a first approximation, GCaMP6 fluorescence at 830 nm is roughly proportional to the intracellular concentration of the sensor and independent of intracellular calcium concentration, thereby allowing to crisply resolve neuronal somas even when the baseline activity was sparse.

As expected, I observed only a ~1.5-fold increase in GCaMP6 fluorescence upon electroporation (**Figure 3.1f**), although calcium levels in the soma likely reached saturating levels. After each electroporation, I recorded reference images of the field of view, which were instrumental to verify cell survival and transgene expression in the following days. At the end of the procedure, I sealed the craniotomy with a glass cranial window. If the neuron survived, it expressed dsRed2 1-3 days post-injection (**Figure 3.1h**). I rarely found neurons that survived but did not express the transgene.

To identify surviving neurons, I imaged GCaMP fluorescence for up to 10 minutes after electroporation, alternating between 920 nm and 830 nm excitation (**Figure 3.2**). I imaged a high magnification field of view including the electroporated cell, few surrounding neurons and neuropil. I then measured the fluorescence time course in the target cell soma, and normalised it to the fluorescence of the surrounding neuropil and neurons. With this procedure I corrected for changes in excitation power during the time lapse and to pool data across experiments. I discarded from further analysis neurons that suffered clear membrane damage upon retraction of the pipette.

The GCaMP6 fluorescence at 830 nm was indicative of cell integrity and predicted neuronal recovery after electroporation (**Figure 3.2**). Neurons that survived the procedure maintained ~2 times higher fluorescence than background, and slowly returned to baseline (**Figure 3.2a, g**). Neurons that were irreversibly damaged by the procedure, after a first increase of fluorescence,

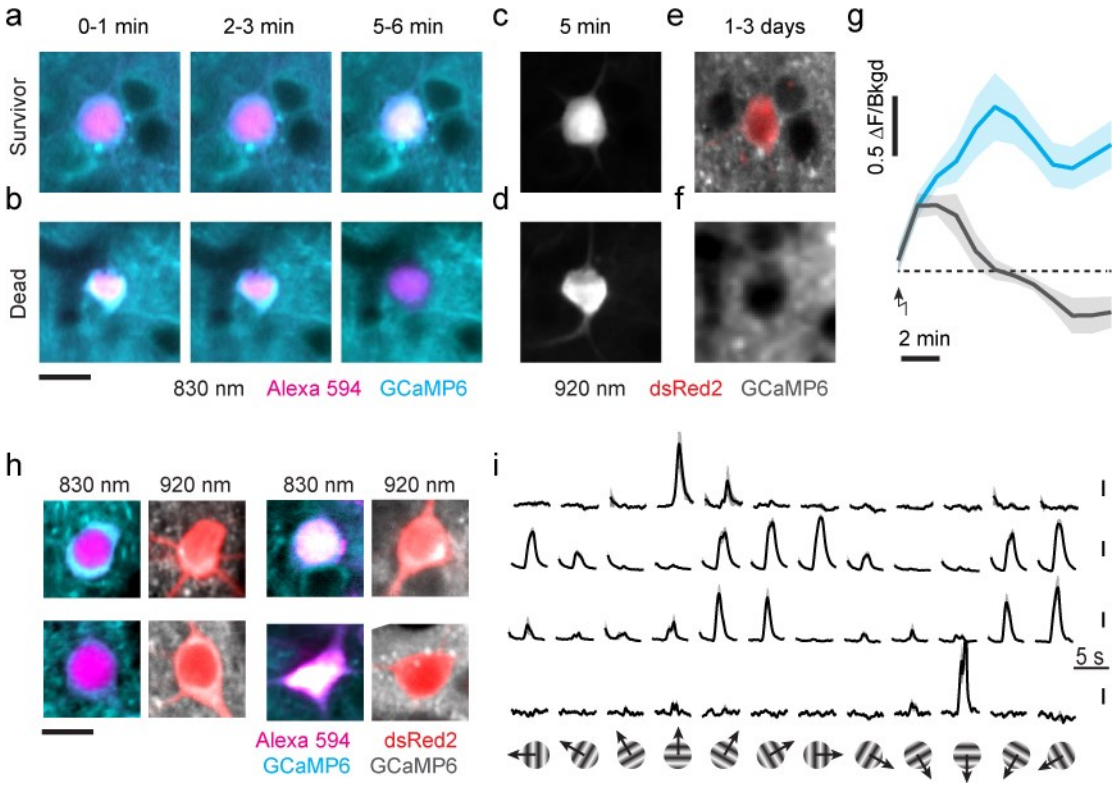

Figure 3.2: GCaMP6 fluorescence predicts survival of electroporated neurons. (**a**) 830 nm time-lapse imaging of a neuron that survived the electroporation. Each panel shows a 30 s average image acquired after the electroporation, at 0-1 min (*left*), 2-3 min (*centre*) and 5-6 min (*right*). Cyan channel shows GCaMP6 fluorescence, magenta channel Alexa 594. Example data from a Camk2a-tTA; EMX1-Cre; Ai94 mouse. (**b**) Same as in **a** for a neuron that did not recover from the electroporation shock. (**c**) 30 s average image of the neuron in **a** 5 min after the electroporation procedure acquired at 920 nm. (**d**) Same as in **c** for the neuron in **b** that did not recover. (**e**) GCaMP6 (*grey channel*) and dsRed2 (*red channel*) at 920 nm imaging of the neuron in **a** 1-3 days after the electroporation. (**f**) Same as in **f** for the dead neuron in **b**. (**g**) Average time-course of GCaMP6 contrast (intracellular/background) for neurons that survived the electroporation (*cyan line*, n = 18) and neurons that did not recover (*grey line*, n = 10). (**h**) Representative example neurons that survived the electroporation imaged at 830 nm after the electroporation (*cyan and magenta*) and at 920 nm 1-3 days later (*grey and red*). Example data from Camk2a-tTA; EMX1-Cre; Ai94 and Camk2a-tTA; EMX1-Cre; Ai93 mice. (**i**) Average visual responses of the example neurons in **h** triggered by gratings drifting in 12 different directions. Traces are z-scored responses, scale bar 1 sd.

slowly turned dark with respect to the background (**Figure 3.2b, g**). This results are consistent with a decrease in GCaMP concentration in damaged neurons, which become darker than the surrounding neuropil where the sensor concentration is higher.

Unexpectedly, all neurons, irrespective of fate, maintained bright fluorescence at 920 nm (**Figure 3.2c, d**). Even neurons that were post hoc confirmed dead remained ~4 times more fluorescent than the surrounding neurons and neuropil minutes after the pipette was retracted (**Figure 3.2d**). Likely, the remaining GCaMP6 trapped inside ruptured neurons was saturated with extracellular calcium and was bright enough to make the soma stand out of the background. This effect was enhanced by the low levels of spontaneous activity in the surrounding neurons during anaesthesia. Therefore, 920 nm fluorescence was not very informative about cell survival.

I assessed the expression of the transfected transgenes 1-3 days after electroporation. Survivor neurons maintained unaltered expression of GCaMP6 with nuclear exclusion, indication that they were healthy and not affected by apoptosis. Moreover, they expressed dsRed2, confirming successful transfection of the electroporated transgenes (**Figure 3.2e**). In contrast, neurons that failed to recover disappeared, leaving a dark hole of GCaMP fluorescence and failing to express dsRed2 (**Figure 3.2f**).

My method correctly judged the neuronal survival after electroporation in 82% of the attempts (22/27). Such results effectively doubled the success rate of the experiment, given that, in my hands, neurons survived the electroporation on 42% of the attempts (22/52 neurons). Such improvement was possible because I could evaluate which neurons survived the procedure and repeat it in case of failure to achieve the desired number of labelled cells. The few false positives consisted of neurons that maintained very high GCaMP fluorescence for the whole time-lapse imaging post injection; such cells probably successfully resealed the membrane but died of excitotoxicity.

Most of the survivor neurons maintained a healthy appearance after electroporation; nonetheless, somewhat counterintuitively, a subset of survivor neurons showed marked signs of cellular stress during the time-lapse imaging window (**Figure 3.2a,h**). Many neurons gradually underwent nuclear filling with calcium indicator, potentially caused by the excessive excitation or the

breakdown of the nuclear membrane following the electric shock (**Figure 3.2a, h**, third column). In other instances, neurons shrunk to a less rounded size, probably due to the osmotic shock caused by electroporation (Fig 2h, bottom right neuron). Therefore, I next tested if the cells that survived the electroporation remained healthy and preserved their physiological response properties. To probe their visual responses, I presented mice with drifting gratings in 12 different directions. All neurons showed calcium activity during visual stimulation, and many displayed consistent orientation and direction selective responses (**Figure 3.2i**). I concluded that cellular stress responses caused by electroporation recovered in the following days.

3.2.2 Efficient pipeline for tracing and recording presynaptic networks

Building on my new single neuron electroporation method, I devised an improved experimental pipeline to nearly triple the success rate of single neuron initiated monosynaptic circuit tracing and recording *in vivo*. In my hands, published protocols yielded a discouraging success rate of 14% (5/36 successful experiments), much lower than for simple electroporation experiments, potentially because of the complications due to rabies tracing. However, when I controlled for electroporation outcome, success rate increased to 41% (7/17). I considered an experiment successful when the rabies virus tracing yielded more than 30 presynaptic neurons.

The first step in the pipeline is the electroporation of a single neuron in L2/3 of the mouse visual cortex with plasmids coding for the avian receptor TVA, the optimised rabies virus glycoprotein oG and the red fluorescent protein dsRed2 (**Figure 3.3a**). Rather than injecting the rabies virus straight away as suggested by published protocols, I sealed the craniotomy with a removable cranial window (**Figure 3.3b**). This procedure offers many advantages. First, it allows the experimenter to wait for optimal TVA and G expression levels in the starting neuron before rabies virus injection, which will improve the yield of rabies

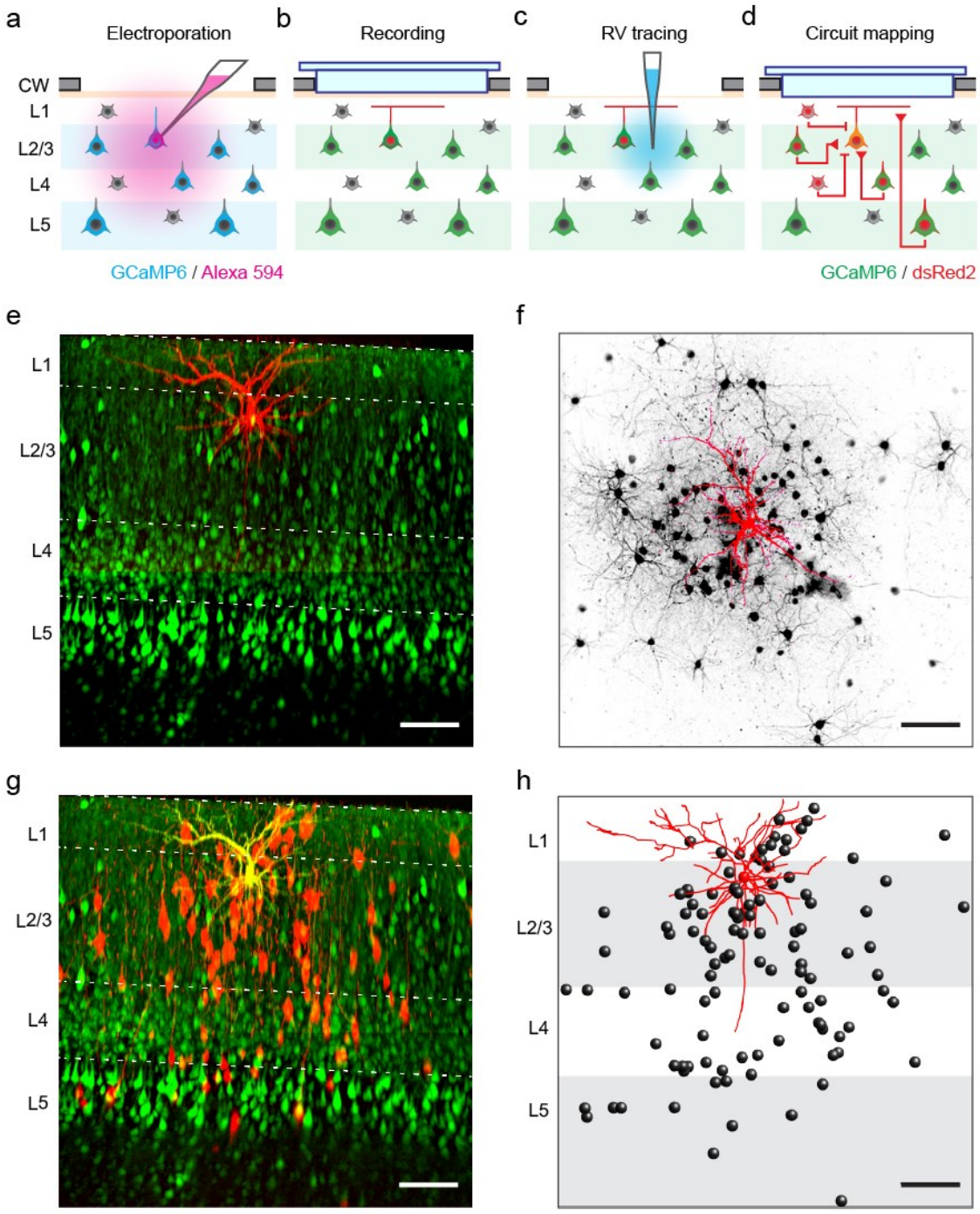

Figure 3.3: *In vivo* single neuron initiated transsynaptic tracing and functional imaging in GCaMP6 transgenics. (**a-d**) Cartoon of the novel experimental pipeline for single-neuron initiated monosynaptic tracing in GCaMP6 transgenics: (**a**) targeted single neuron electroporation; (**b**) morphological tracing and functional imaging of the starter neuron; (**c**) injection of pseudotyped rabies virus, durotomy and replacement of the cranial window; (**d**) functional imaging and tracing of presynaptic networks. (**e**) Coronal maximum intensity projection of structural z-stack of an electroporated starter neuron expressing dsRed2 (*red channel*), and surrounding GCaMP6 expressing neurons (*green channel*). White dotted lines

indicate cortical layers' boundaries. (**f**) Frontal maximum intensity projection of the structural z-stack of a starter neuron (*red*), registered with frontal maximum intensity projection of the structural z-stack of the presynaptic network acquired after tracing (*black neurons*). (**g**) Coronal maximum intensity projection of starter cell (*yellow*), presynaptic neurons (*red*) and surrounding GCaMP6 positive neurons. (**h**) Morphological tracing of the starter neuron (*red*) and anatomical reconstruction of presynaptic neurons (*black*) across layers. Example data from a Camk2a-tTA; EMX1-Cre; Ai94 mouse.

infection and transsynaptic spread. Second, and most importantly, it leaves a window of several days to simultaneously record the responses of the starter neuron and the surrounding population while the starter cell is still healthy (Fig 3b). Finally, in case multiple starter neurons are electroporated, this procedure allows the selection of one neuron with interesting physiological responses and the elimination of the rest of the neurons using photo-ablation.

Once I obtained a satisfactory morphological and functional characterisation of the starter neuron, I removed the cranial window and injected an EnvA-dG-dsRed2 rabies virus (**Figure 3.3c**). This procedure required the removal of the dura mater. While this step required an expert surgeon, it preserved the long-term clarity of the cranial window by preventing bone regrowth; in addition, it significantly improved the quality and penetration of two-photon imaging. I completed the surgery by sealing the craniotomy with a new, permanent cranial window. In the following days, I continued functional imaging experiments, and recorded detailed z-stacks to follow the progress of the rabies transsynaptic spread (**Figure 3.3d**).

My experimental strategies yielded detailed morphological, anatomical and functional characterisation of the starter neuron and its presynaptic network (**Figure 3.3e-h**). Volumetric two-photon calcium imaging was used to record simultaneously the activity of the starter neuron and of the surrounding excitatory population. Moreover, I acquired high-resolution z-stacks to reconstruct the morphology of the dendritic tree of the starter neuron expressing the bright dsRed2. In the structural z-stacks, the expression of GCaMP6 in all excitatory neurons perfectly delineated the location of the cortical layer borders. A coronal maximum intensity projection highlighted the L2/3 sparsely active

pyramids, the densely packed granules in L4 and the bright large pyramids in L5 (**Figure 3.3e-g**). The identification of these boundaries in each animal was used to determine the cortical layer of the traced presynaptic neurons.

3.2.3 Simultaneous recording of starter neurons and presynaptic networks

We analysed 9 pilot datasets to characterise the temporal evolution of the starter neuron health and the progression of the tracing across days (**Figure 3.4a)**. As expected, both the starter neuron and many presynaptic neurons expressed GCaMP6 (**Figure 3.4b, c)**. The delayed injection of rabies virus was crucial to prolong the temporal window suitable to record healthy responses from the starter neuron. In my experiments, I recorded starter neuron's activity for up to 7 days before starting the rabies tracing. Once I injected the virus, the starter neuron health quickly deteriorated: by the 3rd day post injection, most starters displayed GCaMP nuclear filling (**Figure 3.4d**, third panel) and aberrant or ceased firing (Fig 4a, orange curve); within the first week post injection, most of the starter cells underwent apoptosis (**Figure 3.4a**, red curve, Fig 4d, fourth panel).

On average, my protocol traced 132±41 presynaptic neurons per starter cell (**Figure 3.4a**, black curve). This count only includes neurons that could be imaged in a volume of ~850x850x700 microns below the cortical surface around the postsynaptic cell. Histological analysis revealed additional traced cells in many secondary visual areas, associative cortices and thalamus (not shown). Traced presynaptic neurons started to appear around the 4th day post injection, and steadily increased in number peaking around the 10th day (**Figure 3.4a**, black curve). A successful tracing seemed to crucially depend on both the efficiency of transfection and the long survival of the starter neurons.

The longer health of the starter cell offered the opportunity to image its activity at the same time as the responses of its presynaptic partners (**Figure 3.5**). To this

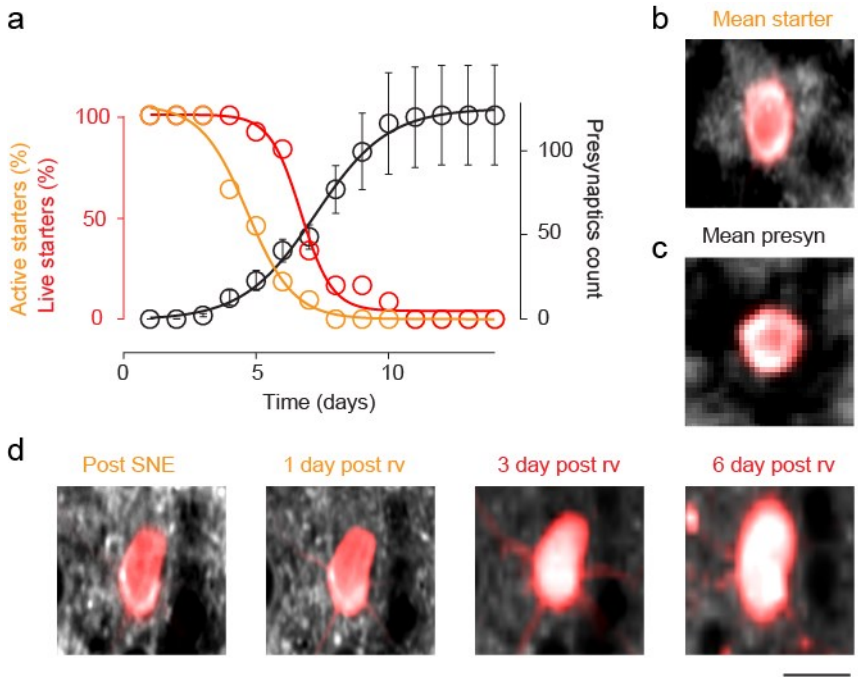

Figure 3.4: Time-lapse of starter neuron health and presynaptic tracing count. (**a**) Temporal evolution of the percentage of functionally responsive starter cells (*orange*), starter cell integrity before apoptosis (*red*) and traced presynaptic neuron count (*black*) over time (n= 9) (**b**) Average mean projection of the starter neurons during functional imaging. (**c**) Average mean projection of functionally active presynaptic neurons. (**d**) Time-lapse mean images of one starter neuron after the electroporation (*leftmost panel*), 1 day (*centre left*), 4 days (*centre right*) and 6 days (*rightmost panel*) post rabies virus infection.

end, I performed volumetric two-photon calcium imaging before injection of the rabies virus, when the starter neuron was still healthy (**Figure 3.5a**). Then I registered the imaging planes to the anatomical z-stack acquired after tracing its presynaptic network (**Figure 3.5b**). In this way I identified post-hoc several presynaptic neurons imaged simultaneously with the starter cell (**Figure 3.5c**), and correlated their activity with the responses of their common postsynaptic partner (**Figure 3.5d, e**).

3.3 Discussion

I described novel methods to achieve robust single cell initiated monosynaptic circuit tracing and recording *in vivo*. My study builds on published methods for targeted single neuron transfection *in vivo* and single cell initiated monosynaptic tracing: by exploiting recently developed transgenic animals expressing the genetically encoded calcium indicator GCaMP6, I improved on these methods

and provide an efficient experimental pipeline for anatomical tracing and functional recording from single cortical neurons, their presynaptic networks and the surrounding neuronal population.

My single cell electroporation strategy ascertains with >80% confidence the survival of neurons after *in vivo* targeted transfection. Current *in vivo* transfection methods lack a reliable measure to determine whether a neuron survived the procedure; the problem is exacerbated for experiments that strictly require a single cell to be targeted, because the experimenter cannot perform multiple attempts in the same animal. This is a crucial requirement to target rabies virus tracing to single neurons. In my hands, my approach nearly doubled the success rate of experiments that aimed at labelling a single cortical cell.

While the technique is based on transgenic animals expressing GCaMP6, I show that the key to high-yield results is the comparison of the intracellular concentration of GCaMP in the target neuron with the surrounding neurons and neuropil, and not the readout of calcium concentration. In principle, my approach should generalise to any fluorescent probe expressed at the population level or in specific neuronal classes, if expression is sufficiently dense to compare fluorescence levels in neighbouring neurons. Moreover, while scattering limits two-photon guided transfection to the superficial cortical layers, the recent development of 3P microscopy (Ouzounov et al., 2017)will extend the range of optically targeted transfection to deeper neurons. My novel experimental pipeline maximises the success rate of rabies tracing, and combines it with volumetric two-photon imaging to provide detailed morphological, anatomical and functional characterisation of the starter neuron and its presynaptic network.

Rabies viruses expressing GCaMP6 have been previously used to record the responses of the starter cells and their presynaptic partners. However, these approaches suffered from the increased cytotoxicity of the GCaMP expressing rabies. In addition, recordings were limited to the traced neurons, making it impossible to compare their responses to the surrounding neuronal population.

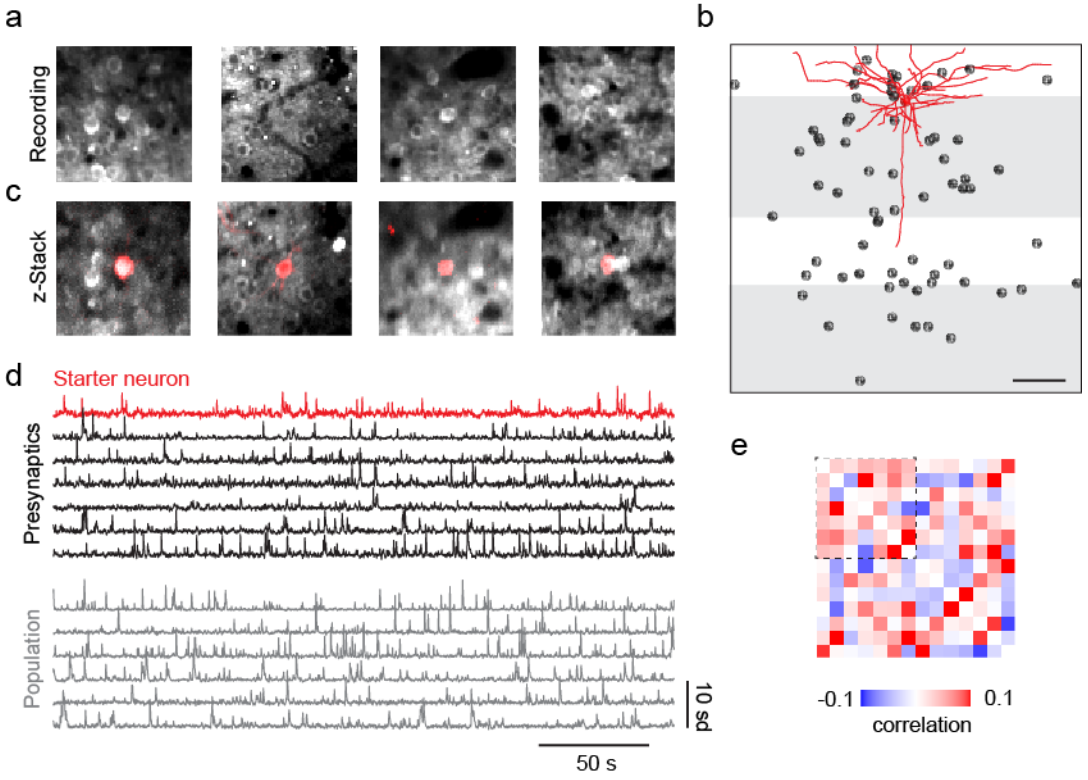

Figure 3.5: Volumetric imaging of starter neuron and surrounding population with post-hoc identification of traced presynaptic neurons. (**a**) Mean projections of 100 µm^2 regions of the imaging field of view of a volumetric two-photon calcium imaging acquisition, 1 day after the starter neuron electroporation (**b**) Anatomical reconstruction of the traced neurons from a structural z-stack acquired after monosynaptic tracing of the same starter neuron in **a**. Shaded rectangles outline cortical layers' boundaries. Scale bar 100 µm. (**c**) The regions imaged in **a** were registered to the structural z-stack to identify the traced neurons. (**d**) GCaMP6 fluorescence time courses recorded simultaneously from the starter neuron (*red*), the presynaptic cells (*black*) and surrounding neurons (*grey*). (**e**) Correlation matrix of the responses from the neurons in **d**. GCaMP6 responses were sampled at 3Hz. Dotted square identifies the starter neuron (*first entry*) and its presynaptic partners. Example data from a Camk2a-tTA; EMX1-Cre; Ai94 mouse.

I overcame these limitations by expressing GCaMP at the population level, and demonstrated that transgenic GCaMP positive neurons can tolerate rabies infection the same way as wild type neurons. Moreover, by separating in time the transfection of the starter cell and rabies injection, I increased the time window to record healthy responses from the starter neurons and increase the number of traced presynaptic cells. Finally, I demonstrated for the first time a method to identify presynaptic neurons recorded simultaneously to the starter cells by post-hoc reconstructions using high-resolution z-stacks acquired *in vivo*.

Overall, the methods presented herein can be used to nearly triple the success rate of single cell initiated rabies virus monosynaptic tracing. These improvements might help to harvest the fruit of this powerful technique, which despite being demonstrated 10 years ago has struggled to become established in many laboratories. Moreover, these improvements will open novel experimental avenues: for instance, rabies viruses can be coated with different variants of avian glycoprotein EnvA and EnvB to target distinct neurons tagged with the parent receptors TVA and TVB. While these tools are already available to the neuroscience community, in practice they have never been used to target separate circuits in order to study their interactions *in vivo*. By allowing strict control over the number of electroporated cells and flexibility over the timing of injection of the rabies, my pipeline paves the way for elucidating the interactions between interlaced cortical presynaptic networks. Finally, future endeavours will be helped by the engineering of non-cytotoxic variants of rabies virus (Ciabatti et al., 2017), which can be used for circuit manipulations.

Chapter 4

Functional organisation of presynaptic networks in the mouse primary visual cortex

4.1 Introduction

Neurons in the primary visual cortex (V1) are tuned to visual features like retinotopic location, orientation and direction of motion (Niell and Stryker, 2008). Such selectivity stems from the integration of inputs from a presynaptic network composed of hundreds of neurons distributed across cortical layers and thalamus (Douglas and Martin, 2004; Wertz et al., 2015). Understanding how the functional architecture of the presynaptic network, and the activity of its neurons, relate to the functional properties of the postsynaptic neuron is a fundamental challenge in neuroscience; facing it could elucidate the principles that organise neuronal connectivity and ultimately cortical computations (Carandini et al., 2005; Harris and Mrsic-Flogel, 2013).

Local connectivity between primary visual neurons is not random (Lee et al., 2016; Perin et al., 2011; Song et al., 2005), but rather organised according to specific functional principles (Yoshimura et al., 2005) which have only begun to be understood (Reid, 2012). Neurons with high response correlation and similar receptive field (RF) properties preferentially connect to each other (Cossell et al., 2015; Ko et al., 2011): therefore, it has been proposed that visual neurons are wired to form interacting subnetworks with the purpose of amplifying the tuning of neurons to features like the orientation, or direction of moving gratings (Han and Mrsic-flogel, 2013; Harris and Mrsic-Flogel, 2013). However, it remains unclear if these functional principles of connectivity generalise across cortical layers and over larger cortical distances, or if different rules for the integration of

more abstract stimulus features exist. Indeed, recent research suggests that layer 2/3 (L2/3) visual neurons receive synapses from separate modules of neurons in different layers(Yoshimura et al., 2005), and that such modules could have 'variant tuning' with respect to the postsynaptic cell, that is different selectivity to image motion (Wertz et al., 2015). Accordingly, *in vivo* single-cell recordings from L2/3 pyramidal cells in V1 have revealed different degrees of similarity between the preferred orientations at the dendritic input sites and at the cell body (Chen et al., 2013; Jia et al., 2010).

Besides the tuning of individual neurons, the functional and neuroanatomical architecture of presynaptic networks upstream to visual neurons remains poorly understood: it is not known whether presynaptic networks are uniform in cortical space, or if there are anisotropies in the spatial distribution of neurons, perhaps related to the postsynaptic neuron position in the retinotopic map and to its orientation preference. It is also unclear if there is a relationship between the dendritic morphology and the spatial distribution of the presynaptic inputs. For instance, a recent study suggests that L2/3 neurons might receive distant inputs with the same orientation preference to represent extended oriented edges along the visual field (Iacaruso et al., 2017); however, it is not known whether this bias towards input from specific regions of the surrounding cortex translates to an elongated spatial distribution of the presynaptic network in retinotopic space.

Finally, it remains an open question whether the subnetworks of neurons revealed by connectomics correspond to patterns of neurons that tend to be coactive, and how such patterns of neuronal activation vary with brain state (Hofer et al., 2011; Luczak et al., 2009). In fact, most of the functional connectomics studies so far measured neuronal responses under anaesthesia (or *in slices*) : it remains to be determined whether neurons that are connected or share a synaptic partner are more likely to participate in the same functional assembly than neurons that are not, both during responses to sensory stimuli and during spontaneous activity in awake animals (Harris, 2012). Indeed, driving and modulatory synapses, the latter of which are weaker but constitute the majority

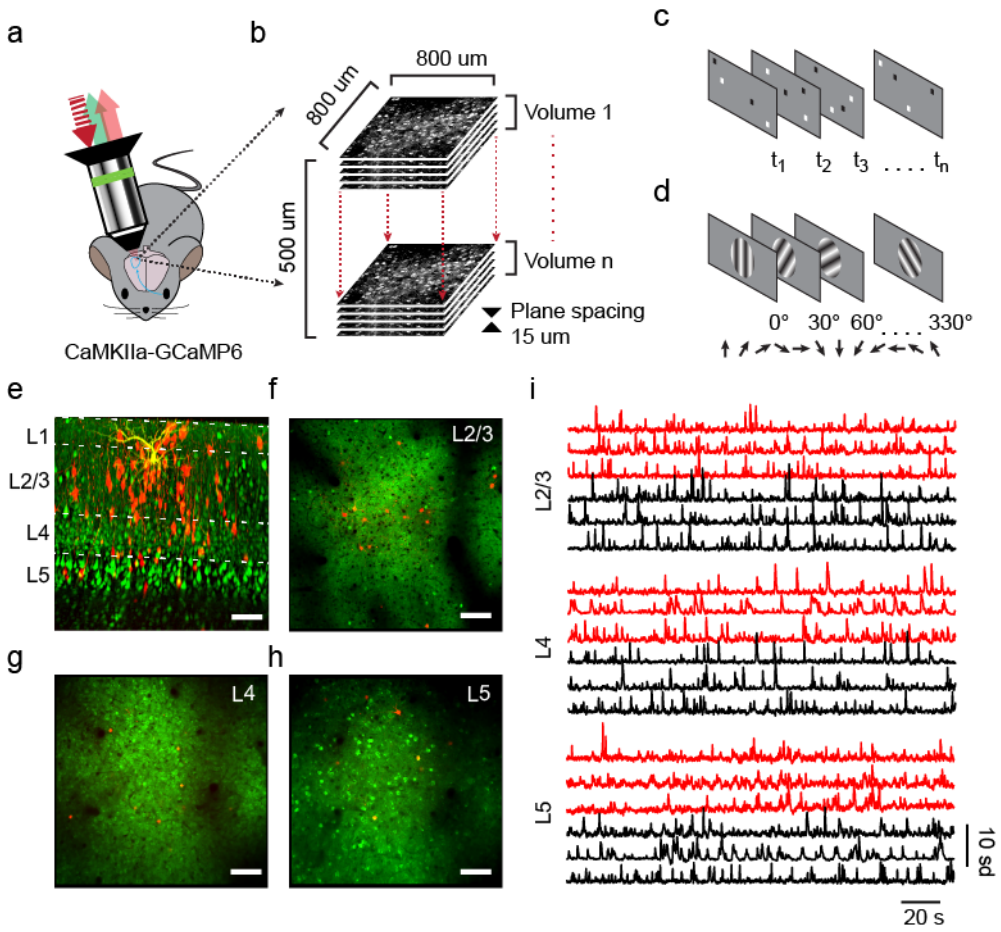

Figure 4.1: Volumetric two-photon calcium imaging of presynaptic networks in V1. (**a**) Two-photon excitation (*red dotted arrow*) of GCaMP and dsRed2 fluorescence (*green and red arrow*) in V1 of a transgenic mouse expressing GCaMP6 in all excitatory cortical neurons. The presynaptic network to a target L2/3 neuron was traced with an EnvA-dsRed2 rabies virus. (**b**) A series of 4-8 multiplane volumetric imaging sessions was used to record responses from neurons spanning an 800 x 800 x 500 µm cortical volume. (**c**) Sparse noise stimuli used for retinotopic mapping. (**d**) Drifting grating stimuli shown for orientation tuning experiments. (**e**) Sagittal maximum intensity projection of a structural z-stack of the imaged volume showing the starter neuron (*yellow*), the presynaptic partners (*red*) and the surrounding population (*green*). (**f**) Example imaging plane from L2/3. (**g**) Example imaging plane from L4. (**h**) Example imaging plane from L5. (**i**) Example recording from traced neurons and other excitatory population across layers. Within the same layer, responses were recorded simultaneously. Scale bar in **e, f, g, h** is 100µm. Example data from a Camk2a-tTA; EMX1-Cre; Ai94 mouse.

of the inputs (Cossell et al., 2015; Harris and Shepherd, 2015), might be weighted differently during different brain states.

To characterise the functional organisation of presynaptic networks upstream of L2/3 pyramidal neurons in mouse V1, I deployed the powerful approach demonstrated in Chapter 2, and combined single neuron initiated monosynaptic rabies virus tracing (Marshel et al., 2010; Vélez-Fort et al., 2014; Wertz et al., 2015; Wickersham et al., 2007b) with two-photon microscopy in mouse V1. In this chapter, I describe recordings and anatomical reconstructions from 9 L2/3 neurons and their presynaptic networks. I measure the detailed dendritic morphology of the starter neurons and map the neuroanatomical distribution of their inputs in V1. I relate these neuroanatomical measurements with the fine scale retinotopic map to reveal that presynaptic networks are elongated in retinotopic space and that such elongation predicts the orientation preference of the postsynaptic cell. Finally, I report that the tuning of neurons in each presynaptic network is heterogeneous and is not necessarily aligned to the orientation preference of the corresponding postsynaptic cell.

4.2 Results

4.2.1 Recording physiology and anatomy of networks in V1

To characterise the functional organisation of presynaptic networks upstream of L2/3 pyramidal neurons in mouse V1, I used single neuron initiated transsynaptic tracing in mice expressing the calcium indicator GCaMP6 in all excitatory cortical neurons (Madisen et al., 2015). I implanted the mice with a headpost and a removable cranial window (**Figure 4.1**a). In each experiment, I electroporated a single pyramidal neuron (Judkewitz et al., 2009) in L2/3 with plasmids coding for the rabies glycoprotein oG (Kim et al., 2016), the avian receptor TVA(Wickersham et al., 2007b) and the red fluorescent protein dsRed2. I termed this cell the 'starter neuron'. After obtaining detailed morphological reconstructions and functional recordings from the starter neuron, I extracellularly injected an EnvA-dG-dsRed2 rabies virus (Wickersham et al., 2007b), which could only infect the TVA tagged starter neuron and then spread to its presynaptic partners.

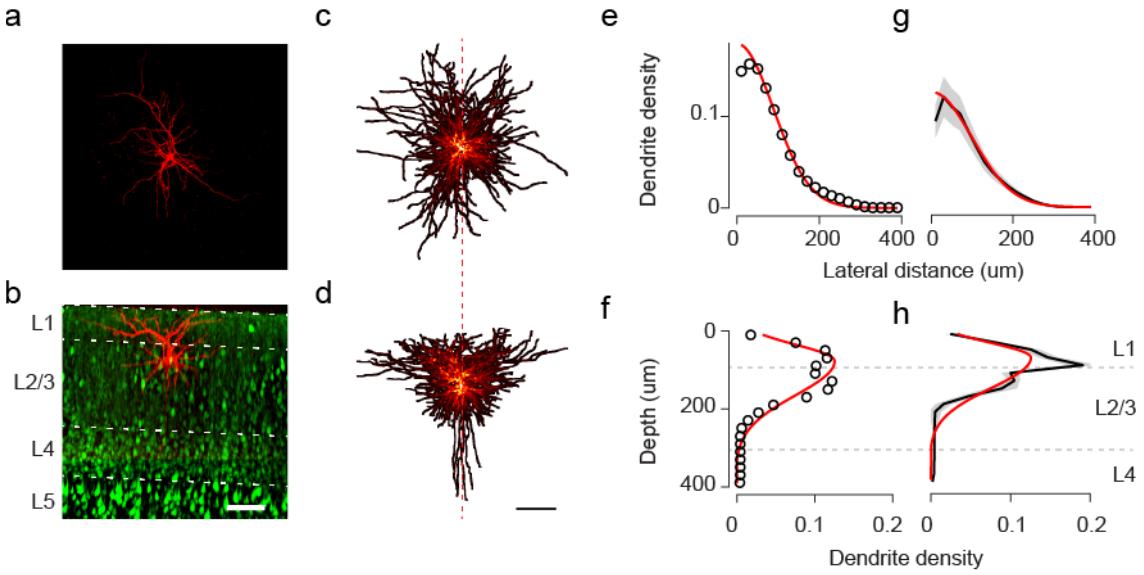

Figure 4.2: Morphological reconstruction and analysis of starter neurons dendritic tree. (**a**) Frontal maximum projection of structural z-stack of a dsRed2 expressing starter neuron. (**b**) Sagittal maximum projection of same structural z-stack from **a,** showing the starter neuron in red, and lamination of surrounding excitatory population in green in a Camk2a-tTA; EMX1-Cre; Ai94 mouse. White dotted lines indicate layer borders. Scale bar 100um, shared with **a**. (**c**) Average coronal projection of morphological reconstructions from all the starter neurons. The colormap temperature indicates dendrite density in each μm^2 pixel. (**d**) Same as in **c** for the sagittal projection. (**e**) Density of dendrites as a function of lateral distance from the soma for the example neuron in **a** (**f**) Density of dendrites as a function of cortical depth, for the example neuron in **a.** (**g**) Average dendrite density as a function of lateral distance from the soma across starter cells (n=7) (**h**) Average dendrite density as a function of cortical depth from the soma across starter cells (n=7). Red lines represent Gaussian fits (**e, g)** or asymmetric Gaussian fits (**f, h**).

Then, I used volumetric two-photon calcium imaging (Göbel et al., 2007) to simultaneously record the functional responses of the starter neuron, its presynaptic neurons and the rest of the excitatory population (**Figure 4.1a,b**). During imaging, mice were awake and free to run on a treadmill (**Figure 4.1b**); I first presented animals with sparse noise stimuli to map the retinotopy of the imaged neurons (**Figure 4.1c**); then, I showed 30-60 degrees wide circular gratings drifting in twelve different directions (**Figure 4.1d**), centred at the retinotopic position of the field of view (FOV).

To densely sample neurons across layers 2-5, I repeated simultaneous acquisition of 5-10 imaging planes spaced 15µm and tiled a cortical volume of 800*800*500µm around the starter neuron (**Figure 4.1e**). Despite the dense

expression of GCaMP6, I could resolve active neuronal somas in L2/3 (**Figure 4.1f**), L4 (**Figure 4.1g**) and superficial L5 (**Figure 4.1h**). I then registered each imaging session and segmented ROIs representing active neurons using an automated pipeline for two-photon imaging analysis (Pachitariu et al., 2016); I manually sorted ROIs corresponding to red cells to identify active presynaptic neurons in each cortical layer (**Figure 4.1i**).

Across days, I acquired high resolution z-stacks to reconstruct the morphology of the starter neuron and map the cortical distribution of its presynaptic inputs (**Figure 4.1e, Figure 3.3**). As the rabies tracing progressed, the increasing expression of dsRed2 rabies virus traced the anatomical position of presynaptic inputs from the cortical surface down to 700µm in L5 (**Figure 4.1e, Figure 3.4**). The expression of GCaMP6 in all excitatory neurons provided us with a clear demarcation of the borders between cortical layers, enabling us to assign the traced neurons their parent cortical layer *in vivo*.

4.2.2 Dendritic morphology of L2/3 starter neurons

Based on the expression of GCaMP6, and on morphological hallmarks, I classified the starter neurons as L2 intra-telenchepalic excitatory cells. Indeed, all electroporated cells showed pyramidal somas located between 100-200µm from the cortical surface. The expression of the electroporated dsRed2 revealed spiny dendritic trees that ramified extensively in L1-2-3 for hundreds of microns (**Figure 4.2a,b**). Helped by a supervised neurite tracing software (Feng et al., 2014), I used the two-photon z-stacks acquired *in vivo* to trace the morphology of most of my starter cells. Analysis of the average dendrite morphology confirmed two morphological hallmarks of this neuronal class: a stubby but extremely ramified apical dendrite, whose collaterals could span 200-300µm laterally in L1 (**Figure 4.2c**); and a dense arborisation of basal dendrites caged around the soma (**Figure 4.2d**).

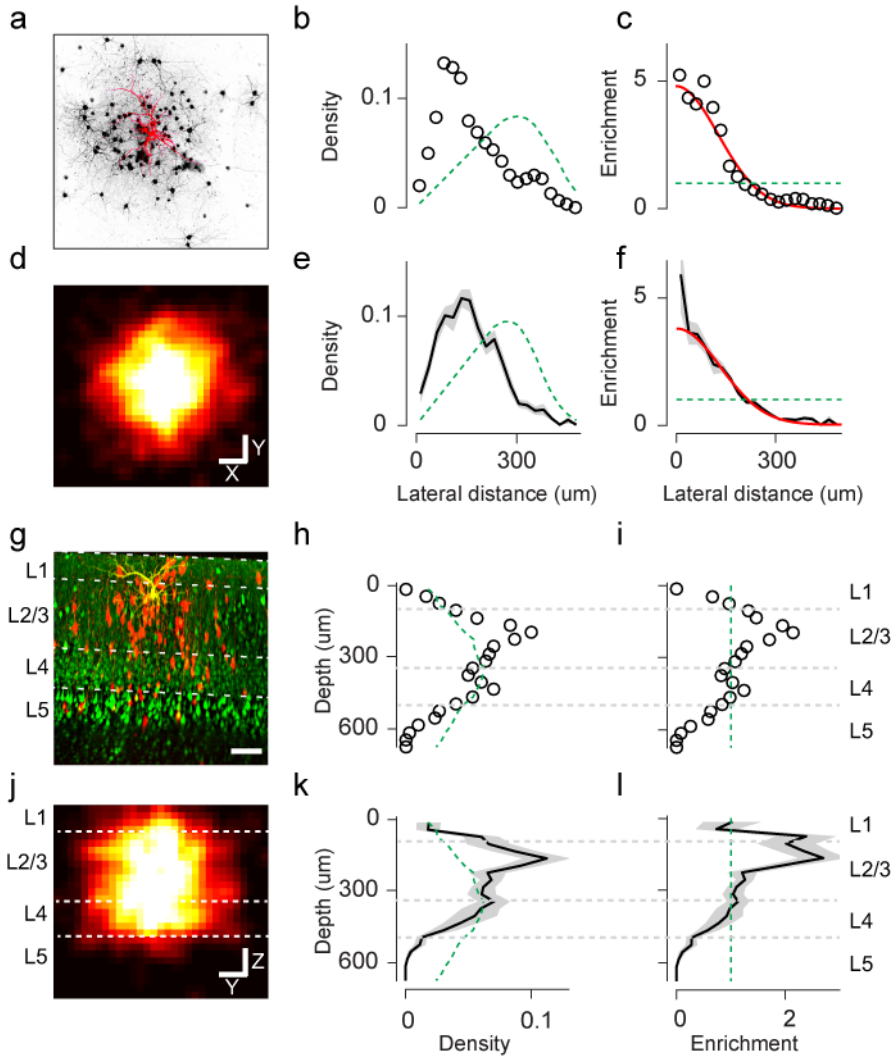

Figure 4.3: Anatomical mapping of presynaptic networks of L2/3 neurons. (**a**) Frontal maximum projection of the example starter cell from **Figure 4.2** (*red neuron*) and its presynaptic partners (*black neurons*) in a Camk2a-tTA; EMX1-Cre; Ai94 mouse. (**b**) Density of presynaptic neurons as a function of somatic distance from the starter neuron in **a** (*black circles*) calculated in 25µm bins. Green dotted line represents the probability of encountering neurons in concentric rings of increasing radius from the starter cell. (**c**) Enrichment of pairwise connections as a function of lateral somatic distance from the starter cell, calculated by dividing the black circles by the green dotted line in **b**. Unity green line represents uniform distribution. Red curve represents Gaussian fit to the data. (**d**) Average spatial distribution of presynaptic neurons across experiments (n= 9), calculated in 25µm bins. (**e-f**) Same as in **b-c** for the average distributions. (**g**) Sagittal projection of the starter neuron (*yellow*), the presynaptic partners (*red*) and the surrounding population (*green*). (**h**) Density of presynaptic neurons as a function of cortical depth for the starter neuron in **a, d,** calculated in 25µm bins. Green dotted line represents the total density of neurons at each cortical depth. (**i**) Enrichment of pairwise connections with cortical depth for the example neuron in **a, d**. (**j**) Average distribution of presynaptic neurons across cortical layers and across experiments (n= 9), calculated in 25µmbins. (**k-l**) Same as in **h-i** for the average across experiments.

While my z-stacks could also identify the main axon descending vertically across cortical layers (**Figure 4.2d**), I did not attempt to trace its numerous collaterals.

I used 3D morphological reconstructions to measure the statistics of the starter neurons dendritic arborisation in cortical space. For each neuron, I first measured the probability of encountering dendrites as a function of lateral distance from the soma (**Figure 4.2e**). The resulting density function was well-fitted by a Gaussian centred at the soma. I repeated this procedure on the average dendrite projection across neurons, aligning each dendritic tree to the soma: the average dendrite density fell with a spatial constant (i.e. the standard deviation of the Gaussian) of 85±13µm. Then I repeated a similar analysis to measure the distribution of dendrites across layers. The dendritic arborisation did not reach further than deep L2/; I approximated it with an asymmetric Gaussian function (**Figure 4.2f**, i.e. a Gaussian curve with two different standard deviations around its peak). The different widths probably reflect the different spatial statistics of the apical and basal dendrites arborisations (**Figure 4.2h**).

4.2.3 Anatomical organisation of presynaptic networks

For each starter neuron, I traced a presynaptic network comprising on average 132±41 V1 presynaptic partners (range of 38-334, n = 9), distributed laterally in V1 for almost a millimetre and across all cortical layers (Figure **4.3a**,**d**,**g**,**j**). I aligned the z-stack of each starter neuron to the z-stack of its presynaptic network to reconstruct the detailed spatial anatomical distribution of the presynaptic inputs with respect to their common postsynaptic target (Fig 3a,g); then I averaged the results across experiments (Figure **4.3d**,**j**).

First, I measured the lateral distribution of presynaptic somas as a function of lateral cortical distance, irrespective of cortical depth, and then derived for each starter neuron the connection probability with the local population (Fig 3a-f). L2/3 neurons received on average most of their inputs from peers laterally displaced by 100-200 µm(Figure **4.3**e). Nonetheless, this measure does not take into account the fact that, progressing further away from the starter neuron in

concentric rings, the pool of potential synaptic partners linearly increases with distance. Hence, to obtain a measure of pairwise connection probability as a function of lateral cortical distance, I divided the measured presynaptic somas density by the area of concentric rings surrounding the starter neuron in dependence of distance, which is in turn proportional to how many potential synaptic pairings are available at each distance (Figure **4.3b**, e green line). Rather than normalising this function to 1, as you would for a probability density function, I kept the scale to measure the 'enrichment' of presynaptic at each distance (Figure **4.3c**) with respect to a flat connection probability (Figure **4.3c**, green line). The result indicates that L2/3 neurons sample nearly 5 times more densely from neighbouring neurons, and that the probability of receiving a synapse decays with intersomatic displacement according to a Gaussian profile with spatial constant (i.e. standard deviation) of 130.8±8.9 μm(Figure **4.3c,f**). Notably, this profile has a similar shape, but a longer space constant, to the dendritic tree of the starter neurons (**Figure 4.2**).

I repeated a similar analysis to measure the distribution of presynaptic inputs, and the connection probability, across layers (Figure **4.3g,j**). Inputs to L2/3 neurons were more abundant in layer 2/3 and L4 (Figure **4.3g,j,h,k**). While my data could underestimate the density of inputs from L5, because I could not image deep in L5 in all the experiment, these results agree with previous reports (Wertz et al., 2015). To estimate the global density profile of neurons across layers, I measured the number of responsive ROIs identified in my functional imaging experiments (Figure **4.3h**, k, green line). Finally, I divided the measured distribution of presynaptic neurons by this global density to gauge the enrichment of pairwise connections from inputs in different layers (Figure **4.3i, l**). This analysis showed that L2/3 starter cells sampled twice more densely from their peers in L2/3 when compared to their potential inputs from L4. L2/3 neurons also seemed to receive abundant connections from L1 neurons: because very few excitatory neurons expressed GCaMP in L1, these inputs were likely superficial interneurons (Figure **4.3i, l**).

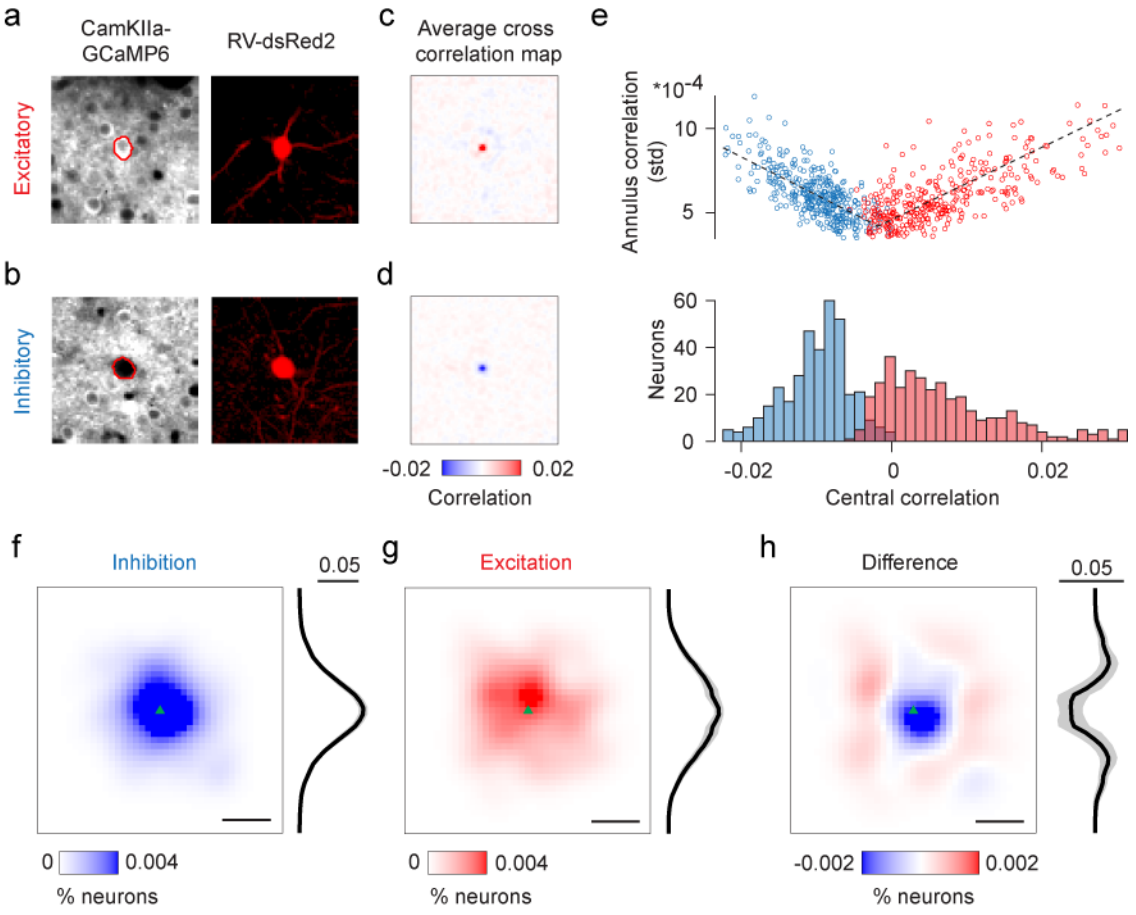

Figure 4.4 Anatomical organisation of excitatory and inhibitory presynaptic networks. (**a**) Example presynaptic excitatory neuron from a Camk2a-tTA; EMX1-Cre; Ai94 mouse: average GCaMP6s fluorescence image (*left panel*) and average RV-dsRed2 fluorescence image (*right panel*). The somatic mask segmented from the RV-dsRed2 image is superimposed on the GCaMP6 channel (*red outline*). (**b**) Same for an example putative inhibitory neuron. (**c**) Map of cross correlation between the somatic mask and the GCaMP6 image, averaged across all putative excitatory cells. (**d**) Same for putative inhibitory neurons. (**e**) The central peak of the correlation map plotted against the standard deviation of a 5 µm annulus around the peak highlight the cluster of putative excitatory neurons (*red dots*) and the cluster of putative inhibitory neurons (*blue dots*). The classification was obtained from k-means clustering or bilinear fit (*black dotted line*). (**f**) 2D density map of lateral distribution of putative presynaptic inhibitory neurons around the postsynaptic neuron (*green triangle*), data pooled across the experiments (*n=377*). The unidimensional distribution was obtained averaging projections onto 35 lines through the postsynaptic neurons, with slopes sampled every 10 degrees. (**g**) Same for putative excitatory neurons (*n=342*). (**h**) The difference between the inhibitory and excitatory distributions generates an inverse Mexican hat profile. Scale bar is 100 µm.

Finally, I classified traced presynaptic neurons as putative excitatory or inhibitory units based on the expression of GCaMP6, which was driven in all excitatory cortical neurons by the CaMKIIa promoter (Figure **4.4**). Quantification

on data pooled across experiments indicated that 49% of the traced presynaptic neurons were excitatory cells, while 51% were putative inhibitory neurons. To measure GCaMP6 expression, I leveraged on the z-stacks resulting from serial volumetric functional imaging acquisitions (Figure **4.4a-b**): while these z-stacks had coarse sampling in z (planes spaced 15 μm), they granted prime lateral resolution from the averaging of thousands of frames acquired during over >1h long imaging sessions. I devised a semi-automatic algorithm to identify and classify RV traced cells as GCaMP6 positive or negative: briefly, somatic ROIs were segmented based on dsRed2 fluorescence acquired in the red channel (Figure **4.4a-b**); at this point each ROI was inspected and either accepted as a valid cell, or discarded in case of false positives or out of focus cells. Then, the algorithm calculated the phase correlation map between the binary mask of each ROI and the GCaMP6 fluorescence image (Figure **4.4c-d**). Neurons expressing GCaMP6 resulted in a strong positive central correlation peak, when the ROI mask and the bright shape of the GCaMP6 positive cell matched nicely(Figure **4.4c**). Conversely, GCaMP6 negative neurons resulted in a strong negative central correlation peak, where the ROI mask overlapped with a dark hole in fluorescence (Figure **4.4d**). Finally, k-means clustering based on several statistics computed from the GCaMP fluorescence image and the phase correlation mask highlighted 2 prominent cluster of neurons, corresponding to GCaMP6 positive excitatory neurons and GCaMP6 negative putative inhibitory neurons (Figure **4.4e**). Similar results were obtained with a classification based on a bilinear fit to central peak of the correlation map against the standard deviation of 5 μm annulus around the peak (Figure **4.4e**).

Unexpectedly, the lateral distribution of putative excitatory and inhibitory neurons around the postsynaptic cells was markedly different. Putative inhibitory neurons tended to be clustered locally around the postsynaptic neurons (Figure **4.4f**), while excitatory inputs were spread out and more evenly distributed over a larger area (Figure **4.4g**). As a result, the difference between the two distributions resulted in characteristic inverse Mexican hat profile (Figure **4.4h**), which suggests that cortical inhibitory inputs outnumber excitatory

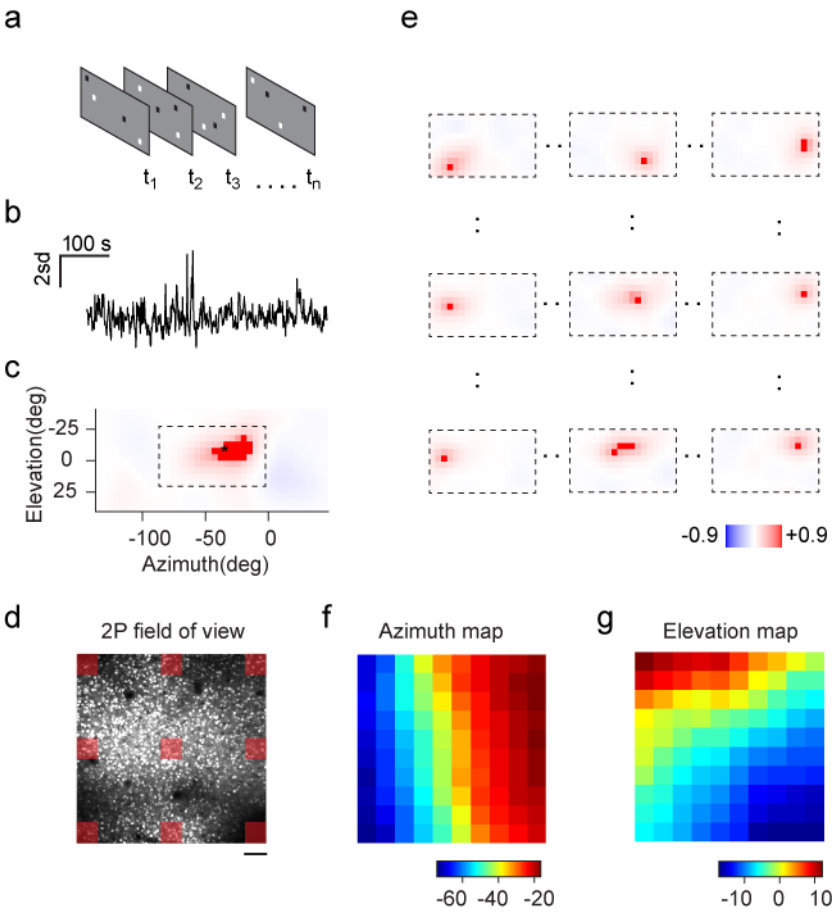

Figure 4.5: Retinotopic mapping from 2P imaging data. (**a**) Sparse noise stimulus used for retinotopic mapping experiments. (**b**) Example average responses across the imaged cortical volume during sparse noise presentation. (**c**) Stimulus triggered average receptive field of the full field of view. The asterisk represents the center of mass of the RF. RF is normalised to the absolute maximum. (**d**) Example time-maximal projection of one imaging plane acquired during sparse noise presentation. The FOV was divided in a grid of 10x10 square sections of interest to compute the retinotopic map: the red squares indicate 9 example such squares. Scale bar 100 µm. (**e**) Stimulus triggered average RF of the sections of interest highlighted in **d.** (**f**) Azimuth retinotopy for the full FOV. Each square represents a tile from the 10x10 grid used to analyse the FOV in **d** (**g**) Same as in **f** for elevation retinotopy**.** Example data from a Camk2a-tTA; EMX1-Cre; Ai94 mouse.

ones in centre of the receptive field, while excitation dominates inputs from the periphery of the receptive field, with a total cumulative imbalance of ~20% of neurons.

4.2.4 Retinotopy of inputs predicts orientation preference of starter neuron

To map the retinotopy of the imaged cortical volume, I performed volumetric imaging while presenting the mouse with a sparse noise stimulus composed of 5 degrees wide black and white squares on a grey background (**Figure 4.5a**). First, I averaged fluorescence changes over the whole imaged volume (**Figure 4.5b**), and mapped the global preferred retinotopic position of the FOV (**Figure 4.5c**). Next, I divided the volume in a grid of 10 x10 square sections (**Figure 4.5d**): I used the global receptive field to constrain the fit of a single preferred retinotopic position for each section (Fig4e). The resulting azimuth and elevation map displayed the hallmark smooth gradient of retinotopy across the FOV (**Figure 4.5e**,**f**,**g**); as previously reported (Garrett et al., 2014), the gradient was almost twice as steep for azimuth than elevation, indicating almost double magnification factor for elevation (**Figure 4.5f**,**g**). The direction of the retinotopic gradient was also used to control the correct sterotaxic targeting of each experiment to the primary visual cortex (Zhuang et al., 2017).

For each starter neuron, I measured the retinotopic distribution of its presynaptic partners, and I termed such distribution 'presynaptic field' (**Figure 4.6**). To this end, I approximated the RF location of the traced neurons as their position in the azimuth and elevation map, and measured the density of inputs as a function of retinotopic distance in azimuth and elevation, producing a smooth 2D map (**Figure 4.6a**,**b**,**c**). Such presynaptic fields were broadly distributed in retinotopic space: 95% of the presynaptic neurons fell within an elliptical field spanning on average 46±3 degrees in azimuth and 26±1 degrees in elevation of the visual field around the location of the starter cell. Such wide sampling of retinotopic space matches the known wide RF of mouse visual neurons (Bonin et al., 2011; Hübener, 2003; Niell and Stryker, 2008).

I then asked if there was a relationship between the orientation preference of the postsynaptic neuron and the retinotopic distribution of the presynaptic field. Mouse visual neurons tend to have indeed an elongated RF (Niell and Stryker, 2008), which is thought to confer the characteristic orientation selective

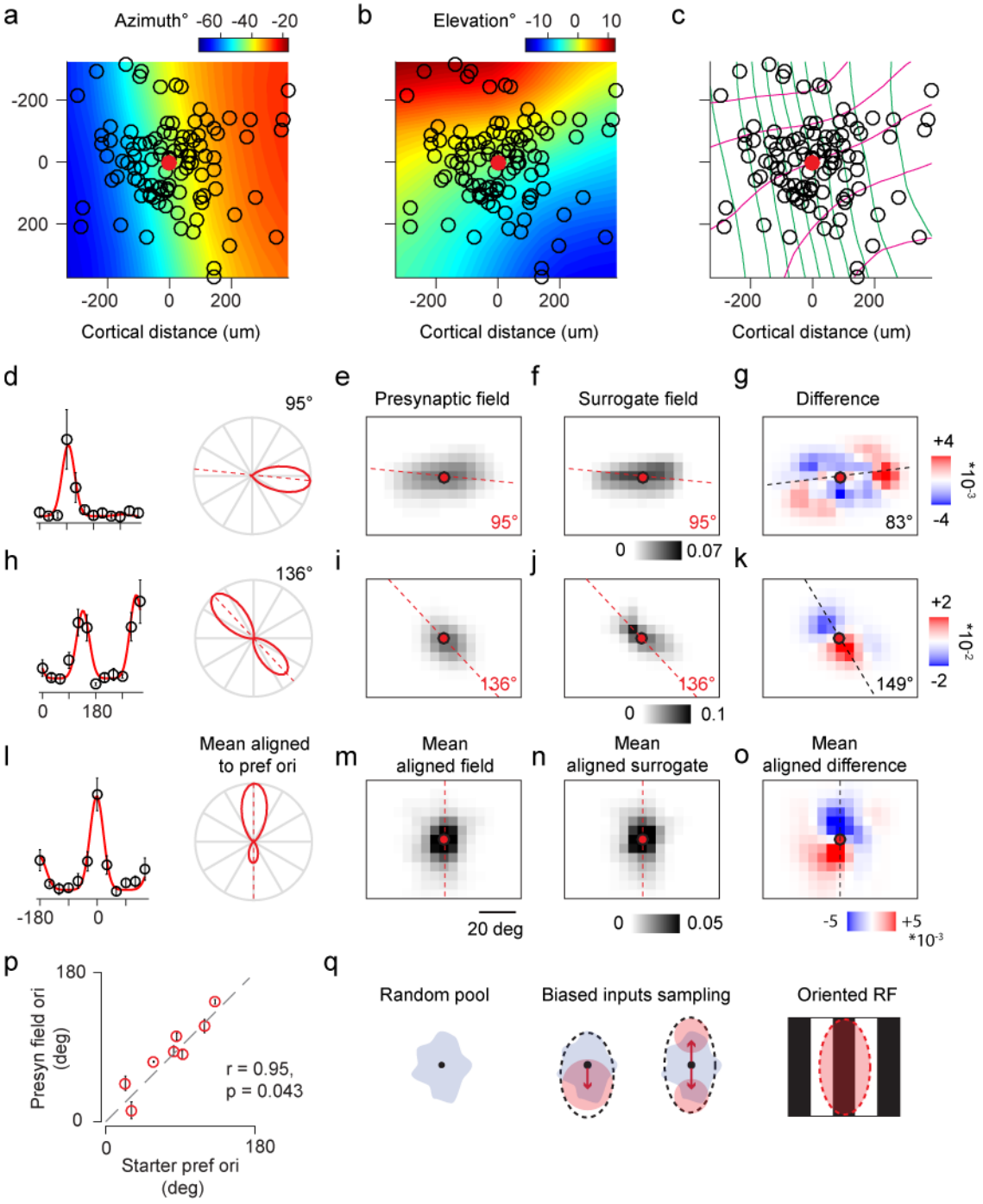

Figure 4.6: Biased retinotopic sampling of inputs correlates with orientation selectivity of starter neuron. (**a**) Overlay of retinotopic azimuth maps and cortical position of an example starter neuron (*red dot*) and its presynaptic inputs (*black circles*). (**b**) Same as in **a** for elevation retinotopic map. (**c**) Representation of retinotopy with iso-azimuth and iso-elevation lines, spaced by 5 degrees, overlaid with the spatial distribution of the example network of neurons. The position of neurons in the retinotopic map was used as a proxy for their RF center. (**d**) Orientation tuning curve for the starter neuron in **a**. Average responses to drifting gratings

(mean ± sem) were fitted with a double Gaussian tuning profile. The polar plot of the same tuning curve highlights the orientation of the preferred grating in retinotopic space (*dotted red line*). (**e**) Presynaptic field for the neuron in **a-d**: probability density of presynaptic neurons as a function of retinotopic distance from the starter neuron. Red dotted line represents preferred orientation of the starter neuron (**f**) Surrogate retinotopic distribution of inputs drawn from a 2D Gaussian distribution in cortical space fit to the presynaptic network in **a-e**. The map shows the average of 100 random draws with the same number of presynaptic inputs of the corresponding starter neuron. (**g**) Difference between the measured presynaptic field in **e**, and the surrogate field in **f.** Red or blue regions correspond to enriched or reduced sampling of inputs with respect to the surrogate field. The black dotted line represents the axis of elongation connecting the centre of mass of enriched and depleted regions of the presynaptic field (**h**, **i**, **j**, **k**) Same as in **d-g** for a second example starter neuron. (**l**) Average tuning curve across the analysed starter neurons (n = 8), aligned to the preferred direction. (**m**) Average aligned presynaptic field across starter neurons: before averaging, distributions were rotated in retinotopic space and aligned according to the preferred direction of movement of the starter neurons. (**n**) Same as in **m** for the surrogate fields. (**o**) Same as in **m** for the difference fields. (**p**) The orientation of the elongation axis of the presynaptic fields in retinotopic space plotted against the preferred orientation of starter neurons, and (circular correlation 0.95, $p < 0.05$). (**q**) Cartoon depicting the proposed model of formation oriented receptive fields from elongated presynaptic fields

responses. To identify the preferred orientation of each starter neuron, I fitted its responses to gratings drifting in twelve different directions with a double-Gaussian tuning curve (**Figure 4.6d**,**h**). In every experiment, the presynaptic

fields were asymmetric, elongated and slanted in retinotopic space, due to the variable magnification factors of azimuth and elevation, and local warping of the retinotopic maps at different eccentricities and in different mice (**Figure 4.6e**,**i**).

To test presynaptic fields distribution independently from the asymmetries due to the local gradient of the retinotopic map, I took advantage of my the detailed measurements of the distribution of presynaptic neurons in cortical space, which demonstrated that such inputs are drawn from a Gaussian distribution falling with lateral distance from the starter cell (**Figure 4.5**). For each experiment, I generated 100 surrogate presynaptic networks, matched in number of traced neurons, and randomly drawn from a Gaussians distribution in cortical space matched in spatial constant to the fit to each presynaptic network (**Figure 4.6f**,**j**). If the measured asymmetry in retinotopic space was just a by-product of the spatial gradient of the retinotopic map, then I would observe no difference between the real and surrogate presynaptic networks.

Instead, the difference between real and surrogate retinotopic distributions of presynaptic neurons displayed regions of consistent enrichment of inputs (red lobes) and other of consistent depletion (blue lobes) (**Figure 4.6g,k**). The presence of both enrichment and depletion regions is a consequence of the fact that density distributions were normalised to 1 before subtraction. These enrichment and depletion regions of inputs were displaced to one another along an elongation axis: in some cases (3/7 networks), the map had 2 enrichment lobes separated by a depletion region **Figure 4.6g**); in other experiments (4/7 networks) the map showed only two main lobes displaced around the position of the starter cell (**Figure 4.6k**). I fitted this elongation axis with a line connecting the centre of mass of the major enriched and depleted input lobe, and measured the orientation of this axis in retinotopic space (**Figure 4.6g,k**).

If the orientation of enriched and depleted presynaptic fields in retinotopic correlates with the orientation preference of the postsynaptic neuron, then they should survive averaging across experiments. To test this hypothesis, I rotated the retinotopic fields, their surrogate, and the difference map for each experiment according to orientation preference of the starter cell, to make this direction vertical (**Figure 4.6i,m,n,o**). Indeed, the average of the aligned presynaptic fields also showed a major enrichment and depletion field displaced around the average post synaptic neurons: importantly, the axis of displacement was now vertical, following the alignment procedure (**Figure 4.6o**). Accordingly, there was strong and significant circular correlation between the orientation preference of the starter neurons and the elongation axis of their presynaptic fields (**Figure 4.6p,r** = 0.95, $p < 0.05$).

These results suggest that V1 neurons select their inputs to produce an oriented receptive field: this selection results in sampling biases that can be either unimodal or bimodal along the preferred orientation of the neuron (**Figure 4.6q**).

4.2.5 Neuropil correction of neuronal responses

Neuronal fluorescence time-courses were corrected for the signal contamination from the surrounding neuropil (Pachitariu et al., 2016). To validate

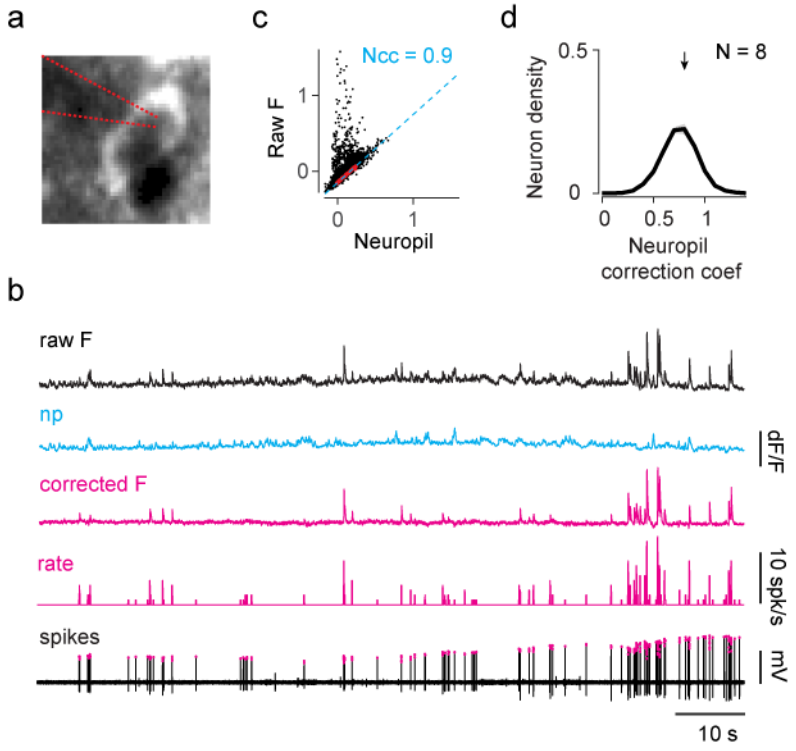

Figure 4.7 Validation of neuropil correction with ground truth recordings. (**a**) Two-photon targeted juxta-somal recording from a GCaMP6s expressing neuron in V1. Red dotted line highlights the patch pipette. (**b**) Data from the example recording in **a**: raw fluorescence trace (*black, top*), neuropil trace computed with Suite2P (*cyan*), neuropil corrected neuronal signal (*magenta, top*), firing rate derived from spikes (*magenta, bottom*), juxta-somal recorded spiking activity (*black, bottom, magenta dots highlight spikes*) (**c**) Raw fluorescence trace plotted against neuropil trace. Neuropil correction factor was computed from linear fit (*cyan line*) to lower envelope of the relationship (*red dots*). (**d**) Population distribution of neuropil correction factor from volumetric 2P imaging during orientation tuning experiments. Arrow indicate median of the distribution. Shaded area represents mean ±s.e.m across 8 datasets.

my neuropil correction method, I carried out targeted juxta-somal patch recording in vivo, to measure spikes from a single pyramidal neuron in V1 while imaging somatic GCaMP6s fluorescence (Figure 4.7a-b). As expected, the fluorescence trace closely followed the spiking activity of the neuron, yet suffered from slow fluctuations and spurious transients inherited from the surrounding neuropil (Figure 4.7b). To correct for such contaminations, I estimated a scaling factor for the neuropil trace by examining the lower envelope of the relationship between neuropil and somatic fluorescence (Figure 4.7c). Then, I subtracted the neuronal signal by the scaled version of the neuropil trace (Peron et al., 2015) (Figure 4.7b). The resulting signal followed more closely the firing rate inferred

from the ground truth spikes (Figure **4.7b**). The same procedure was repeated for every neuron across my recordings, yielding a median neuropil correction factor of 0.80+-0.02 (Figure **4.7d**).

Neuropil signals arise from the averaged activity of many of out-of-focus somas, dendrites and axons: accordingly, in my data, neuropil signals changed smoothly in space, were similar for close neurons, and displayed weakly tuned stimulus evoked transients (Figure **4.8a**). While such contaminations were smaller than the signals from the neurons of interest, they were consistent and reliably stimulus locked (Figure **4.8a**). Therefore, they contributed substantially to stimulus trigger averages and must be accounted for. Strongly responsive neurons were affected least by the corrections, while unreliable or highly selective neurons benefited a lot from the removal of neuropil un-tuned contaminations (Figure **4.8a**). Strikingly, many cells that would have been classified as responsive, revealed themselves as silent after neuropil correction (Figure **4.8a**).

At the population level, the neuropil correction impacted the data in two ways: it revealed greater stimulus selectivity for responsive neurons, without substantially affecting the estimation of the preferred orientation (Figure **4.8b**); furthermore, perhaps most crucially, it was essential to discard from further analysis neurons that, once corrected, did not show significant stimulus evoked activity (Figure **4.8c**). Neuronal signals were tested for significant stimulus responses before and after neuropil correction: I classified neurons as 'responsive accepted', if they passed the test both before and after the correction, or as 'responsive rejected', if they failed the test after neuropil correction (Figure **4.8b-c**). Finally, I compared the statistics of orientation tuning among four classes of signals: neuropil corrected responsive accepted neurons; raw responsive accepted neurons; raw responsive rejected neurons; neuropil signals from both responsive accepted and rejected neurons (Figure **4.8d-e**). Neuropil signals were largely untuned, showed weak orientation selectivity and were predominantly biased for cardinal directions (Figure **4.8b-e**). They contributed a small amount to the activity of responsive accepted units: while the correction did not change

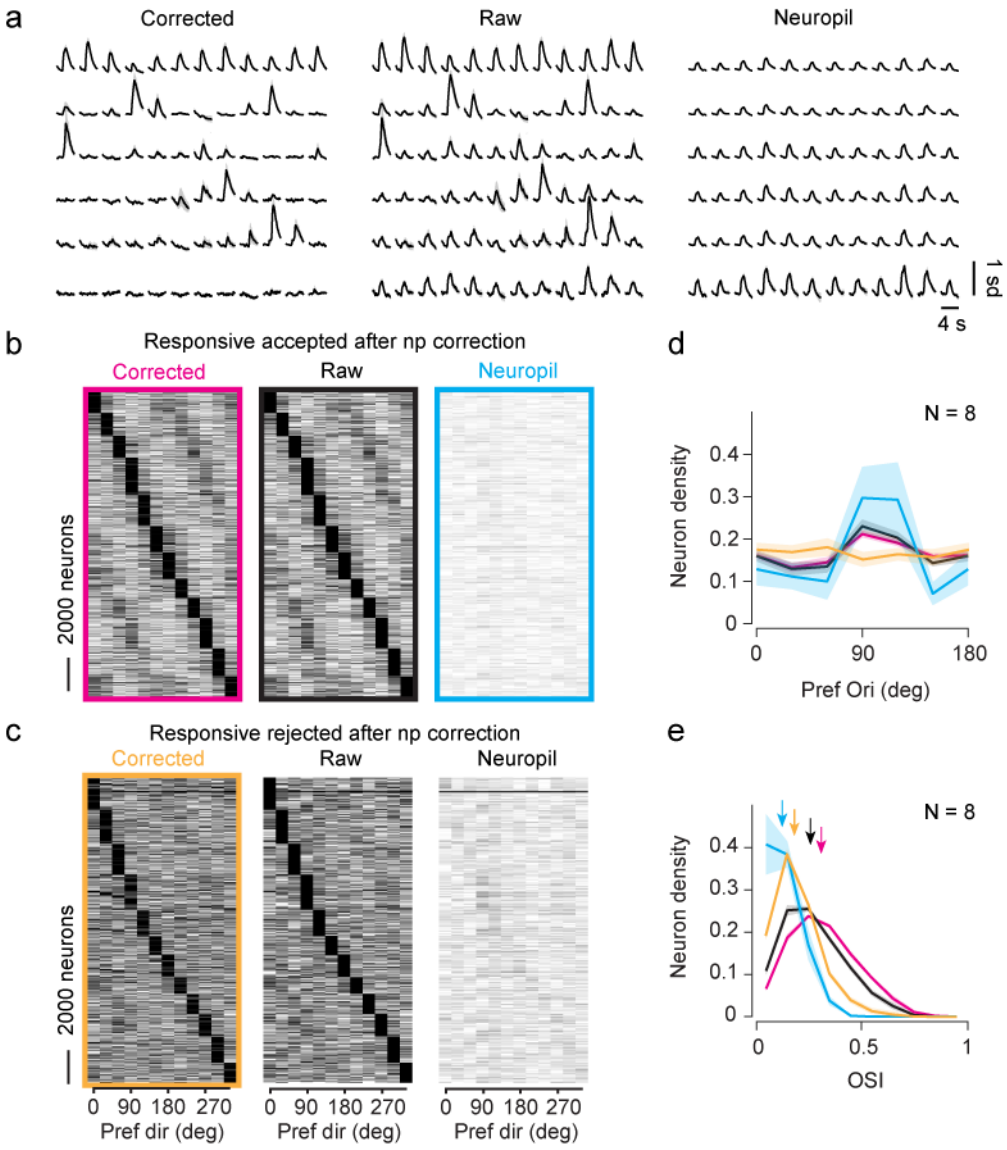

Figure 4.8 Functional relevance of neuropil correction. (**a**) Responses to gratings from six example neurons in a Camk2a-tTA; EMX1-Cre; Ai94 mouse: neuropil corrected responses (*left*), raw responses (*middle*), neuropil contamination (*right*). Traces are mean±s.e.m. (**b**) Average responses to drifting gratings from responsive accepted neurons pooled across experiments (n = 19748). The response to each grating is measured as the integral below the GCaMP trace, and summarised in the matrix, where rows represent neurons and columns represent the intensity of the response to a specific direction. Responses where normalised between 0 (white) and 1 (black). Rows are sorted according to the preferred direction. Neuropil corrected responses (*left*), raw responses (*middle*), neuropil contamination (*right*) (**c**) Same as **b** for responsive rejected neurons (n = 20526). (**d**) Population distribution of preferred orientation, averaged across datasets (N = 8), for responsive accepted neuropil corrected neurons (*black*), responsive accepted raw neurons (*magenta*), responsive rejected raw neurons (*yellow*), and neuropil traces (*cyan*). (**e**) Population distribution of orientation selectivity index, averaged across datasets (N = 8), for responsive accepted neuropil correc. ted neurons (*black*), responsive accepted raw neurons (*magenta*), responsive rejected raw neurons (*yellow*), and neuropil traces (*cyan*). Arrow represent medians of the distributions. Data are mean ±s.e.m.

their stimulus preference substantially, it significantly increased their orientation selectivity (Figure **4.8b, d-e**). Conversely, neuropil signals dominated the weak and noisy responses from the 'responsive rejected' units: many changed stimulus preference after the correction, while their orientation selectivity remained weak, similarly to the neuropil (Figure **4.8c, d-e**).

4.2.6 Orientation tuning of presynaptic networks

Many presynaptic neurons (53±7%) displayed activity-dependent fluorescence changes during two-photon imaging recordings. These neurons were classified as active ROIs by an automated image segmentation pipeline (Pachitariu et al., 2016), and were therefore considered visually responsive excitatory neurons.

We sought to determine the similarity between the sensory responses of the starter neurons and its presynaptic network. The majority (7/9) of the starter neurons significantly responded to the presentation of drifting gratings (**Figure 4.9a-c**). Among the traced presynaptic neurons, 32±2% (17±3% of the total) responded to gratings motion (Figure **4.9d-j**). Response were judged significant if the neuron had either a maximal average response greater than 2 times the standard deviation of the traces during the blank stimuli or an OSI or DSI greater than 0.2; moreover, they had to pass a one-way ANOVA across stimulus conditions and have maximal stimulus response significantly greater than the response to a blank stimulus.

We first quantified the responses to drifting gratings recorded across all traced networks. This also served as a control for the health of the traced neurons. All presynaptic networks contained both direction and orientation selective neurons, with preference ranging across all the shown directions of motion (**Figure 4.9d,e**). Besides the preferred direction, the degree of selectivity varied from neuron to neuron: some were extremely direction selective (DSI > 0.5), others very orientation selective (OSI >0.5), other responded to most of the stimuli (median OSI =0.32, median DSI = 0.18). While recent studies have suggested a prevalence

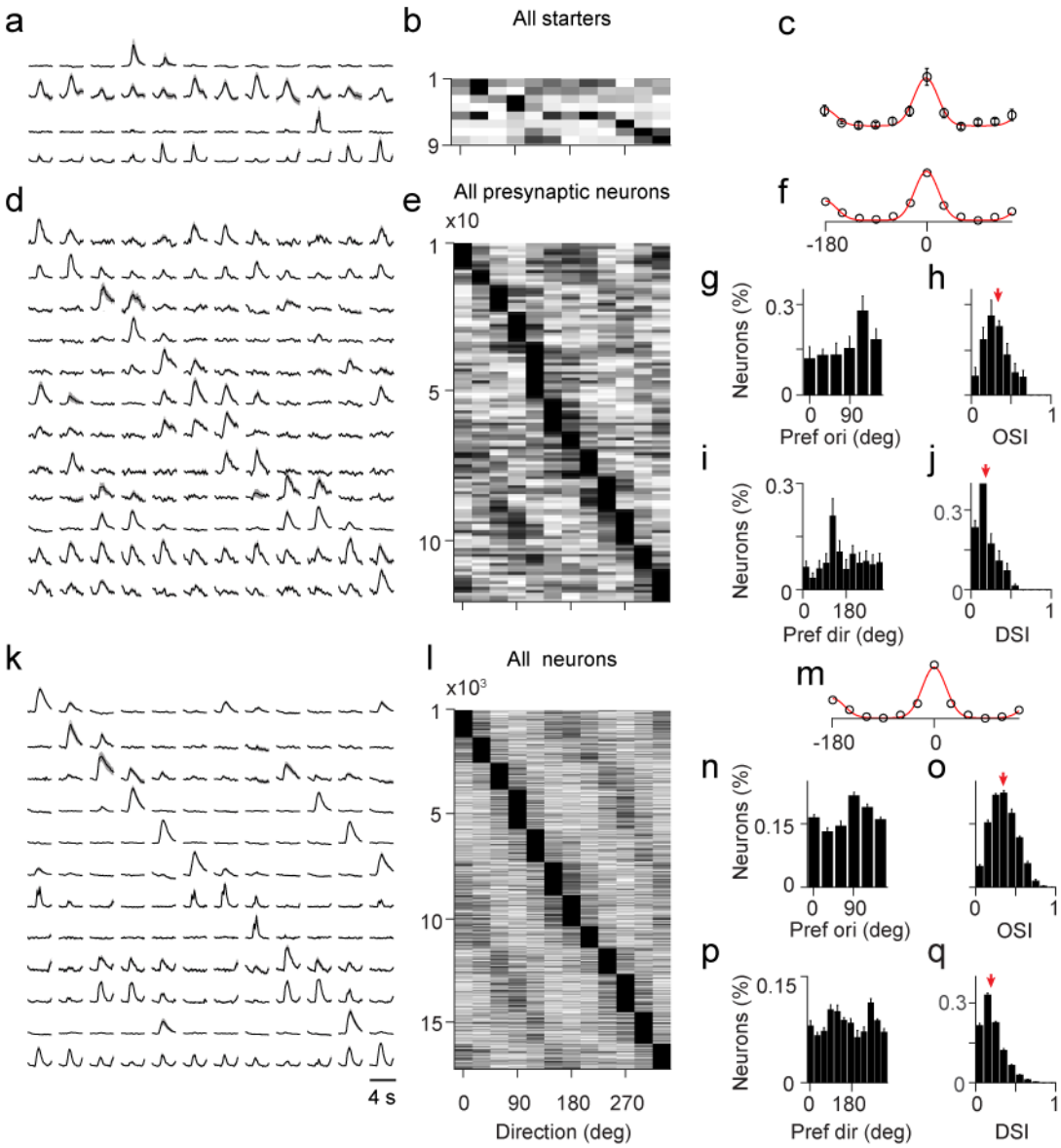

Figure 4.9: Orientation and direction selectivity of the traced neurons and surrounding excitatory population. (**a**) Responses to drifting gratings from four example starter neurons. Rows represent neurons, columns represent grating directions, data are mean ± sem. Rows are sorted according to the preferred direction. (**b**) The response to each grating is measured as the integral below the GCaMP trace, and summarised in the matrix, where rows represent neurons and columns represent the intensity of the response to a specific direction. Responses where normalised between 0 (white) and 1 (black). Rows are sorted according to the preferred direction. (**c**). Average tuning curve across the starter neurons, aligned to preferred direction. (**d-f**) Same as **a-c** for the rabies traced neurons across presynaptic networks (n = 8) (**g**) Distribution of orientation preference across neurons in all the traced presynaptic networks. (**h**) Distribution of orientation selectivity index across traced neurons. (**i**) Distribution of direction selectivity across traced neurons. (**j**) Distribution of direction selectivity index across traced neurons. (**k**, **l**, **m**, **n**, **o**, **p**, **q**), Same as in **d-j** for all the excitatory neurons recorded across layers across mice (n = 8). Red arrows indicate the median of the distributions.

of responses to the horizontal direction of motion (Hillier et al., 2017), I found a bias in the representation of the cardinal vertical direction of motion (Fig6 g,i).

To ask whether these statistics of orientation and direction selectivity were comparable in the surrounding population, I quantified the responses of unlabelled neurons recorded during the same imaging sessions, pooled across experiments (**Figure 4.9k-p**, 17,190 visually responsive neurons in total). As previously reported, excitatory neurons showed highly direction selective responses, representing the whole range of presented stimuli (**Figure 4.9k, l**). I found a broad range of orientation and direction selectivity, ranging from 0.1 to 0.8 (**Figure 4.9o,q**, median OSI = 0.34, median DSI = 0.18): this result is consistent with the fact that I pooled responses across superficial and deep layers, which contain population of narrowly and broadly tuned neurons

(Niell and Stryker, 2008; Sun et al., 2015). The population distribution of OSI and DSI was not significantly different than the one measured in rabies traced neurons (Kolmogorov-Smirnov test, p = 0.35 for OSI, p =0.943 for DSI). The population data confirmed a global overrepresentation of horizontal orientation with the vertical direction of motion (**Figure 4.9m,p**).

I then asked whether the distribution of orientation tuning measured for each presynaptic network correlated with the orientation preference of the corresponding starter neuron (**Figure 4.10**). To control for the population wide bias for horizontal gratings, I first analysed the population distribution of orientation tuning recorded in each mouse. I confirmed that in each experiment there was indeed an overrepresentation of horizontal gratings, and that the circular asymmetry of the measured preferred orientation distributions was significant for all mice (**Figure 4.10a-h,** Rayleigh test). The average across mice showed a significant enrichment of neurons preferring horizontal gratings.

For each presynaptic network, I aligned the distribution of preferred orientation to the selectivity of the starter neuron (**Figure 4.10i-o**). I found that neurons within each presynaptic networks were tuned to a broad range of orientations: the distribution of preferred orientation for most presynaptic networks did not

show a bias for the preferred orientation of the starter cell. Only one presynaptic network significantly over-represented the preferred orientation of the starter cell (**Figure 4.10i**, Rayleigh test, $p < 0.05$). Yet, on average, there was no tuning toward the preferred orientation of the starter cell (**Figure 4.10p**).

I finally tested if the global population bias could 'hide' an enrichment of neurons sharing the same orientation tuning of the postsynaptic. To test this hypothesis, I divided the distribution of preferred orientation in each presynaptic network by the distribution of preferred orientation of the surrounding neuronal population (**Figure 4.10q-r**). The resulting distribution seemed to reveal in some cases a relative enrichment of the orientation preference of the starter cells in the presynaptic neurons when compared to the population data(**Figure 4.10r,t**), yet neither individual networks, nor their average distribution, were significantly tuned to a particular orientation (**Figure 4.10q-x**, Rayleigh test > 0.05).

4.3 Discussion

In this study, I combined single neuron-initiated monosynaptic rabies virus tracing (Marshel et al., 2010; Vélez-Fort et al., 2014; Wertz et al., 2015) and two-photon microscopy (Denk et al., 1990) to characterise the functional organisation of presynaptic networks upstream to L2/3 pyramidal neurons in the primary visual cortex of awake mice. I targeted the starter neurons with red fluorescent proteins, and traced their inputs with a rabies virus expressing a similar red reporter to provide a detailed description of their dendritic morphology, and the anatomical distribution of their inputs in cortical space. Moreover, I deployed these techniques in transgenic mice expressing the genetically encoded calcium indicator GCaMP6 (Madisen et al., 2015; Wekselblatt et al., 2016): I mapped the retinotopic organisation of the visual cortex; I recorded the responses of traced neurons to the directional motion of drifting gratings and compared them to the surrounding population of neurons. Such novel approach allowed to characterise for the first time the functional architecture of presynaptic networks in retinotopic space, and compare this architecture to the orientation selectivity of

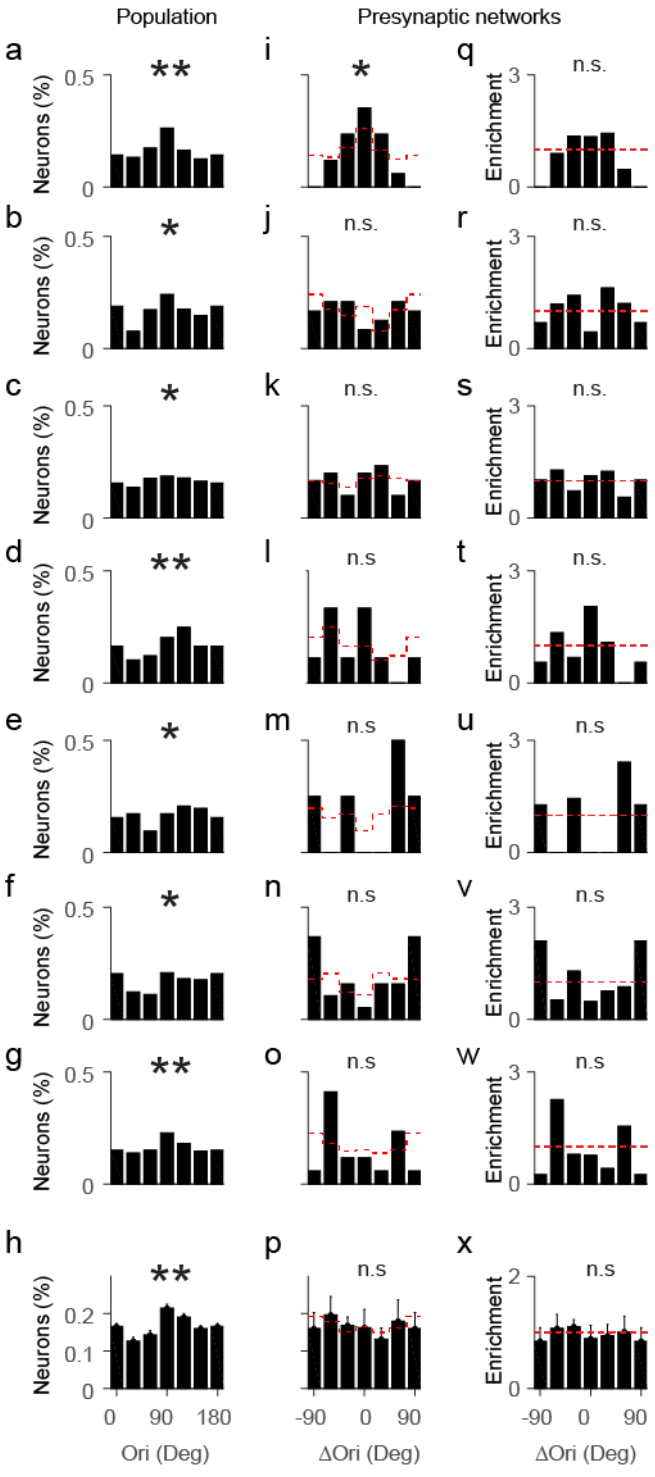

Figure 4.10: Distribution of orientation preference in presynaptic networks and surrounding population. (**a-g**) Distribution of preferred orientation recorded from excitatory neurons across layers in V1. Each panel shows data from a different animal. (**h**) Average distribution of preferred orientation across animals (n = 7). (**i-o**) Distribution of preferred orientation in presynaptic networks upstream of L2/3 neurons. Each panel shows data from a different presynaptic network; the distribution was aligned to the orientation preference of the post-synaptic neuron. The red dotted lines represent the population data from the same animals, shown in panels **a-g**, after alignment to the preference of the postsynaptic neuron. (**p**) Average distribution of aligned preferred orientation across networks. The red dotted line represents the average of the population distribution after alignment. (**q-w**) Enrichment of preferred orientations in presynaptic networks obtained by dividing the distribution of preferred orientations, aligned to the preference of the postsynaptic neuron and divided by the aligned population distribution. (**x**) Average enrichment of preferred orientations across animals. In all the plots, asterisks or n.s. indicate the p value of a Rayleigh test for circular unimodal biases (n.s. = $p>0.05$, * = $p<0.05$, ** = $p<0.01$).

the starter neurons. Finally, I began to dissect the relationship between the responses to image motion of the starter neurons and their presynaptic partners.

The starter neurons targeted in this study had the distinctive morphological traits of L2 intra-telencephalic (IT) neurons (Harris and Shepherd, 2015): they belonged to superficial L2/3, they extended ramified apical dendrites in L1 and had dense basal dendrites arborisation locally in L2/3. Indeed, besides the abundant local inputs from L4, L2/3 and L5 that target their basal dendrites, L2 IT neurons are known to receive direct inputs both from primary thalamus, higher order thalamus and association areas in L1. Noticeably, their apical dendrites in L1 are targeted by thalamo-cortical neurons located in the shell of the lateral geniculate nucleus, which relay information from retinal direction selective ganglion cells (Cruz-Martín et al., 2014). Indeed, many of my starter neurons that responded to drifting gratings where highly direction selective (4/7). Moreover, post-hoc histological analysis from my experiments confirmed the presence of some monosynaptically traced thalamic neurons, as well as many feedback projections from higher visual areas and associative cortices (Wertz et al., 2015).

The anatomical distribution of the traced presynaptic networks revealed that L2 IT receive most of their inputs from neurons displaced ~100-200 µm in cortical space, although pairwise connection probability with neighbours falls with distance with a space constant of ~130 µm. These results might explain earlier connectivity mapping in slice, that reported that while pairwise connection probability declined with cortical distance(Song et al., 2005), the occurrence of higher order connectivity motifs peaked between 100-150 µm of inter-somatic distance (Perin et al., 2011). The analysis of the layer distribution of presynaptic neurons showed that while L2 IT neurons sample more densely inputs from L3, they also receive substantial connections from L4 neurons. Despite the difficulties of imaging deeper than 500µm in the cortex, I was also able to detect several traced neurons in L5. While my approach did not allow to quantify the strength of synaptic connections, my data suggest that recurrent inputs from local L2/3 peers play a major role in shaping the computation of L2 IT neurons.

I discovered that the presynaptic network is organised in retinotopic space to form an elongated 'presynaptic field', whose orientation in retinotopic space matches the orientation preference of the postsynaptic cell. In other words, the retinotopic organisation of the presynaptic inputs predicts the orientation selectivity of the postsynaptic cell. My data suggest that while the retinotopic organisation of presynaptic field is strongly biased by the local gradient of the retinotopic map (Garrett et al., 2014), neurons tend to sample more inputs from regions of the retinotopic space that are displaced along the axis representing their preferred orientation. Such novel organising principle of functional connectivity in might underlie the formation of oriented receptive fields that contributes to orientation selective responses in V1 (Kaschube, 2014). A similar functional connectivity rule has been described in the visual cortex of ferrets, whereby retinotopy and orientation column can be mapped to predict the connection patterns between L4 neurons with center-sorround RF and L2/3 neurons with elongated, orientation selective RF (Mooser et al., 2004). Nonetheless, a similar principle has never been demonstrated tracing inputs on a single neurons basis.

Consolidation of these results will require further control analysis and an expanded dataset. For instance, neuronal RF were estimated using the somatic position of cells on the mean field retinotopic map. While such approximation was convenient to measure the RF centre even for neurons that did not show robust responses to sparse noise stimuli or neurons that did not express GCaMP at all, it has been reported that RFs can have substantial local jitter with respect to the continuous retinotopic map (Bonin et al., 2011). Nonetheless, further analysis of the data discussed herein (Rossi et al. 2017a), together with previous published work (Bonin et al., 2011; Kremkow et al., 2016), suggests that the error in the estimates of RF location from retinotopy is minimal, even after neuropil correction (Rossi et al. 2017a). Moreover, my analysis of responses to sparse noise stimuli did not consider shifts in stimulus position caused by eye movements occurring in awake mice (Payne and Raymond, 2017). While head-fixed mice display reduced eye movements, mostly constrained to the horizontal direction,

these gaze shifts might be sufficient to blur or bias the estimates of the retinotopic map or the fit of neuronal RF (Payne and Raymond, 2017). The eye-tracking data recorded during my experiments will allow to control for these artefacts.

I found that the tuning of neurons in each presynaptic network is heterogeneous and is not necessarily aligned to the orientation preference of the corresponding starter neuron. These results are not in agreement with many previous studies in mice, that reported preferential connectivity among neurons with similar orientation tuning (Bock et al., 2011; Cossell et al., 2015; Hofer et al., 2011; Wertz et al., 2015). The discrepancy with previous findings might arise from the technical pitfalls peculiar to the methods used in previous studies or the ones used in my investigation. Firstly, none of the previous functional connectivity studies properly corrected their two-photon imaging data for neuropil contamination. This pitfall is particularly important given the abundant evidence, confirmed in my study, of a significant overrepresentation of cardinal directions by visual neurons(Hillier et al., 2017; Kondo and Ohki, 2015; Sun et al., 2015). Omission of a conservative neuropil correction might bias measurements of functional connectivity, generating an artefactual bias for connected neurons to share the same orientation tuning, while this effect is simply inherited from biases inherent in the sampled population. While studies employing GCaMP6 functionalised rabies virus potentially resolved the neuropil contamination problem by sparsely labelling only the traced neurons (Wertz et al., 2015), they could not measure responses from the surrounding neuronal population, and therefore could not evaluate their result in the context of population responses. Nonetheless, even the cortex-wide expression of GCaMP6 I deployed has its drawbacks: indeed, I selected active presynaptic neurons based on the overlap between the rabies driven dsRed signal and the detection of an active ROI from an image segmentation software. This procedure might yield spurious ROIs corresponding in fact to bright neuronal processes running in the proximity of a rabies traced soma, and ultimately contaminate the results with responses from false positive neurons. Finally, many of previous studies analysed functional recordings under anaesthesia, and sparsely sampled the tuning of neurons with

only eight orientations. Instead, I performed imaging experiments in awake behaving mice and measured tuning curves at a finer scale. A more accurate analysis of eye movements and behavioural changes during my experiments, together with a better quantification of the responses of presynaptic neurons will test the relevance of these concerns.

Nonetheless, the results of the thesis are not necessarily in contrast with current models of V1 cell's orientation selectivity (Priebe, 2016), posing that tuning for the preferred direction is primed by feed-forward inputs from LGN (Lien and Scanziani, 2013), and amplified by similarly tuned driver cortico-cortical connections (Cossell et al., 2015). In this framework, global, or broadly tuned, suppression is supplied by feed-forward cortical inhibition (Hofer et al., 2011), to further sharpen the responses and preserve contrast invariant tuning (Priebe, 2016). While investigation of local connectivity in slices confirmed the tendency of neurons to receive the stronger synapses from similarly tuned peers (Cossell et al., 2015), these synapses were a minority, and there was only a weak correlation between connection probability and tuning similarity (Ko et al., 2011). Moreover, a recent rabies virus tracing study reported that presynaptic inputs from L4 and L5, but not L2/3, can indeed have variant orientation tuning when compared to the postsynaptic neurons (Wertz et al., 2015). Therefore, the majority of cortico-cortical synapse could be 'modulatory', and come from neurons with different tuning. These inputs, while broadly tuned, might contribute to tuning via coaxially organised retinotopic drive, as demonstrated herein. Most importantly, they could underlie response specialisation to more complex stimuli such as plaids (Juavinett and Callaway, 2015) and natural stimuli (Ko et al., 2013), or constitute a pool of connections available for plastic changes and adaptation. Furthermore, while I could not assess the functional properties of inhibitory presynaptic inputs in this thesis, I found that excitatory presynaptic neurons are distributed more broadly than inhibitory presynaptic neurons in cortex. These distant connections might serve a different purpose than amplification of local features, perhaps contributing to sensory binding of stimuli beyond the classical RF.

Chapter 5

Imaging focuses on epileptic networks at multiple scales

5.1 Introduction

Epilepsy is a common neurological disorder which affects ~1% of the world population (England et al., 2012). It is characterized by recurrent episodes of abnormal and excessive neuronal activity. When these episodes are accompanied by motor, sensory or other symptoms the episodes are called seizures. In many patients, seizures arise from a localized cortical focus and then propagate to nearby or distant regions: such manifestations are termed focal, or partial onset, seizures. If dysfunction or lesion of a cortical region leads to a positive or negative symptom (for instance, perception of a flash of light or disturbance of language production), that region is said to be 'eloquent cortex'. In other instances, patients experience primary generalized seizures, which entail simultaneous bilateral epileptic discharges and are thought to be of subcortical origin (Sorokin et al., 2016).

It is unclear why aberrant escalating activity escapes the physiological regimes of operation of cortical networks. For this and other reasons, drug treatment of epilepsy remains sub-optimal: in about 30% of cases, drugs fail to control seizures or only do so at doses that lead to unacceptable side effects (Perucca and Gilliam, 2012)(Laxer et al., 2014). This is not entirely surprising because drugs do not differentiate between neurons involved in seizure generation and spread and neurons elsewhere in the brain.

Unravelling the mechanisms underlying the development of epilepsy (i.e. epileptogenesis) and the generation of seizures (i.e. ictogenesis) requires to study brain networks at multiple scales. At the ictogenic focus, acquired lesions or

congenital abnormalities (Wiebe and Jette, 2012) predispose to aberrant recruitment of neuronal activity. In some but not all cases morphological abnormalities can be detected at the cellular or macroscopic level. Changes in neuronal excitability and dysfunctional neuron-glia interactions have also been reported in some experimental models (Paz and Huguenard, 2015).

If we are to dissect how such changes affect the wiring and balanced operation of different excitatory and inhibitory neuronal classes, we must record from densely packed neuronal populations, ideally with single cell resolution (Wenzel et al., 2017). Yet, none of the circuitry at the ictogenic focus operates in isolation, rather is embedded in an intricate network, where local and distal brain areas are connected by short and long range neuronal collaterals. Understanding which pathways support and sustain seizure requires recordings of brain wide networks (Goodfellow et al., 2016). Therefore, only a detailed understanding of local and global mechanisms triggering epileptic networks can lead to the identification of target 'choke points' to design new therapeutic strategies.

Electrophysiological recordings have always been the gold standard to recognize and study epileptic activity in the brain (Steriade and Contreras, 1998). However, even state-of the-art high density surface arrays suffer from significant limitations in localizing neuronal activity due to volume conduction and low spatial sampling (Viventi et al., 2011). Alternatively, single unit recordings with multisite probes only sample local neuronal activity sparsely; moreover, they are difficult during seizures, because excessive firing distorts action potential waveforms and jeopardize spike sorting (Merricks et al., 2015). While these techniques remain extremely valuable, not least because they can be applied in human patients to help identifying the epileptogenic focus (Schevon et al., 2012; Truccolo et al., 2011), their insufficient spatial sampling and scalability has slowed down the understanding of epileptic manifestations in experimental work on animal models.

Two state of the art optical imaging methods, two-photon microscopy (Denk et al., 1990) and widefield fluorescence imaging (Ratzlaff and Grinvald, 1991),

offer the spatial resolution and scalability to complement electrophysiological methods in the quest to reveal the mechanisms underlying epileptic networks at different scales. A wide palette of genetically encoded activity reporters can be used to measure membrane potentials(Akemann et al., 2012), spiking (Chen et al., 2013), the concentrations of intracellular ions (Arosio et al., 2010) or neurotransmitter release (Marvin et al., 2013). Specificity is the key: genetically encoded indicators can be targeted to specific neuronal population and allow long-term, chronic recording from cortical and subcortical structures (Madisen et al., 2015). Ultimately, these techniques promise to play a crucial role in understanding both epileptogenesis and ictogenesis.

In this chapter, I will offer a perspective on how novel functional optical imaging approaches can be used to reveal the principles governing epileptic networks. I will describe how innovative imaging technologies can be used to study the circuit mechanisms underlying seizures at multiple scales, from interactions between brain areas down to the contribution of different neuronal classes to seizure initiation, propagation and termination. I will review the results of pioneering studies that have used imaging. Finally, I will outline the open questions and highlight how innovative imaging approaches will drive future investigations and help design novel therapeutic avenues.

5.2 Novel optical imaging methods to boost epilepsy research

Two-photon microscopy (Denk et al., 1990) and widefield fluorescence imaging (Ratzlaff and Grinvald, 1991) represent the two state of the art imaging methods to complement electrophysiological recordings of neuronal activity during epileptic activity. For equal temporal resolution, the two techniques offer a trade-off between spatial resolution and scale: two-photon imaging achieves sub-micrometric resolution over a ~1mm field of view, while wide-field imaging allows recording from the whole cortical surface with a lateral resolution of ~50-100um. Nonetheless, modern imaging technologies are quickly increasing the bandwidth and temporal resolution (Ji et al., 2016). Hence, it is tempting to

extrapolate to the day a single setup will allow imaging the entire cortical surface of the mouse brain with single cell resolution and single action potential resolution (Reid, 2012).

All methods of functional fluorescence brain imaging rely on fluorescent reporters of neuronal activity. An ever-improving array of fluorescent reporters of neuronal activity allow to tailor the technique to record different aspects of cellular physiology(Lin and Schnitzer, 2016). Calcium indicators gauge neuronal spiking from the intracellular dynamics of calcium (Vogelstein et al., 2010): their high signal to noise ratio and broad dynamic range make them the most widely used reporters of neuronal activity (Grienberger and Konnerth, 2012). However, in principle, only voltage indicators have a sufficient temporal resolution to record single spikes and the ability to measure sub-threshold activity (Akemann et al., 2012). Nonetheless, voltage indicators have a lower SNR than calcium indicators and they are bound to the cellular membrane, hampering single cell resolution in packed neuronal networks (Akemann et al., 2013). Interesting emerging reporters measure other important aspects of neuronal activity: iGluSnFr measures glutamate release (Marvin et al., 2013), while Chloride indicators can gauge the effects of inhibition (Arosio et al., 2010).

The advent of genetically encoded fluorescent reporters fostered an explosion of imaging methods in neuroscience (Lin and Schnitzer, 2016). Molecular engineering constantly improves and expands the palette of genetically encoded reporters and actuators (Chen et al., 2013; Dana et al., 2016). Advanced mouse transgenic technologies (Madisen et al., 2015) and designer viral vectors (Chan et al., 2017) are routinely used to deliver stable non-cytotoxic expression of reporters in neurons. In parallel, cranial window preparations for chronic imaging became increasingly robust, allowing activity to be monitored for many hours over the course of weeks and in awake animals (Goldey et al., 2014). Perhaps most importantly, intersectional expression strategies based on DNA recombinase or inducible promoters can be used to timely tag different neuronal classes. As a result, green and red sensors can be targeted to allow simultaneous multiplexed recordings from genetically identified neuronal population (Dana et

al., 2016); alternatively, they can be spectrally matched with a wide array of optogenetic actuators to provide simultaneous readout and control of neuronal activity (Packer et al., 2014).

Widefield imaging macroscopes (Ratzlaff and Grinvald, 1991) allow to record activity over the whole cortical surface (Mohajerani et al., 2013), representing a substantial advance over superficial electrophysiological recordings performed at a few sites. Widefield imaging can be used to map the organization of cortical areas and map the topology of functional connectivity and correlations between them (Kalatsky and Stryker, 2003; Mohajerani et al., 2013). Moreover, wide field imaging has been deployed alongside multisite electrode probes to correlate cortical activations patterns with neuronal activity recorded in deep brain structures (Xiao et al., 2017). These setups are relatively inexpensive to build, with the best optics and cameras that can achieve a spatial resolution of ~50um and temporal resolution up to 100Hz. Multispectral widefield imaging (Bouchard et al., 2009) is capable of measuring simultaneously signals from cortical populations of excitatory and inhibitory neurons, provided they are targeted with green and red activity reporters. Alternatively, ratiometric imaging allows parallel recording of neuronal and haemodynamic activity (Carandini et al., 2015).

Two-photon scanning microscopy (Denk et al., 1990) can achieve recording from 10'000 neurons in a densely packed cortical column (Pachitariu et al., 2016), an impossible target even for the most advanced electrode array. Two-photon fluorescence excitation provides with sub-micrometric spatial resolution; moreover, the low scattering of infrared excitation laser in the brain tissues, permits imaging down to 1mm. Efforts to engineer adaptive optics and 3-photon microscopy systems are pushing this limit further, achieving two-photon recordings in the mouse hippocampus (Ouzounov et al., 2017). In addition, cranial windows can be customized with prisms (Andermann et al., 2013), GRIN lenses or periscopes (Barretto et al., 2009) to allow coronal imaging of cortical layers or recordings from deep brain structures, respectively. Recently, high speed resonant scanners have been combined with piezo-electric scanning of the

microscope objective to achieve 3D volumetric imaging of entire 1mm3 cortical columns (Göbel et al., 2007). Alternatively, ultra-wide field 2P microscopes allow imaging over almost an entire hemisphere of the mouse brain(Ji et al., 2016). Consequently, two-photon datasets are growing in size and complexity: luckily, automated pipelines for image registration, segmentation of ROIs and deconvolution of neuronal activity are also constantly improving and freely available (Pachitariu et al., 2016).

5.3 Imaging epileptic networks: harvesting the first results

Nearly two decades ago, Schwartz et al first demonstrated that intrinsic optical imaging of haemodynamic signals could be used to localise in the cortex the hallmarks of epileptic activity such as interictal foci, ictal foci, and propagation to secondary foci (Schwartz and Bonhoeffer, 2001). Now, several years down the road, studies are starting to harness the greater spatial and temporal resolution of fluorescence optical imaging to study in detail the circuit mechanism of epileptic discharges in pharmacological and genetic models of epilepsy. Much of this work focused on focal cortical epilepsy, which can be modelled pharmacologically by local applications of GABAa antagonists, K-channel blockers and muscarinic agonists: particularly, these studies leveraged on refined preparations for chronic imaging in awake animals, which avoided the confounding effects of anaesthesia, which often make it difficult to induce seizures.

Two-photon imaging studies are unveiling the complex spatio-temporal dynamics of neuronal recruitment during interictal and ictal activity *in vivo*. These works are challenging the long-standing view of epileptic discharges as highly stereotyped events. Two-photon calcium imaging in the hippocampus mapped patterns of neuronal recruitment during interictal spikes (induced contralaterally), and demonstrated a heterogeneous pattern of activation despite seemingly stereotypical LFP events (Muldoon et al., 2015). Neuronal recruitment during the propagation of ictal discharges was investigated in the visual cortex,

where high speed 2P imaging was used to monitor neuronal dynamics across layers. Results suggest that seizures spread reliably, with repeated cell-wise and layer-wise recruitment patterns, yet with greatly variable recruitment durations and lags in absolute time (Wenzel et al., 2017). This elasticity is controlled by inhibitory interneurons, as local GABAA-R blockade abolishes the phenomenon.

The variability, and elasticity, of neuronal recruitment during the progression of interictal and ictal events seems to be controlled by GABAergic interneurons. Targeted two-photon recordings from parvalbumin positive interneurons expressing GCaMP6 showed that these neurons are recruited by feedforward excitation barrages from the focus before the local excitatory circuit is invaded by the seizure (Liou et al., 2017; Muldoon et al., 2015). Because compromising local inhibition with GABAA-R blockade leads to quick recruitment of local excitatory cells into the seizures(Wenzel et al., 2017), it has been hypothesised that the propagation of seizure to healthy regions depends on the failure of this feed-forward inhibition, either because interneurons themselves fail to fire or release GABA, or because postsynaptic chloride gradients collapse, compromising voltage inhibition (Trevelyan et al., 2007).

Calcium imaging has also played a prominent role in defining the importance of astrocytes in modulating neuronal activity during ictogenesis (Carmignoto and Haydon, 2012; Losi et al., 2017). Indeed, while astrocytes are not electrically excitable cells, they signal their activity with prominent intracellular calcium oscillations. Astrocytes are crucial for the homeostasis of extracellular K concentration and clearance of neurotransmitter from the extracellular space; moreover, they listen to neuronal activity at 'tripartite' synapses and talk back to neurons releasing several gliotrasmitters (Araque et al., 2014; Bazargani and Attwell, 2016). Accordingly, many evidence from in situ studies suggest that they could causally promote ictogenesis mediating neuronal excitation and synchrony(Gómez-Gonzalo et al., 2010). Recent studies deploying both two-photon and wide-field calcium imaging *in vivo* called into questions these hypotheses, showing that the astrocyte syncytium is indeed recruited into a dramatic 'calcium' wave during ictal events, but that such a wave starts after

seizure onset and unfolds with spatio-temporal dynamics that seem uncoupled from the underlying neuronal activity (Baird-Daniel et al., 2017; Daniel et al., 2015).

Prior to the work described in this thesis, some of which was recently published (Rossi et al., 2017), we had a limited understanding of how the spatio-temporal evolution of interictal and ictal discharges related to the underlying pattern of connectivity in the awake cortex. In Chapter 6 I will describe my wide-field imaging study, which demonstrate that prolonged seizures and brief interictal events both start as standing waves in the V1 focus and in connected locations in higher areas. Following this common beginning, however, seizures persist and propagate both locally and into homotopic distal regions. The prominent oscillations typical of seizures also propagate along homotopic connectivity. Once a seizure generalises, the relationship between patterns of activity and cortical topology becomes more complex: multiple leading regions other than the focus appear to concurrently pace the seizure oscillation and give rise to competing spiral waves and (Huang et al., 2010; Rossi et al., 2017; Viventi et al., 2011) ping pong dynamics (Liou et al., 2017).

Despite these significant advances, recording of spontaneous seizures have proven difficult, and researches have often resorted to study pharmacologically induced seizures. One of the main challenges for the future will be to extend similar research to animal models of spontaneous seizures. Currently, most imaging methods require head fixation of experimental animals: such recordings cannot be prolonged beyond few hours for the sake of animal welfare. Moreover, imaging usually generates terabytes of data that are hard to analyse and store. Hopefully, the development of head-mounted imaging systems (Barretto et al., 2009), combined with the constant improvements in data compression methods and machines computational power (Pachitariu et al., 2016) will soon help researchers in this endeavour, and allow for continuous in-cage imaging of brain activity in freely moving genetic models of epilepsy.

5.4 Open questions to design new therapeutic strategies

Recent technological advances and imaging methods are providing a detailed description of the underpinnings of epileptic networks at multiple scales, from neuronal microcircuits to brain wide networks. I end this chapter outlining some major open questions, and describing how the imaging methods described herein could tackle them and inform the design of novel therapeutic approaches.

An ongoing debate regards the spatio-temporal dynamics of neuronal firing in the ictogenic network (Szabo et al., 2015). Decades of electrophysiological studies established the classical view of epileptic seizures as hypersynchronous and stereotyped events (McCormick and Contreras, 2001). Synchronicity implies coherent firing in the local population, while stereotypy refers to fixed temporal firing patterns that are repeated across epileptic events. While many recordings from humans and animals confirmed highly coherent firing at the focus and decreased coherence in the regions surrounding the focus (Schevon et al., 2012), recent analysis of human recordings reported unexpected contrasting results, showing either low coherence but high reproducibility of neuronal spiking patterns (Truccolo et al., 2011) or completely variable recruitment patterns of the same neurons (Bower et al., 2012).

A related question concerns the difference between seizures, and the numerous, brief interictal discharges that occur between them. It is not known if ictal and interictal events originate in similar populations, and if the two types of event differ from the very beginning in terms of neuronal recruitment and temporal evolution (De Curtis and Avanzini, 2001; Prince and Wilder, 1967). Understanding these factors would help clarify why one type of event propagates and the other does not (Huberfeld et al., 2011).

Two-photon imaging can provide a unifying description of population dynamics during interictal and ictal events, and highlight the differences between activity in the focus and propagation zone. Current unanswered questions and controversies could be due to the technical pitfalls of

electrophysiological recordings, which allow only sparse sampling of the local neuronal population (Wenzel et al., 2017). Two-photon imaging can overcome these limitations, and can be used to ascertain the principles governing population activity in animal models of epilepsy. These principles, in turn, will guide the interpretation of electrophysiological recordings from human subjects: such interpretation is paramount for the correct localisation of the ictogenic focus, particularly when brain surgery is the only option available to patients with pharmacoresistant focal epilepsy (Schevon et al., 2012).

Another important set of questions relates to the role of different excitatory or inhibitory neuronal classes, and the conserved circuit motifs connecting them, in generating, propagating and modulating seizure activity(Paz and Huguenard, 2015). A longstanding simplistic view states that seizures arise from an imbalance between excitation and inhibition in cortical circuits(Prince and Wilder, 1967). In fact, only particular neuronal classes, and their specific connectivity, appear to be placed in critical circuit junctures required for the full expression of seizures (Paz and Huguenard, 2015). Intensely studied examples include feedforward inhibition by parvalbumin positive basket cells, which seems to restrain the propagation of cortical focal seizures (Sessolo et al., 2015), and cortico-thalamo-cortical loops involving cortical CT neurons, which cause the run-away excitation that triggers spike wave discharges in absence epilepsies (Sorokin et al., 2016).

The combination of two-photon imaging and intersectional genetic strategies can clarify which neuronal classes, and what circuits, are casually involved in the progression of ictogenesis; such investigations will pave the way for pre-clinical studies attempting to target these 'choke points' with gene therapy, optogenetic and chemogenetic strategies (Krook-Magnuson and Soltesz, 2015; Paz and Huguenard, 2015). Several recent studies have combined these technologies with real-time seizure detection to achieve closed-loop control of seizures on demand. For instance, inhibition of principal cells with targeted overexpression of K channels or inhibitory opsins (Wykes et al., 2012), and DREADDs (Kätzel et al., 2014) attenuated the seizure phenotype; alternatively, activation of interneurons with excitatory opsins was used to suppress seizures (Krook-Magnuson et al.,

2013). While these results are exciting, a deeper understanding of the timely causal role of these manipulations is needed to avoid undesired pro-epileptic side effects. Indeed, a recent study suggested that while activation of parvalbumin-positive interneurons can suppress seizure propagation, their untimely stimulation might in fact favour the generation of epileptiform discharges (Sessolo et al., 2015). Two-photon *in vivo* imaging techniques will allow to identify which classes of excitatory and inhibitory neurons are important and fire before, during or at the end of a seizure, and eventually help devising an informed optogenetic strategy based on these observations.

A final set of questions asks how the unfolding of epileptic events depends on the topology of brain wide functional connectivity. In the classical view, seizures spread mimic a brushfire, progressively recruiting contiguous circuitry as in the "Jacksonian march" seen in motor cortex. However, somewhat in contrast with this classical view, seizures spread also to distal regions, involving both hemispheres and subcortical centres, and ultimately causing loss of consciousness. The principles that underlie propagation through such a distributed 'epileptic network' are unknown: it is unclear whether pathological connectivity is required or whether seizures spread along the same functional pathways that support information processing during normal cortical activity. Moreover, once the seizure generalises it is unclear how different areas interact to maintain the seizure, and if pacemaker areas important for seizure maintenance or termination exist. Answering these questions can explain why surgery might not work in some cases, and, perhaps most crucially, how to optimise current and future evaluation methods to predict an optimal surgical strategy (Goodfellow et al., 2016).

Widefield calcium imaging can answer these questions, and help devise a predictive modelling framework to quantify the contribution of different network component to ictogenesis, which will improve the outcome of treatment (Goodfellow et al., 2016). The map of the structural and functional connectivity between brain areas can be used as a reference to understand the dynamic interactions of the epileptic focus with other functionally connected regions

(Rossi et al., 2017). Multiplexed recordings from excitatory and inhibitory neuronal populations will allow to understand and compare pathways for normal processing and epilepsy, and dissect how the breakdown of inhibition promotes seizure propagation (Schevon et al., 2012; Trevelyan et al., 2007). Finally, imaging during generalised seizure, and comparison of differences and commonalities between various pharmacological and genetic models, can be used identify nodes outside the focus important for seizure generation, maintenance and termination (Liou et al., 2017). For example, it has been proposed that seizures, analogously to arrhythmias in the cardiac tissue excitation, could be terminated by the mutual annihilation of spiral waves and planar waves originating from different seizing regions: this would have implications for electrical stimulation or optogenetic strategies to disrupt seizures (Viventi et al., 2011). Lastly, wide field imaging can also reveal the causal interaction between seizures and other circuit dysfunction such as cortical spreading depression (Farkas et al., 2008), which underlie post-ictal migraine (Charles and Baca, 2013) and sudden unexpected death in epilepsy (Aiba and Noebels, 2015).

Chapter 6

Methods

6.1 Part 2

Herein I detail the methods used in the experiments described in Chapter 7. All data analysis was performed in MATLAB (The MathWorks Inc.).

6.1.1 Transgenic lines

Experiments were performed on 8-12 week old female and male mice that were maintained on a 12 hours light/dark cycle. Emx1::Cre; CAG::flex-GCaMP3 mice were generated by crossing the following two transgenic lines: Emx1-IRES-Cre, expressing Cre recombinase under the Emx1 promoter (catalog #005628, The Jackson Laboratory); and a reporter *Ai38-GCaMP3* line (catalog #014538, The Jackson Laboratory), carrying a floxed copy of the *GCaMP3* gene under the strong *CAG* promoter in the *Rosa26* locus. Offspring expressed GCaMP3 in excitatory neurons of the neocortex and hippocampus (Gorski et al., 2002; Vanni and Murphy, 2014).

Rasgrf-dCre-CaMKIIa-TTA-TITL-GCaMP6f triple transgenics(Madisen et al., 2015) were generated by breeding *Rasgrf-dCre, CamKII-tta* and *Ai93(TITL-GCaMP6f)* mice. Three weeks before imaging, TMP was orally administered for 3 consecutive days to trigger dCre-mediated recombination. With this system, *flex-GCaMP6f* recombination was induced only in *Rasgrf* positive neurons, while transcription was further restricted to *CaMKIIa* expressing neurons that also expressed the transcription factor TTA. As a result, GCaMP6 expression was selective to pyramidal neurons located in layers 2/3 and sparsely in layer 5.

Although GCaMP6f allows for the detection of population activity with higher signal to noise ratio than GCaMP3, the cortical activations studied here were so massive that this made little difference. We thus present data obtained with both indicators.

6.1.2 Surgical procedures

Using aseptic techniques, animals were chronically implanted with a thinned skull cranial window under isoflurane anesthesia. 0.05mL Rimadyl (Carprofen 5% w/v) was administered before surgery as an anti-inflammatory and analgesic. During the procedure, eyes were protected with ophthalmic gel (Viscotears Liquid Gel, Alcan) and the body temperature maintained around 37˚C. The animal was anesthetized and mounted in a stereotaxic frame. The scalp over the dorsal skull surface was removed to expose the cranium. The left hemisphere parietal bone was thinned using a scalpel blade. Thinning proceeded until the cancellous layer of the skull, which contains blood vessels, was completely removed. A custom-made stainless steel head plate with a round imaging chamber (8 mm diameter) was then cemented over the thinned area using dental cement (Superbond). Finally, a small drop of UV cement (Norland Products Inc.) was applied inside the imaging chamber and an 8 mm glass coverslip glued onto the thinned skull region. The cement was cured with an UV LED (390nm, Thorlabs) for 20 s. The animal was allowed to recover at 37˚C in an incubator and provided with Rimadyl in the drinking water (0.1 mL in 100 mL) for the three days after the surgery.

On the day of LFP recordings, the animal was anaesthetized again and a small skull screw implanted in the contralateral frontal bone, rostral to the cranial window. A silver wire previously soldered to the screw head served as a reference for electrophysiological recordings. After opening a small hole in the cranial window coverslip, a small craniotomy was performed over the target region of V1. The exposed region was finally covered with Kwik-Cast silicone elastomer sealant. The animal was allowed to fully recover before starting the recording session. The typical recording session of epileptiform activity lasted 30-40 minutes.

6.1.3 Visual stimulation and retinotopic mapping

Visual stimuli were presented on three LCD monitors(Carandini et al., 2015), positioned 30 cm from the animal, arranged to span 140 degrees in azimuth and

60 degrees in elevation of the visual field contralateral to the imaged hemisphere. For retinotopic mapping, stimuli were contrast-reversing gratings presented inside a rectangular window. Stimulus duration was 5 s, flickering frequency was 2 Hz, and spatial frequency was 0.03 cycles/°. To measure the preferred azimuth, the rectangular window was 60° high and 30° wide. To measure the preferred elevation, it was 20° high and 140° wide. Eye movements were monitored with CCD camera equipped with 2 infrared LEDs.

6.1.4 Electrophysiology

Local field potential (LFP) was recorded with Ag-Cl electrodes in ACSF-filled borosilicate micropipettes (typical tip aperture 2-3 μm, 1-3 MΩ), positioned at 500-600μm below the dura. To induce epileptiform activity, 10 mM Picrotoxin (Sigma) dissolved in DMSO (Sigma) was added to the recording solution. During these experiments, the pipette was pushed through the dura without applying pressure, to avoid injection of the GABAergic antagonist. In some experiments, we induced epileptiform activity with injections of 100-200nL of 5M pilocarpine dissolved in DMSO. Because of the viscosity of the solution, the injection pipette was then withdrawn and exchanged with an ACSF-filled borosilicate micropipette to record the LFP. The pressure inside injection pipettes was measured with a differential manometer and kept below 200 mbar. The resistance of the micropipette was monitored to ensure that insertion in the brain did not clog the tip. LFP signals were amplified 1,000 fold and high-passed above 0.1 Hz via a Multiclamp 700B differential amplifier (Molecular Devices). Data were digitized at 10 kHz with a Blackrock acquisition system and software. The exposure signal from the camera, the TTL signals from the visual stimulation software and the screen photodiode signal were recorded at the same time to synchronize electrophysiological, imaging and visual stimulation data.

6.1.5 LFP analysis

To identify the start times of interictal events and seizures from the LFP recording we devised a simple supervised event detection method. The LFP trace was resampled at 100 Hz; the start of each event was assigned to the local maxima

of the first derivative of the signal that exceeded 3 standard deviations from baseline; the end of each event was identified when its low frequency envelope returned to baseline. Finally, the results of the automatic detection were inspected visually and events classified as interictal events or seizures. Missed events were manually selected and artifacts removed.

Wavelet scalograms of the LFP signal were computed using the wavelet toolbox provided by Torrence and Compo (atoc.colorado.edu/research/wavelets). Power spectra and coherence of LFP and fluorescence signals were calculated using the Chronux Toolbox(Mitra and Bokil, 2008) (http://chronux.org/).

6.1.6 Widefield calcium imaging

Imaging experiments were performed under a custom built tandem-lens epifluorescence macroscope (Carandini et al., 2015; Ratzlaff and Grinvald, 1991). Excitation light at 480nm was provided by a blue LED light (465nm LEX2-B, Brain Vision, band-passed with a Semrock FF01-482/35 filter) and diverted via a dichroic mirror (FF506-Di03, Semrock) into a Leica 1.0X Plan APO (M series, part #10450028) or 1.6X Plan APO objective (M series, part #10450029), which focused the light on the sample. The collected fluorescence was reflected by a second dichroic mirror (FF593-Di03, Semrock), passed through an emission filter (FF01-543/50-25, Semrock), and focused by a second Leica 1.0X Plan APO objective onto the sensor of a sCMOS camera (pco.edge, PCO AG). The camera was controlled by a TTL external trigger synchronized with the visual stimulation. The image acquisition rate was 50 Hz for retinotopic mapping and 70 Hz during imaging of epileptiform activity (except for experiments in the pilocarpine model, imaged at 50 Hz). The nominal spatial resolution of the system was 200 pixel/mm. Imaging was conducted in 20 s long sweeps, interleaved with ~10 s pauses needed to save the data to disk.

6.1.7 Analysis of imaging movies

Widefield movies where first registered using a discrete Fourier transform based subpixel image registration algorithm(Guizar-Sicairos et al., 2008). The

retinotopic mapping and epileptiform activity images where then aligned using the brain vasculature as a reference. Affine transformation was used to find the best alignment. Then we calculated $\Delta F/F_0$ movies, where the signal for each pixel x at time t was obtained as

$$\frac{\Delta F(t,x)}{F_0(x)} = \frac{F(t,x) - F_0(x)}{F_0(x)}$$

F_0 was computed as the 20th percentile of each imaging sweep. Finally, a mask was manually drawn to segment out the visible cortex form the edges of the implant.

The map of retinotopy was obtained as previously described(Carandini et al., 2015) In short, the reversing gratings elicited periodic neural responses that oscillate at twice the frequency of reversal(Benucci et al., 2007). For each pixel, we measured the power of these second harmonic responses using the Fourier transform of the fluorescent trace. We then fitted a Gaussian position-tuning curve to the amplitude of the responses to visual stimulation at four horizontal positions. The standard deviation for the Gaussian curve model was the one that minimized the least squared error of the fit across pixels.

To localize the cortical initiation site of each event, calcium signals were aligned by the start of the electrographic discharge. For each event, pixels were included if they showed $\Delta F/F$ increases greater than 60% of the peak $\Delta F/F$ reached in the same class of events. The center of mass of the resulting cortical area, calculated over the first 500 ms, was then taken as the site of initiation of epileptiform activity. The average retinotopic position of the focus across animals was 93±16 degrees, confirming our ability to target the medial region of V1. We restricted the analysis to events that were contained for the most part in an imaging sweep. In particular, we included seizures that were imaged for at least 6 s after their start.

To assess the slow propagation of seizures, we defined criteria to evaluate when a cortical territory was invaded by the seizing activity. The distribution of maximum florescence levels during seizure was bimodal (Suppl. Figure 5). We

considered recruited to the seizure the pixels that exceeded 30% of the peak fluorescence recorded at the focus, which was a good threshold to separate the population of pixels with the highest fluorescence change (Suppl. Figure 5). We then calculated the time it took for a seizure to invade each recruited pixel, measured from the electrographic seizure onset. We called this time 'delay to seizure invasion', and we measured it as the time point at which the fluorescence at any recruited pixel reached 60% of its maximum.

6.1.8 Standing wave model

We modeled the fluorescence movies of epileptiform events as standing waves (Figure 3**e**), i.e. as the product of a global time course and a single map (an image)

$$Movie = Timecourse * Map + Residuals$$

To fit this model (i.e. to minimize the residuals), we used singular value decomposition (SVD), which returns the best least square approximation of a matrix as the sum of standing waves. We obtained the time course and map of the separable model from the first row and first column returned by the SVD.

6.1.9 Modelling of the profile of interictal events

We modeled the retinotopic profile of activation elicited by interictal events as the dot product of two functions, both dependent on the cortical position **x** of each ROI.

The first function depends on homotopic connectivity, and is a Gaussian falling off with the distance between the retinotopic position $R(\boldsymbol{x})$ of point $\boldsymbol{x}$ and the retinotopic position of the focus, $\boldsymbol{R_{focus}}$:

$$H(\boldsymbol{x}) = e^{\frac{-\left(R(\boldsymbol{x}) - \boldsymbol{R_{focus}}\right)^2}{2\sigma^2}}$$

The second function depends on contiguous spread, and is a Gaussian-like function with the numerator raised to the 4th power to give it a flat top as it falls off with the cortical distance from the epileptic focus:

$$C(\boldsymbol{x}) = (a - b)e^{\frac{-\left(\boldsymbol{x} - \boldsymbol{x_{focus}}\right)^4}{\lambda^4/ln(2)}} + b$$

When so parametrized, λ corresponds to the half-width half-maximum of the function. We fitted the parameters σ, λ, $\boldsymbol{R_{focus}}$, $\boldsymbol{x_{focus}}$, a, b by least square minimization.

6.1.10 Phase analysis of cortical oscillations

Movies of cortical seizures were first bandpass-filtered between 6 and 11 Hz. Then we computed the analytical representation of the fluorescence timecourse for each pixel, using the Hilbert transform (MATLAB function 'hilbert', Signal Processing Toolbox). The analytical signal $S_a(t)$ is a representation of a real valued signal $f(t)$ in the complex space:

$$S_a(t) = f(t) + iH(f)(t) = A(t)e^{i\varphi(t)}$$

Its real part is $f(t)$, the fluorescence signal, while its imaginary part is $H(f)(t)$, the Hilbert transform of $f(t)$. When expressed in polar form, the analytical signal $S_a(t)$ has a straightforward interpretation: the modulus $A(t)$ represents the instantaneous amplitude, or envelope, of the oscillation; the angle $\varphi(t)$ represents the instantaneous phase of the oscillation.

6.1.11 Behavioral data

The eye contralateral to the imaged cortex was imaged with a monochrome CCD camera (DMK 21BU04.H, The Imaging Source), equipped with a macro zoom lens (MVL7000 - 18 - 108 mm EFL, f/2.5, Thorlabs). Illumination to the eye was provided by 2 infrared LEDs (850nm, Mightex, powered by an SLC-SA/AA LED controller, Mightex). An infrared filter (700nm high-pass, #092, The Imaging Source) was applied to the camera objective to shield it from stray light. Eye imaging movies were processed with custom software to extract eye movements, pupil dilations and blinks.

The running behavior was measured using a rotary encoder (Kübler 05.2400.1122.0100) that tracked the revolutions of the cylindrical treadmill. The angular displacement was first converted into angular speed and then into linear speed based on the diameter of the treadmill.

Both the rotary encoder signal and the fame time stamps from the eye-tracking camera were acquired using a data acquisition board (National Instruments, PCIe-6323). The same board acquired a copy of the exposure signal from the imaging camera, the TTL signals from the visual stimulation software and the screen photodiode signal: such signals were used to align imaging, electrophysiological and behavioral recordings.

6.1.12 Statistical information

Data were tested for normality before choosing the appropriate statistical test. All the statistical tests used were 2-tailed test. The significance of linear regression models was tested with the F-statistic against the null hypothesis of a constant model. $p = 0.05$ was assumed as the threshold for statistical significance.

6.1.13 Data and code availability

All the relevant data and code are available from the authors upon request. Representative code and an example dataset can be found at www.ucl.ac.uk/cortexlab/data.

Chapter 7

Focal cortical seizures start as standing waves and propagate respecting homotopic connectivity

7.1 Introduction

Focal cortical epilepsy, also known as partial-onset epilepsy, frequently resists pharmacological treatment. Its origins are thought to be unambiguously cortical: seizures arise from congenital or acquired cortical lesions such as focal cortical dysplasia, penetrating brain injuries, abscesses, strokes, and tumors (Wiebe and Jette, 2012). Much of its morbidity results from the spread of seizure activity from a cortical focus to further cortical regions. These regions can be local and contiguous to the focus, as in the "Jacksonian march" seen in motor cortex. However, they can also be distal and ultimately involve both hemispheres and subcortical centres ("secondary generalization"), causing loss of consciousness(Motelow et al., 2015).

It is not known whether seizures spread along the same circuits that support information processing during normal cortical activity(Schwartz and Bonhoeffer, 2001). These circuits may not act as effective constraints during seizures. First, the circuits that underlie normal function rely on synaptic transmission, whereas seizures may involve non-synaptic mechanisms(Bedner et al., 2015; Carmignoto and Haydon, 2012; Gyengesi et al., 2003; Huberfeld et al., 2007; Qiu et al., 2015; Staley et al., 1995; Voipio and Kaila, 2000; Zhang et al., 2014). Second, the flow of activity along the circuits that underlie normal function depends on the balance of synaptic excitation and inhibition. Because seizures disrupt this balance(Goodkin, 2005; Muldoon et al., 2015; Schevon et al., 2012; Trevelyan et al., 2007; Ziburkus et al., 2006), their propagation may obey different rules.

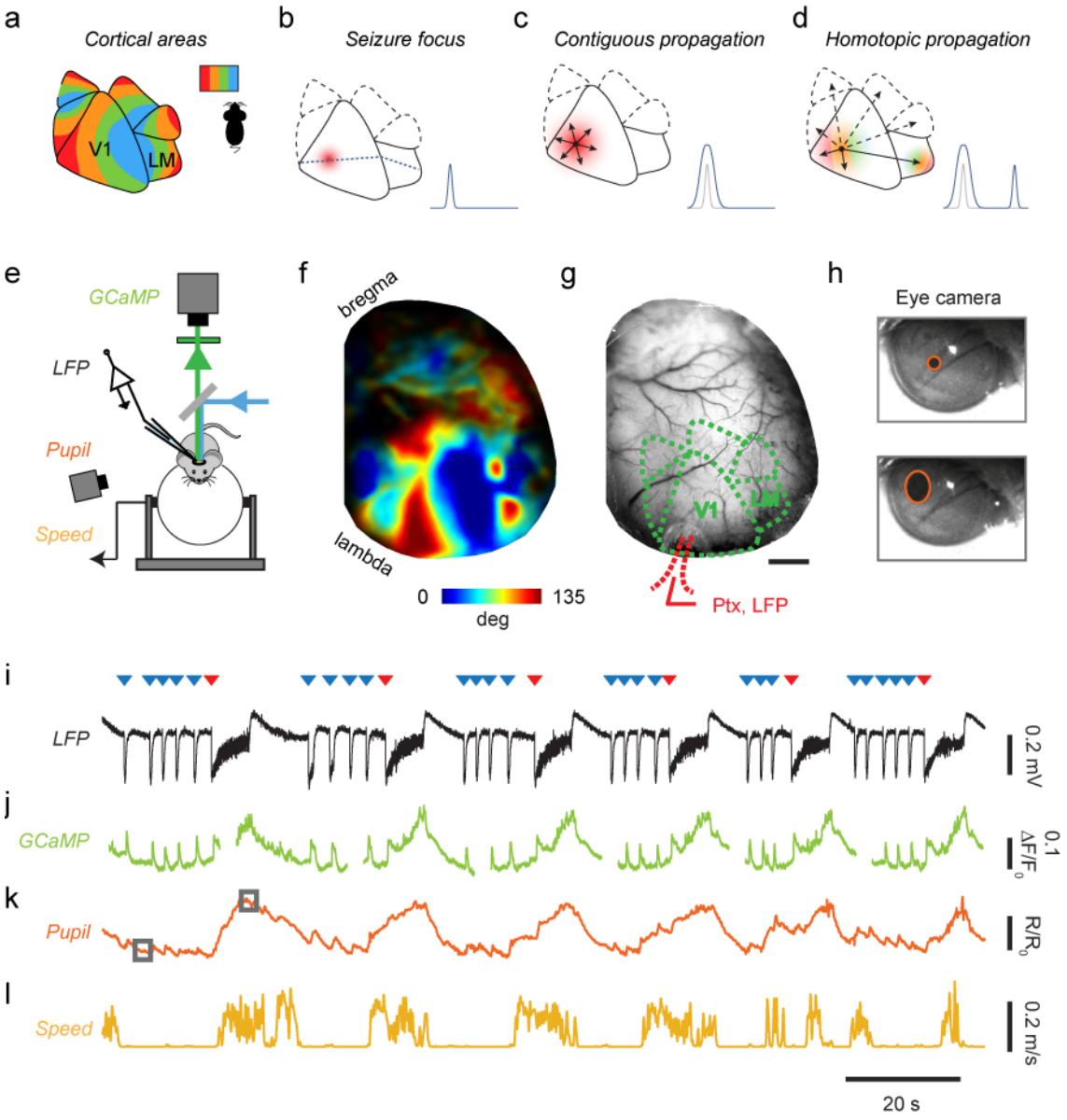

Figure 7.1: Testing hypotheses for cortical seizure propagation with simultaneous imaging, recordings and behavioral measurements in the awake mouse. (**a**) Cartoon of mouse visual cortex showing six visual areas in the right hemisphere, each containing a map of the left visual field (inset). Colors indicate territories that prefer the same horizontal position. V1 and LM are the primary and secondary visual areas. (**b**) Cartoon depicting elevated activity in the seizure focus in V1. Dotted line through the epileptic focus connects V1 and LM regions that prefer the same vertical position. Inset: Profile of activity along that line. (**c**) Contiguous propagation hypothesis: local mechanisms make seizure spread radially to nearby territories. Inset: profile of idealized activity at onset (gray) and during spread (blue). (**d**) Homotopic propagation hypothesis: long-range connections generate secondary distal foci in homotopic locations in higher visual areas. Inset as in **c**. (**e**) Schematic of the experimental setup. (**f**) Example retinotopic map obtained from a GCaMP6f mouse. Colors indicate preferred horizontal position (color bar). (**g**) Representative image acquired during simultaneous widefield imaging and LFP recordings. Red dots highlight location in V1 of pipette for injection of Picrotoxin (Ptx)

and recordings of local field potential (LFP). Scale bar indicates 1 mm. (**h**) Example frames from the eye camera taken when the pupil was constricted (top) or dilated (bottom), with fitted ellipses (red). (**i**) LFP traces measured during epileptiform activity, showing seizures (red triangles) and interictal events (blue triangles). (**j**) Simultaneous GCaMP fluorescence, averaged over the entire imaging window (discontinuities indicate pauses in image acquisition). (**k**-**l**) Behavioral measures during epileptiform discharges: pupil dilations (**k**) and running speed (**l**).

A related question concerns the difference between seizures (ictal events), and the numerous, brief interictal events that characteristically occur between seizures. Seizures represent excessive neuronal firing lasting seconds or minutes and spreading locally and distally(Schevon et al., 2012; Smith et al., 2016). Interictal events, instead, are brief and localized(De Curtis and Avanzini, 2001). A longstanding theory is that their duration and spread are limited by a powerful inhibitory surround(Prince and Wilder, 1967). It is not known, however, if seizures and interictal events originate in similar neuronal populations, and if their initiation differs in terms of spatial profile and temporal evolution(Huberfeld et al., 2011). More generally, it is not clear why seizures persist and propagate, while interictal events subside and stay local.

We addressed these questions in the visual cortex of the mouse, where we could readily distinguish between two scenarios of seizure propagation (**Figure 7.1a-d**). Mouse visual cortex includes multiple retinotopic areas(Andermann et al., 2011; Wang and Burkhalter, 2007), the largest of which are the primary and latero-medial areas (V1 and LM, **Figure 7.1a**). Epileptiform activity in a focal region of V1 (**Figure 7.1b**) could then spread in at least two ways: contiguously or homotopically. In the first scenario, epileptiform activity propagates through local mechanisms to V1 regions that are contiguous to the focus (**Figure 7.1c**). In the second scenario, epileptiform activity propagates along long-range projections from V1 to homotopic regions of higher visual areas, i.e. regions that have the same retinotopic preference(Glickfeld et al., 2013; Wang and Burkhalter, 2007), producing one or more distinct, secondary foci (**Figure 7.1d**).

To evaluate these models of seizure propagation, we induced epileptiform activity in a focal region of V1 and used widefield imaging of genetically-

encoded calcium indicators(Carandini et al., 2015; Vanni and Murphy, 2014; Rossi et al. 2013) to characterize the propagation of activity in space and time. We found that prolonged seizures and brief interictal events both start as standing waves in the V1 focus and in homotopic locations in higher areas. Following this common beginning, however, seizures persist and propagate both locally and into homotopic distal regions. Seizures, moreover, contain prominent oscillations, which also propagate along homotopic connectivity. We conclude that seizure initiation resembles the initiation of interictal events, and seizure propagation respects the connectivity underlying normal visual processing.

7.2 Results

We generated transgenic mice expressing a genetically-encoded calcium indicator (GCaMP3 or GCaMP6f) in excitatory neurons of the cortex(Gorski et al., 2002; Madisen et al., 2015; Zariwala et al., 2012), and implanted a head-post and a glass cranial window spanning the left parietal bone, which we thinned to facilitate optical access(Carandini et al., 2015). After recovery and a period of habituation, we drilled a small opening in the window for insertion of a micropipette, and head-fixed the mice over a treadmill where they were free to run while we performed visual stimulation, widefield imaging, and electrophysiological recordings (**Figure 7.1e**).

7.2.1 Measuring connectivity and epileptiform activity

We first used widefield imaging of GCaMP fluorescence to measure activity evoked by visual stimulation, and mapped the retinotopic organization of V1 and higher visual areas (**Figure 7.1f**). For each mouse we aligned the salient features of the retinotopic map (Carandini et al., 2015) on a reference map of the areal organization of the mouse visual cortex (Andermann et al., 2011). This procedure identified multiple visual areas (**Figure 7.1f**) including V1 and adjacent area LM, which is thought(Polack and Contreras, 2012) to be homologous to primate area V2. The retinotopic map gauges the connectivity between V1 and higher visual areas: regions that respond to the same retinotopic location are also interconnected (Glickfeld et al., 2013; Wang and Burkhalter, 2007).

We then elicited focal epileptiform discharges by blocking $GABA_A$ receptors in a small region of V1 (**Figure 7.1g**). Local application of $GABA_A$ receptor antagonists (Steriade and Contreras, 1998) and blockers (Viventi et al., 2011) is well-known to cause focal epileptiform events. We delivered a blocker, picrotoxin (10 mM) in a pipette inserted into medial V1 via a small craniotomy, and we applied no pressure, to minimize diffusion beyond the tip of the pipette (resistance 0.5-3 MΩ). We targeted layer 5 because its extensive recurrent, horizontal and columnar connectivity enable it to evoke prolonged depolarization across layers (Beltramo et al., 2013), making it a promising location for triggering translaminar epileptiform events.

Within minutes of pipette insertion, recordings of local field potential (LFP) made from the same pipette revealed robust epileptiform events (**Figure 7.1i-n**). These events consisted of intermittent seizures (**Figure 7.1i**, *red triangles*) separated by sequences of brief discharges (**Figure 7.1i**, *blue triangles*). These epileptiform events were mirrored by large amplitude GCaMP optical signals (**Figure 7.1l**). They were also typically accompanied by pronounced increases in pupil dilation (**Figure 7.1h**,**m**) and by bouts of running (**Figure 7.1n**).

7.2.2 Signatures of seizures and interictal events

Based on their duration, these epileptiform events could be readily categorized into distinct classes: seizures and interictal events (**Figure 7.2**). Their duration was distributed bimodally, with a median duration of 8.6 s for seizures, and 0.5 s for interictal events (**Figure 7.2a**, $p < 0.001$, Wilcoxon rank sum test, n=5 mice). Interictal events occurred on average 13.4 ± 3.7 times per minute (n = 5 recordings in 5 animals), much more frequently than seizures, which occurred about once per minute (1.0 ± 0.2 events min^{-1}). Interictal events were slightly larger on average (**Figure 7.2b**, $p < 0.001$, Wilcoxon rank sum test, n = 5 mice) and were followed by briefer periods of relative LFP quiescence than seizures (**Figure 7.2c**).

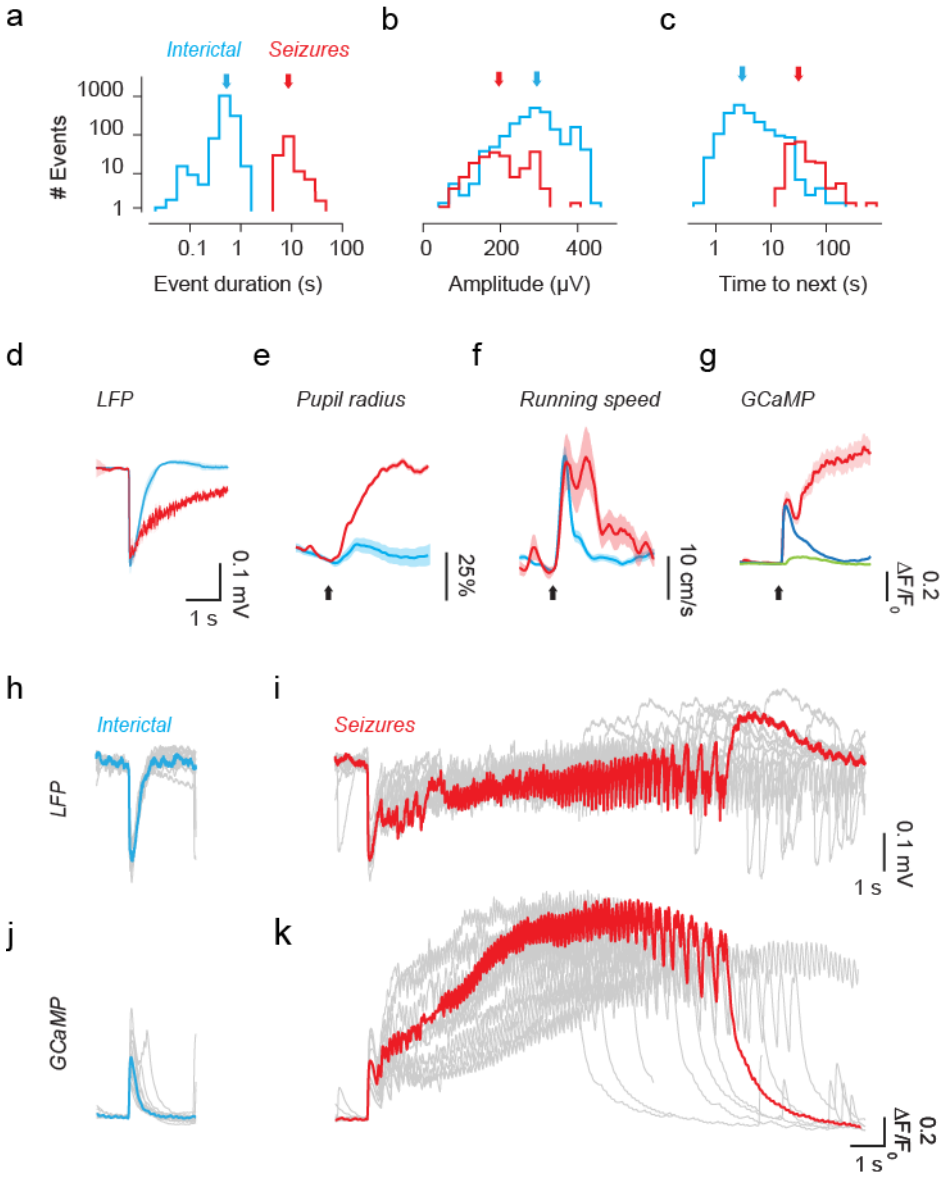

Figure 7.2: Neural and behavioral signatures of seizures and interictal events. (a) Distribution of the duration of interictal events (blue) and seizures (red). Arrows indicate the medians of each distribution. (b) Distribution of event amplitudes, measured as the peak of the initial LFP negative event. (c) Distribution of inter-event intervals (time to next event). (d) LFP waveform following the onset of interictal events (blue) and seizures (red), averaged across all events and in 5 mice. (e) Change in pupil radius triggered on the onset of interictal events (blue) and seizures (red), for one representative animal. Arrow indicates event onset. (f) Same, for running speed. (g) Time courses of GCaMP6f activity in the same animal, averaged over area V1, during interictal events (blue) and seizures (red). Green trace shows response to flickering gratings for comparison. (h) LFP waveform of representative interictal events in one experiment. Blue trace highlights a single representative event. (i) Same as h, for seizures in the same experiment, with the representative trace in red. (j) GCaMP6f activity averaged over visual cortex during the example interictal events in h. (k) Same as j, for the seizures shown in i.

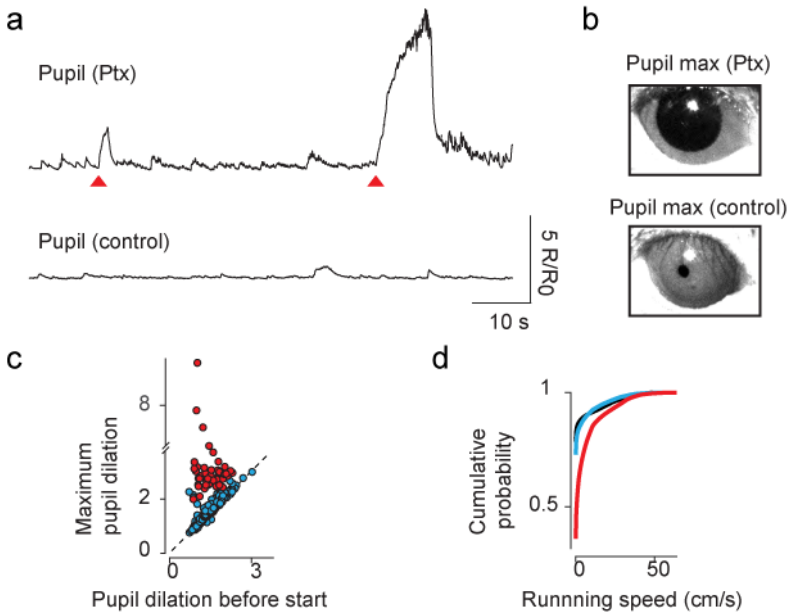

Figure 7.3 Behavioural correlates of epileptiform events. (**a**) Top panel: Example pupil dilation recording during Ptx-triggered seizures in the visual cortex. Red triangles indicate seizure initiation. Bottom panel: Example recording of pupil radius in control physiological conditions, during the presentation of visual stimuli used for retinotopic mapping. (**b**) Comparison between maximum pupil dilations measured in control physiological conditions (bottom panel) versus maximum pupil dilation recorded during Ptx-triggered seizures (top panel), for the same example mice of panel **a**. Difference between maximum dilations in these two conditions was significant across mice ($p < 0.05$, two samples t-test, n=3). (**c**) Relationship between pupil dilation at the start (abscissa) and at maximum reached during epileptic events (ordinate) of the two types (**446** interictal events and **53** seizures from 3 animals). Dilations are measured relative to baseline pupil radius (R_0). (**b**) Cumulative distribution of running speed in a 2s window following the onset of interictal events (blue) and during seizures (orange), compared to baseline measurements obtained between events (black). Data normalized and averaged across **5** animals.

Seizures had pronounced behavioural correlates: they were typically accompanied by prolonged pupil dilations (**Figure 2e**, **Figure 7.3a**) and by bouts of running (**Figure 7.2f**, **Figure 7.3b,** Kolmogorov-Smirnov test, $p < 0.01$, $n = 5$ mice). In addition, the longer seizures culminated in abnormal behaviors such as tail flicking and clonic movements of the forelimbs. For interictal events, pupil dilations were typically smaller (**Figure 7.2e**), running bouts briefer (**Figure 7.2f**) and not consistent across mice (Supplementary Figure **1b**).

Interictal events and seizures also had distinct spectral features (**Figure 7.2h**,**i**, **Figure 7.5**). The LFP waveform of interictal events was highly stereotypical: a

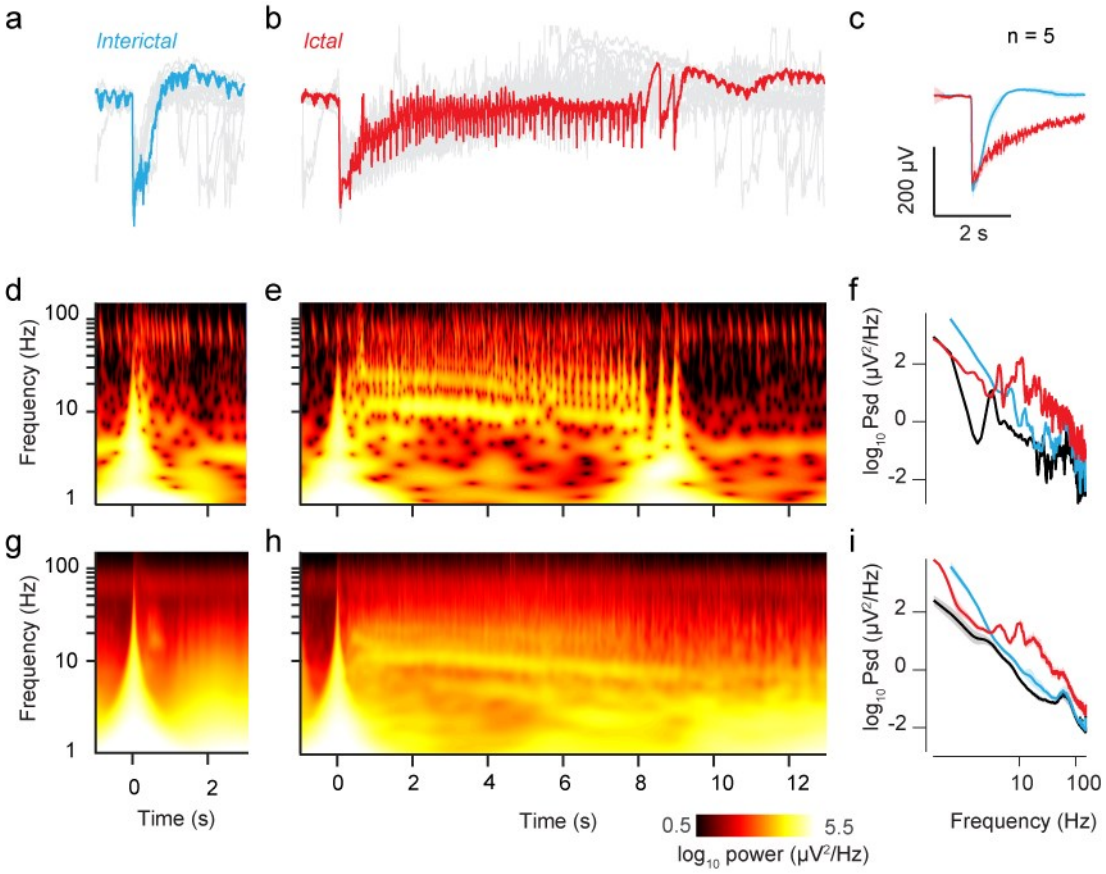

Figure 7.5 Temporal and spectral signatures of interictal events and seizures measured from the LFP. (**a**) LFP waveform of a representative interictal event (blue) and of other example events recorded during the same experiment (grey). (**b**) Same as **a**, for seizures in the same experiment. (**c**) Average across animals (n = 5) of the LFP waveform following the onset of interictal events (blue) and seizures (orange). (**d-e**) Spectrograms (Morlet-wavelet scalograms) of the representative traces in **a** and **b**. (**f**) Power spectra of those two events measured over 3 s from onset, and compared to a representative baseline period (black). (**g-h**) Average spectrogram of interictal events (n = 1476) and seizures (n = 137), across 5 animals. (**i**) Average power spectrum of the events, obtained by averaging curves such as those in **f** across events and animals. The width of the curves indicates 2 s.e.m.

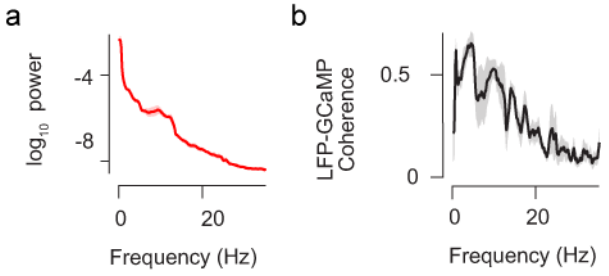

Figure 7.4 Frequency content of GCaMP signals. (**a**) Average power spectrum of the GCaMP signals recorded over the visual cortex during seizures, across animals (n = 5). (**b**) Average coherence between the LFP and the GCaMP signals recorded during seizures across animals (n = 5).

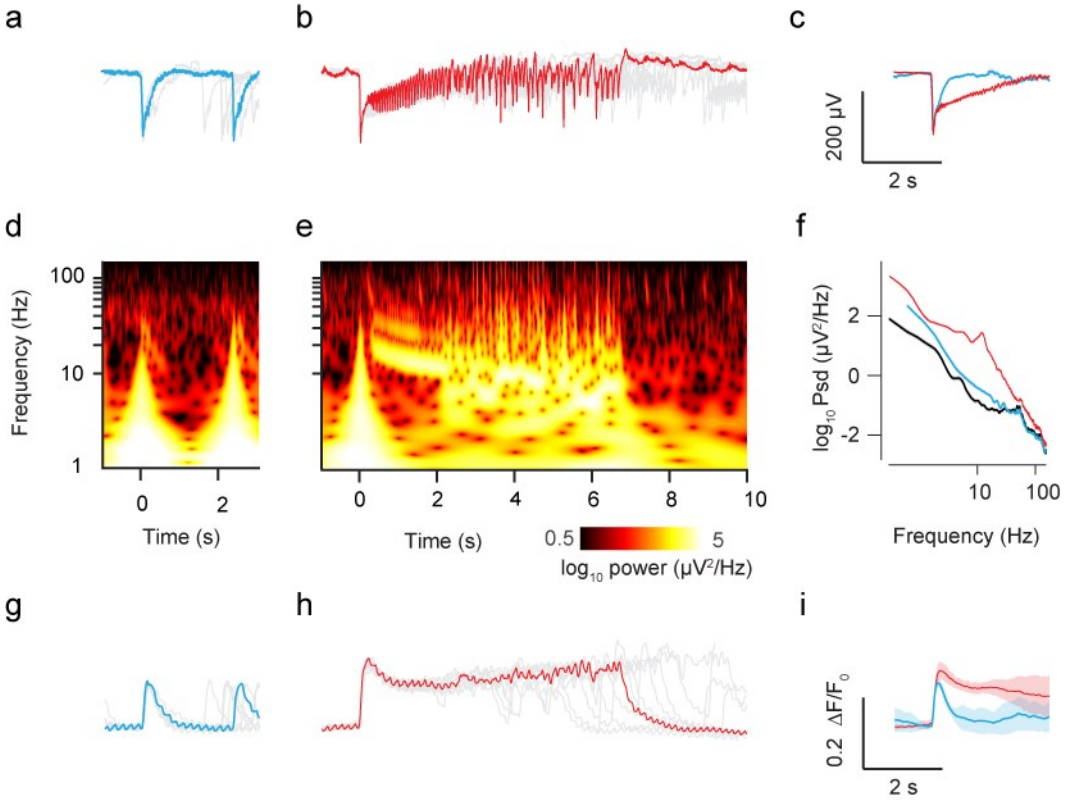

Figure 7.6 Pilocarpine-induced epileptic focus recapitulates results obtained with the picrotoxin model. (**a**) LFP waveform of a representative interictal event (blue) and of other example events recorded during the same experiment (gray). (**b**) Same as **a**, for seizures in the same experiment. (**c**) Average of the LFP waveform from one animal following the onset of interictal events (blue) and seizures (orange). (**d-e**) Spectrograms (Morlet-wavelet scalograms) of the representative traces in **a** and **b**. (**f**) Average power spectrum of interictal events and seizures for one animal, compared to power spectrum of baseline activity. (**g**) GCaMP activity averaged over visual cortex during the example interictal events in **a**. (**h**) Same as **g**, for the seizures shown in **b**.)(**i**) Average of GCaMP fluorescence averaged over the visual cortex from one animal following the onset of interictal events (blue) and seizures (orange) (**j**) Variance explained by the standing wave model for 1 s sections of interictal events (blue dot) and seizures (red dots). Error bars show median ± 1 quartile. Shaded blue area indicates the 96% confidence interval for quality of the fit to interictal events. (**k**) Comparison between maximum signal recorded in picrotoxin (n=3) and pilocarpine (n=2) experiments, including GCaMP3 animals only, during interictal events or seizures (** = p<0.001, * p = <0.05, two samples t-test). (**l**) Comparison between the area of the epileptic focus induced in picrotoxin (n=3) and pilocarpine (n=2) experiments, including GCaMP3 animals only (ns = no significant difference found, two sample t-test)

sharp negative deflection lasting 50-100 ms (**Figure 7.2h**, **a**). Seizures had similar onset (**Figure 7.2i**, **Figure 7.5b**), but this onset was followed by a rapid escalation of high-frequency activity, with a large increase in power between 6 and 30 Hz (**Figure 7.5b**,**e**). The increase in power near 10 Hz was consistent across events

and animals (**Figure 7.5i**). These epileptiform events were faithfully tracked by large fluorescence signals, which dwarfed those seen during normal visual processing (**Figure 7.2g**). The peak fluorescence changes ($\Delta F/F_0$) seen during epileptiform events were 125±22% for interictal events and 175±50% for seizures. These signals were much larger than those evoked by visual stimuli (Carandini et al., 2015; Wekselblatt et al., 2016) (**Figure 7.2g**), which peaked at 4±1%. Yet, they bore close relationship to the LFP (**Figure 7.4**), and faithfully followed the main frequency components of seizures (**Figure 7.2j-k**).

The basic features of these epileptiform events were not peculiar to the acute disinhibition induced by picrotoxin: they were also observed in additional experiments where we elicited focal epileptiform activity with injections of pilocarpine(Kätzel et al., 2014) (5M), an agonist of muscarinic receptors (**Figure 7.6**). In these experiments, epileptiform events started as brief interictal events (**Figure 7.6a**), which became progressively longer to resemble seizures measured with picrotoxin (**Figure 7.6b**). The LFP spectral signatures of these events closely resembled those seen with picrotoxin (**Figure 7.6d-f**). As with picrotoxin, moreover, wide-field changes of fluorescence associated with these events dwarfed the responses measured with visual stimuli. However, the peak fluorescence changes were about half the size of the ones measured with picrotoxin, and the high resistivity of the pilocarpine solution made it impossible to record the LFP via the same pipette used for injection. For these reasons, in the following, we report on results obtained with picrotoxin.

7.2.3 Interictal events and seizures start as standing waves

The fluorescence signals allowed us to study the spatial spread of epileptiform events, and revealed profound differences between ictal and interictal events (**Figure 7.7a-c**). The transient fluorescent signals seen during interictal events were localized in V1 with a smaller peak in LM (**Figure 7.7a**). They involved a region that was markedly smaller than the region that could be activated by visual stimuli (**Figure 7.7b**, Supplementary Movie 1). Seizures, instead, progressively invaded the entire visual cortex and beyond (**Figure 7.7c**,

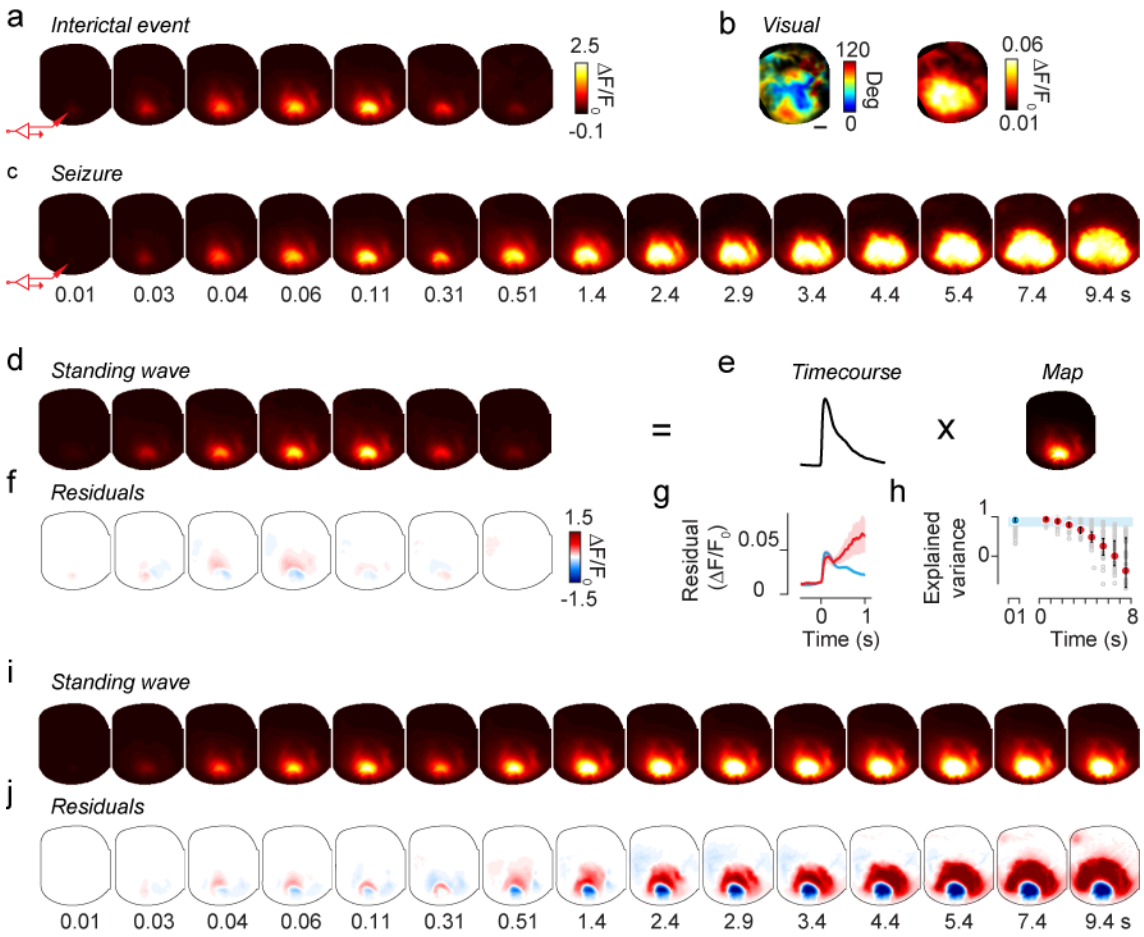

Figure 7.7: Interictal events and seizures start as standing waves, and seizures subsequently propagate widely across cortex. (**a**) Frames obtained through GCaMP6f imaging in a representative interictal event (the one with LFP in Figure 2**h**,**j**). The cartoon electrode indicates the site of Ptx injection and epileptic focus. (**b**) Retinotopic map and map of maximal activation in response to visual stimulation for this animal. Scale bar is 1 mm. (**c**) Same as **a**, for a representative seizure (the one with LFP in Figure 2**i**,**k**). Labels indicate the time of each frame from event onset and apply to frames in **a** and **c**. (**d**) Predictions of a standing wave model fit to interictal event in **a**. (**e**) The standing wave is the product of a single temporal waveform (Timecourse) and a fixed spatial profile (Map). The map and the timecourse shown are averaged across interictal events for this animal. (**f**) The residuals of the fit in **e** are small, indicating little deviation of interictal event from standing wave. (**g**) The root-mean-square residuals for the standing wave model applied to interictal events (blue) and seizures (red). The spatial map was optimized to fit interictal events. Shaded areas indicate two s.e.m. (**h**) Variance explained by the standing wave model for interictal events (blue dot) and 1 s intervals of seizures (red dots). Error bars show median ± 1 quartile. Shaded blue area indicates the 96% confidence interval for quality of the fit to interictal events. (**i**) Predictions of the standing wave model for the seizure in **c**. The model was imposed to have the average spatial map as interictal events, and was free to have the best-fitting timecourse. (**j**) Residuals between seizure and standing wave model are small in the first ~0.3 s after onset, but subsequently become prominent, when the standing wave model fails to capture the propagation typical of seizures.

Supplementary Movie 2). Seizures that lasted > 30 s, indeed, generalized to most (or all) of the imaged hemisphere (**Figure 7.8**). Interictal and ictal events had similar origins: 94±4% of events started in V1, close to the pipette used to apply picrotoxin and record the LFP (starting positions clustered within a radius of 0.32±0.12 mm).

For interictal events, the evolution of activity in space and time was a simple standing wave: they rose and then abated while engaging a fixed spatial profile (**Figure 7.7d-h**). In a standing wave, the responses in all locations follow a similar time course, so that the sequence of images can be represented by the product of a single spatial profile (an image) and a single time course (**Figure 7.7d-e**). We fitted this model to the interictal events and obtained predictions that resembled closely the actual measurements (**Figure 7.7e**), accounting for 94.0±0.4% of the variance of the data (**Figure 7.7g**, *blue dot*). Indeed, the residuals between the data and the predictions of the model were small (**Figure 7.7**), with the maximal residual of $\Delta F/F < 10\%$ (Figure 3**h**, *blue trace*), a negligible fraction of the $\Delta F/F$ ~125% typical of interictal events.

Seizures initially closely resembled interictal events, but then propagated extensively (**Figure 7.7h-i**). A standing wave model with the spatial profile of interictal events was appropriate to describe the beginning of the ictal events, but it became inadequate after a few hundred milliseconds (**Figure 7.7i-j**): it progressively overestimated the activity at the focus (negative residual, **Figure 7.7j**), while underestimating the activity in the surrounding region (positive residual, **Figure 7.7j**). Consequently, the quality of this model's predictions deteriorated sharply with time (**Figure 7.7g,h**). Seizures, thus, start as standing waves just as interictal events, but then they propagate beyond a common initial spatial profile to engage wider regions of cortex.

7.2.4 Interictal events engage contiguous and homotopic regions

The spatial profile common to interictal events and early seizures typically encompassed not only the focus, but also one or more distinct regions that were homotopic, i.e. that shared the same retinotopic preferences (**Figure 7.10a-d**). For

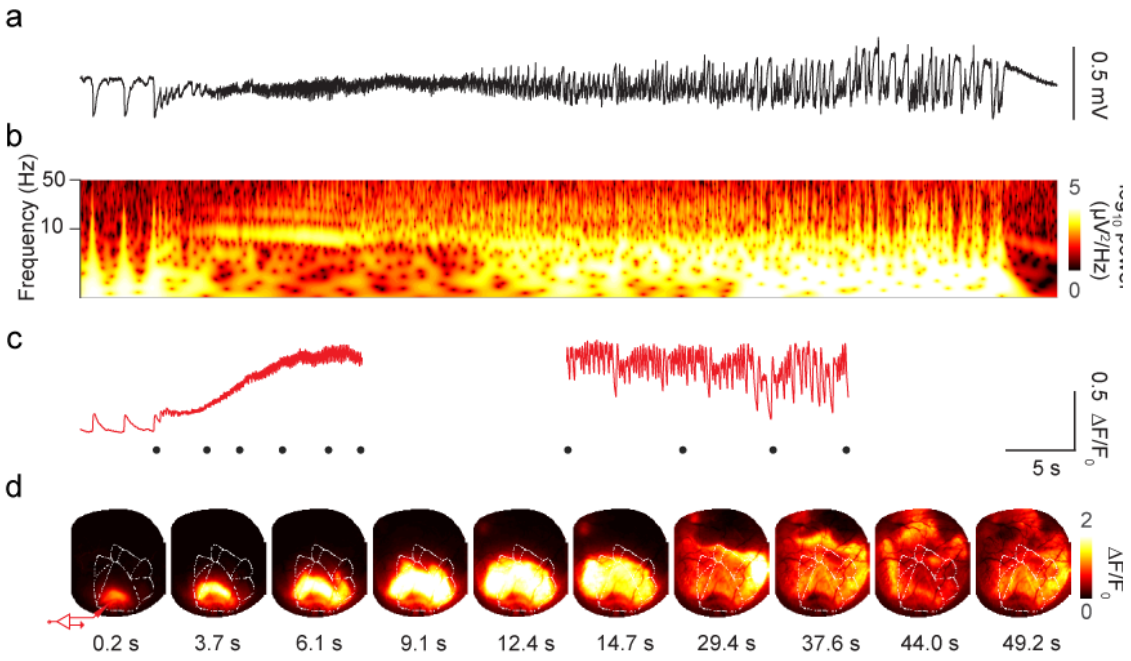

Figure 7.8 Prolonged seizures invade the whole imaged hemisphere. (**a**) LFP recording from the focus. (**b**) Morlet-wavelet spectrogram of the recorded LFP. (**c**) GCaMP6f signal averaged across the whole imaging window, aligned to the LFP (**d**) Single frame snippets from the GCaMP movie, corresponding the black dots in panel **c.** The red cartoon electrode indicates the site of Ptx injection and LFP recording

instance, two distinct lobes are clearly visible 60-100 ms into the example epileptiform events (**Figure 7.7a, c**). A first larger lobe lies in area V1 and a second smaller lobe in area LM (**Figure 7.10a**). To characterize these two lobes, we drew a line connecting V1 to LM along the direction of maximal change in preferred horizontal position previously obtained when retinotopy was mapped (**Figure 7.10b**). The profile of activation along this line was bimodal (**Figure 7.10c**), with the activation in V1 being 8±2 times higher and ~2 times wider than in LM (n = 4 mice, **Figure 7.9a-d**). Crucially, the two activations involved regions with matching retinotopic preference (**Figure 7.10d**). The retinotopic preferences of the two peaks, indeed, were not significantly different (p= 0.4, Wilcoxon signed rank test), and the retinotopic preferences of the two peaks were significantly correlated (r = 0.48, p<0.001 **Figure 7.9e, f**).

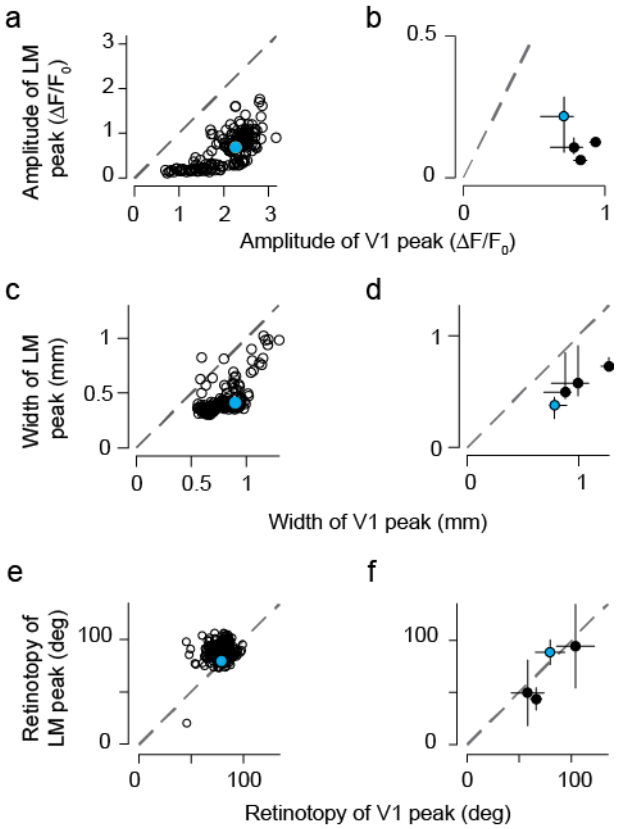

Figure 7.9 Characterizing the two homotopic responses during interictal events. (**a-f**) Response profiles from Figure4 were fit with two Gaussians. The left panels (**a**, **c**, **e**) summarize the fit for each event from the example animal in Figure 4; the right panels (**b**, **d**, **f**) show the data from every animal, median ± first quartile. (**a-b**) The peak response in V1 is plotted against the peak response in LM. To allow comparison between different GCaMP variant, data where normalized to the max V1 response in the right panel. (**c-d**) The standard deviation of the Gaussian fit in V1 is plotted against the standard deviation of the fit for LM. (**e-f**) The retinotopic position of the fit in V1 is plotted against the retinotopic position of the peak in LM.

These observations indicate that two factors determine the spatial profile of interictal events and early seizures: one local, causing contiguous spread and one distal, causing homotopic spread (**Figure 7.10e-i**). The local factor could, in principle, arise from disinhibition (spread of picrotoxin, loss of $GABA_A$ receptor electrochemical driving force, or depolarization block of interneurons), from local excitatory circuits, or from non-synaptic mechanisms; its impact falls off with cortical distance (**Figure 7.10e**). The distal factor, by contrast, arises from the same axonal and synaptic organization that supports homotopic connectivity, whose impact decreases with retinotopic distance (**Figure 7.10h**). We combined these two effects into a simple multiplicative model (**Figure 7.10e,g,h**), and found that with only 6 parameters the model provided good fits to the data (**Figure 7.10f**). The function of retinotopy, in particular, was described by one key parameter, the angular standard deviation σ. As this parameter grows, the function becomes closer to a constant, and retinotopy plays a lesser role in the profile of the epileptiform events. When fitting the data, σ consistently took values <40 deg (**Figure 7.10i**) confirming an important contribution of retinotopy

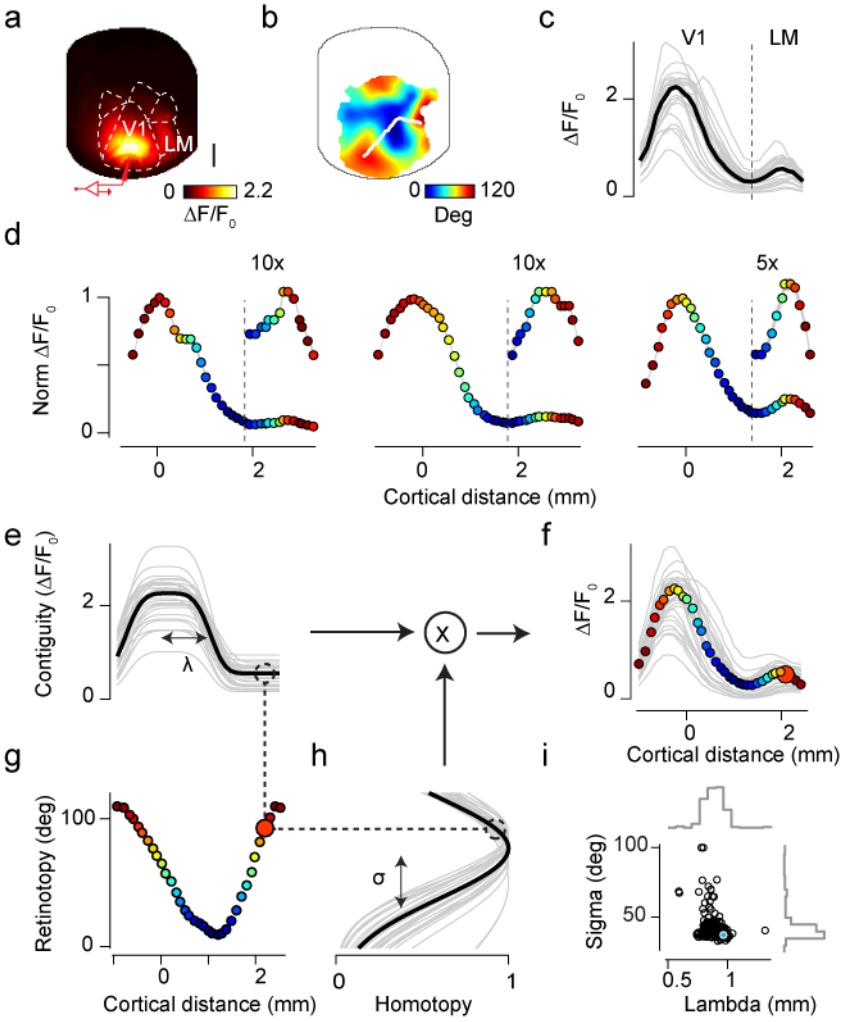

Figure 7.10: Interictal events and early seizures engage both contiguous spread and homotopic connectivity. (**a**) Average spatial profile of interictal events measured in one mouse, obtained by averaging the maximum projection map across events (n = 242). The cartoon electrode indicates the site of Ptx injection and LFP recording. Scale bar is 1 mm. (**b**) Map of retinotopy (preferred horizontal position) with a line from the focus in V1 to area LM, joining regions of interest (ROIs) with same preferred vertical position as the focus in V1. (**c**) Peak dF/F response at each ROI in **b** for a representative interictal event (black) and for 30 other interictal events (gray). (**d**) The spatial profile averaged across interictal events for 3 representative animals (two measured with GCaMP3 and the third with GCaMP6), where ROIs were drawn with the same strategy as in **b.** Dot colour indicates the retinotopic preference of the corresponding ROI. Insets show the magnified profile of responses in area LM. The grey shaded line (extremely thin) represents mean± s.e.m. (**e-h**) The bimodal profile of activity for each interictal event is well described by the dot product of a function of cortical distance from the focus (**e**), and a function of retinotopic distance from the focus (**h**). Dotted lines illustrate how the model predicts the second peak of activation ~2 mm away from the focus (**f**), due to the similar retinotopic preference of that region and the focus (**g**). (**i**) Distribution of fit parameters for the example animal, indicating a consistent role of contiguous spread and homotopic connectivity across events.

(**Figure 7.10h**), which in turn produced a clear secondary peak in activity (**Figure 7.10f**). Homotopic connectivity thus plays a key role in determining the spatial profile of interictal events and early seizures. Nonetheless, at this early stage, homotopic connectivity is not sufficient to recruit in downstream territories the same levels of abnormal activity recorded at the focus. Retinotopic modulation was present in all mice, but the strength of its contribution varied across animals (**Figure 7.10d**), possibly reflecting experimental variability in the induction of the focus and levels of expression or sensitivity of the calcium indicator.

7.2.5 Seizures propagate along homotopic connectivity

These same two factors – contiguous and homotopic – also determined the subsequent evolution of seizures, when the standing wave gave way to escalating propagation of activity (**Figure 7.11a-d**). As we have seen, seizures propagated to engage most of the visual cortex, and often beyond, producing activity levels comparable to those observed at the focus (**Figure 7.11a** and **Figure 7.8**). The pattern of propagation can be seen by following the activity of individual loci between the focus in area V1 and the homotopic location in area LM (Figure **7.11b**, **c**). In the example shown, the focus in V1 had a retinotopic preference ~100 degrees away from the middle of the visual field, which is indicated in orange in the map of retinotopy (Figure **7.11b**). Accordingly, at that location the calcium traces show seizure activity with the earliest onset (Figure **7.11c**, *top arrow*). This activity progressively invades further V1 locations, eventually reaching the border with area LM, where receptive fields are in the middle of the visual field (0 degrees, **Figure 7.11c**, *blue traces*). Well before having reached those areas, however, the seizure has already reached a distal region: the portion of LM with the same retinotopic preference as the focus (**Figure 7.11c**, *bottom arrow*). For instance, 6 to 8 s into the event, the seizure activity shows a bimodal profile, being stronger in the homotopic regions in LM than in regions of V1 that are closer to the focus (Figure **7.11d**).

The two factors, contiguous and homotopic, both contributed approximately linearly to the time course of seizure propagation (**Figure 7.11e-j**). To measure the time it took a seizure to invade different regions, we defined 'delay to seizure

invasion' as the time taken for each pixel to reach 60% of its maximum activity. Consistent with the observations made above, a map of this quantity shows activations occurring earlier in the V1 focus and in the homotopic region in LM than in other locations (**Figure 7.11h**), and a plot of delay along a line from V1 to LM shows the delay growing with distance while displaying two distinct troughs (**Figure 7.11e**). When averaging these measures across mice, we found that delay strongly correlated with distance ($r = 0.81$, $p < 10^{-7}$, $n = 64$ seizures in 4 mice), with an average propagation speed of 0.48 ± 0.03 mm s^{-1} (**Figure 7.11f**). However, closer inspection of this linear prediction based on distance shows that it underestimates the delays of proximal territories and overestimates those of distal territories (**Figure 7.11f**). The corresponding residuals were highly correlated with retinotopic distance from the focus ($r = 0.82$, $p < 10^{-24}$, **Figure 5g**). Indeed, if delay to cortical invasion were solely due to cortical distance, it would grow radially from the focus and display concentric rings (**Figure 7.11i**). The map of residuals instead reveals that it overestimates delays in territories retinotopically close to the focus, especially in higher visual areas (**Figure 7.11j**, *blue negative residual*), and underestimates delays in distal territories in V1 and in regions outside the visual areas (**Figure 7.11j**, *red positive residual*). These results indicate that delay to seizure invasion depends approximately linearly on two factors: one contiguous, which grows with distance in cortex, and one homotopic, which grows with distance in visual preference

7.2.6 Seizure oscillations propagate along homotopic connectivity

Homotopic connectivity also determined the timing of individual oscillatory waves of activity during seizures (**Figure 7.13**). Once a territory was invaded by seizure activity, it displayed striking oscillations in the range of 6-11 Hz (**Figure 7.11c**), evident both in the LFP and in the GCaMP fluorescence (**Figure 7.13a-d**). These oscillations started in the focus and spread with the seizure to cover the entire visual cortex and beyond.

To isolate these oscillations from the slower spreading activity, we filtered the

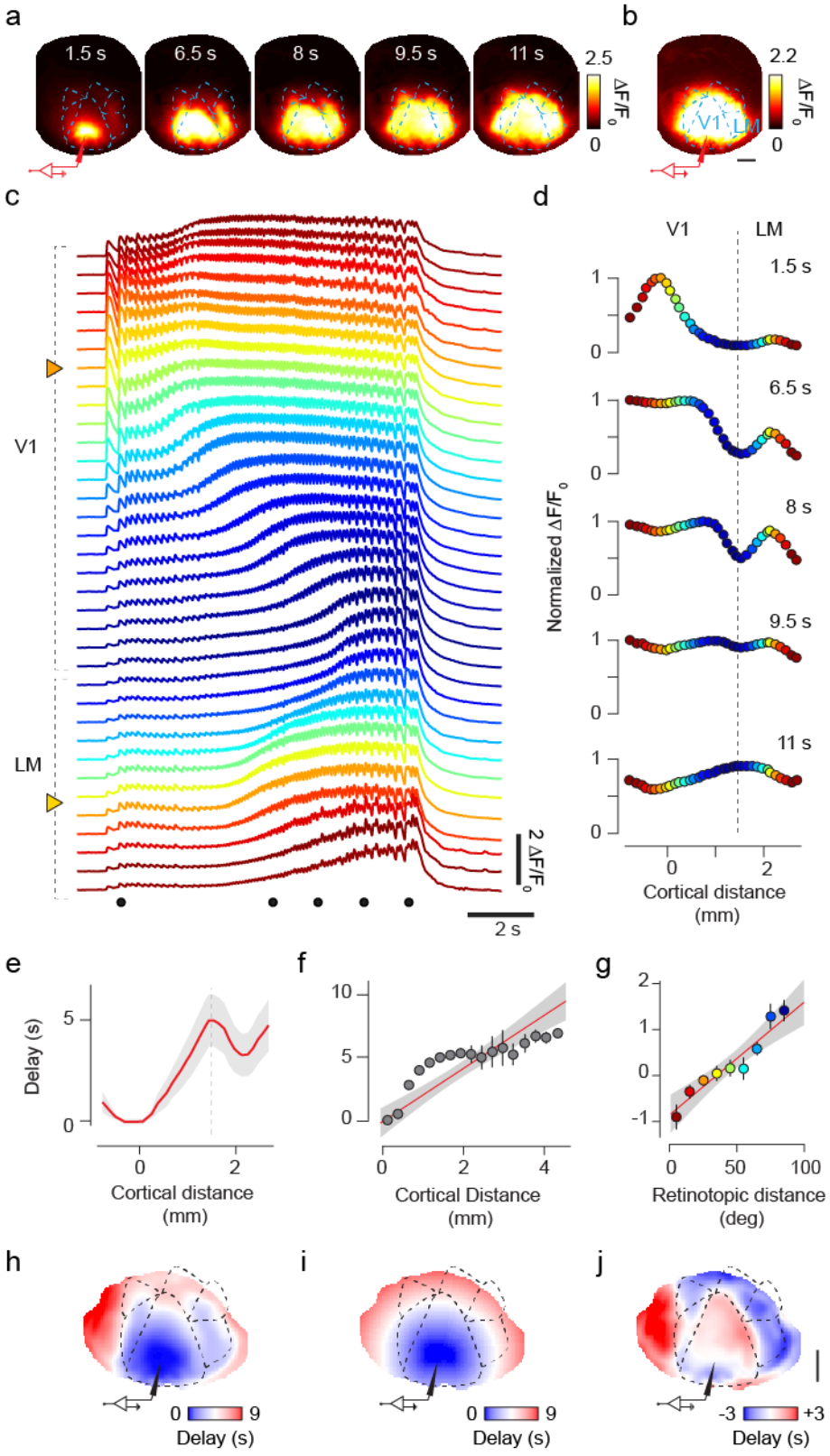
a
1.5 s
6.5 s
8 s
9.5 s
11 s
2.5
ΔF/F0
0
b
2.2
V1
LM
c
V1
LM
2 ΔF/F0
2 s
d
V1
LM
1.5 s
6.5 s
8 s
9.5 s
11 s
Normalized ΔF/F0
Cortical distance (mm)
e
Delay (s)
Cortical distance (mm)
f
Cortical Distance (mm)
g
Retinotopic distance (deg)
h
0
9
Delay (s)
i
0
9
Delay (s)
j
-3
+3
Delay (s)

Figure 7.11: Seizure propagation recruits homotopic regions of cortex. (**a**) Frames imaged in a representative seizure. Labels indicate time from seizure onset, and cartoon electrode indicates the site of Ptx injection and LFP recording. (b) Maximum extent of seizure invasion averaged across 14 seizures in this mouse. (**c**) Single-trial time course along the ROIs in Figure 4**b**, for the seizure in **a**. Dots mark the representative times in **a** and **d**. Arrowheads mark the focus in V1 and homotopic region in LM. (**d**) Spatial profile of the seizure in **c**, at representative times, normalized to their maximum. (**e**) Seizure invasion delay averaged across seizures. Shaded area represents s.e.m. (**f**) Same, averaged across 4 animals. Error bars indicate two s.e.m. Line: linear fit, with shaded 95% confidence interval. (**g**) The residuals of the linear fit in **f** reveal a clear dependence on retinotopic distance from the focus. Line: linear fit, with shaded 95% confidence interval. (**h**) Map of delay to seizure invasion, averaged across 14 seizures in one mouse. (**i**) Prediction of that map based solely on cortical distance from the focus. (**j**) Residuals of that prediction. Scale bars are 1 mm.

traces between 6 and 11 Hz, and used the Hilbert Transform to compute maps of amplitude and phase of the oscillation at each time point (Supplementary Movie 3). For a large portion of a seizure duration (for the first 7.1±0.8 s), the seizure focus tended to act as a pacemaker for the oscillations: each oscillatory wave rose at the focus and propagated on the surface of the cortex, with homotopic regions oscillating almost in synchrony with activity in the focus. The spatiotemporal pattern of these oscillations was consistent across oscillations and across seizures (**Figure 7.13f,g,** Supplementary Movie 4) and was closely related to the map of retinotopy (**Figure 7.13e**). Similar results were seen in other mice (**Figure 7.13h-m**). Just like the slow spread of seizure activity, therefore, the faster oscillations within the seizure tended to propagate along the same circuits that support neural signals during normal cortical activity. Occasionally, however, oscillatory waves showed more complex patterns of propagation such as spiral waves (Viventi et al., 2011) (**Figure 7.14**). To characterize the individual oscillations in a seizure (**Figure 7.14a**), we took the Hilbert Transform and assigned an amplitude and a phase to each pixel.

We then measured the variance of the phase across space (**Figure 7.14b**). In most oscillations, the phase had low variance. These were the homotopic waves, where activity oscillated in synchrony at the focus and in homotopic regions, and shortly afterwards (within ~13 ms, **Figure 7.13**) in the remaining regions. In occasional oscillations, instead, the variance of the phase was higher, and

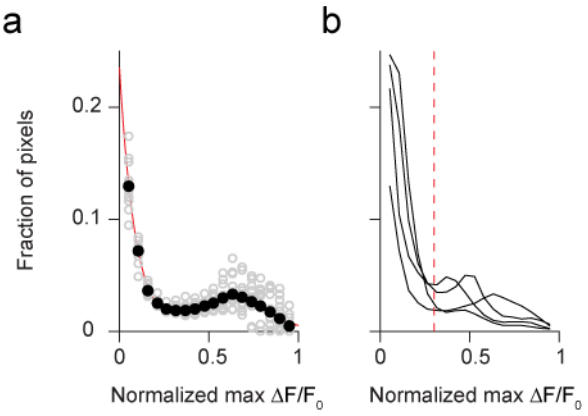

Figure 7.12 Selection of pixels recruited into the seizure. (**a**) Distribution of maximum pixel intensities during seizures for one animal (n= 14), normalized to absolute maximum. Black dot's shows the average distribution, gray dots single trial distribution. Red line is a double Gaussian fit to the average data, individually normalized to absolute maximum. (**b**) Average distribution of maximum pixel intensities during seizures for 4 animals. On average, a threshold of 0.3 (dashed line) separates well the population of pixels with greater activity.

described a spiral pattern of activity(Viventi et al., 2011) (**Figure 7.14c**) where the phase varied orderly around a pinwheel point where the amplitude tended to be lower (**Figure 7.14d**). Such spiral waves were rare at seizure onset, but became more common towards the end of the seizure (**Figure 7.14e,f**). Once a seizure spread beyond the visual cortex, moreover, the patterns of activity became more complex, and the leading regions in the oscillations were no longer confined to the original focus of the seizure (Supplementary Movie 3).

7.3 Discussion

By exploiting the potential of widefield imaging and of genetically encoded calcium indicators, we were able to study the spatiotemporal evolution of epileptiform activity in the awake cortex and relate this evolution to the underlying pattern of connectivity. Focal picrotoxin injections induced prolonged seizures with clear behavioural correlates, separated by numerous brief interictal events. In the first few hundred milliseconds from their onset, the two types of event were extremely similar: they were standing waves of activity with a fixed spatial profile. Afterwards, however, interictal events subsided while seizures went on to invade much of visual cortex and beyond. Individual 6-11 Hz waves of activity within seizures also spread in a similar manner.

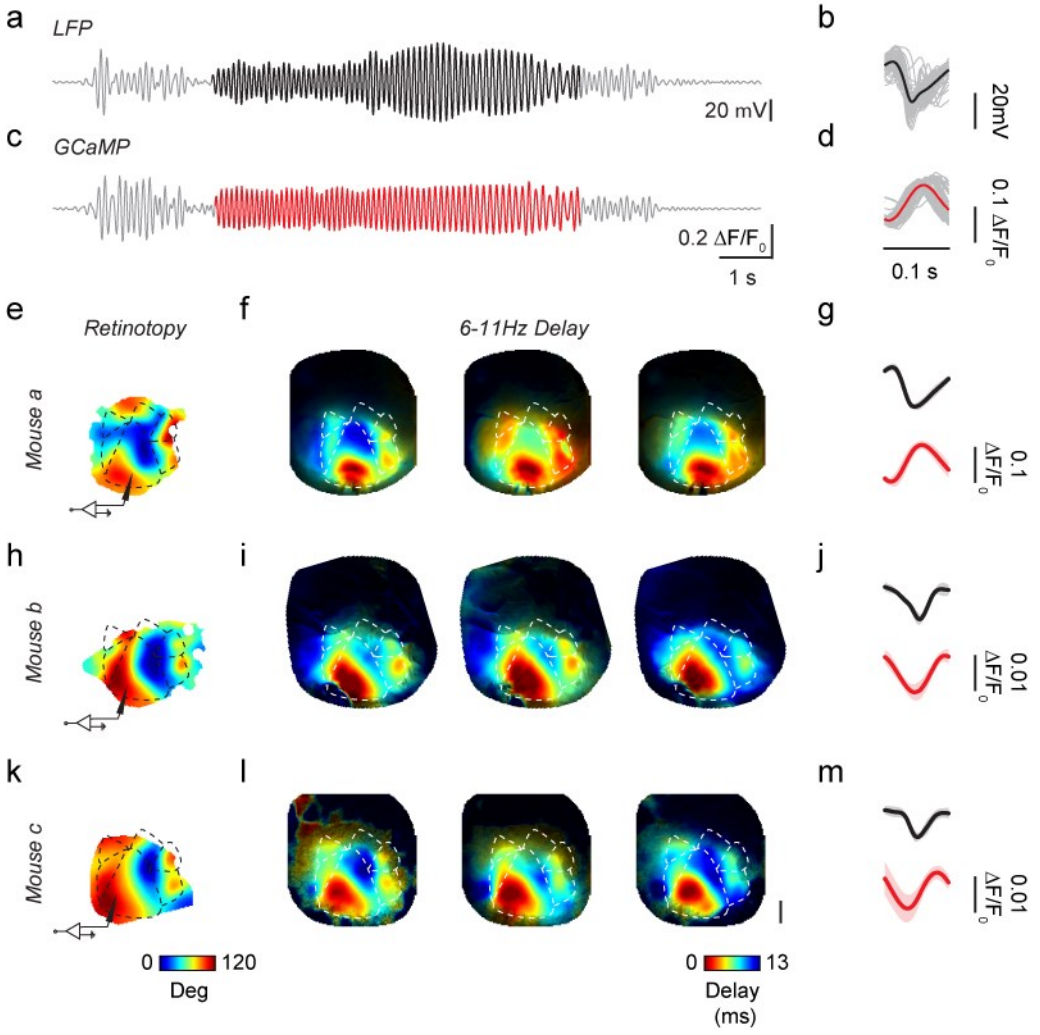

Figure 7.13: Homotopic propagation of 6-11 Hz oscillations during seizures. (**a**) LFP recording of the seizure in Figure 5**a**, bandpass filtered between 6 and 11 Hz. Highlighted in black is an epoch of coherent oscillations driven by the focus, used for the analysis in the next panels. (**b**) Cycle average of the 6-11 Hz oscillation from the unfiltered LFP trace. Gray traces show the individual cycles of the oscillation. (**c**, **d**) Same as **a, b**, for the GCaMP fluorescence measured at the focus. Oscillation highlighted in red. (**e**) Retinotopic maps for an example animal. The cartoon electrode indicates the site of Ptx injection and LFP recording, the dashed line represents visual areas contours. (**f**) Oscillatory delay for three example seizures from this example animal. Delay was obtained from the 6-11 Hz Hilbert phase referenced at the focus, averaged across all cycles of the oscillation for a given seizure. (**g**) Average LFP cycle (top) and average GCaMP fluorescence (bottom), averaged across all the seizures for this animal. Shaded area represents the standard deviation. (**h-m**) Same as **e-g** for six other seizures in two other mice. In all seizures and all mice, the delay of the oscillation faithfully recapitulates the retinotopic maps. Scale bar: 1 mm.

Strikingly, all these epileptiform phenomena respected the connectivity of the visual cortex that underlies normal sensory processing. Specifically, the phenomena were shaped by a combination of two factors, one local and dependent on cortical distance from the focus, and one distal and dependent on homotopic relationship with the focus. Both factors determined the shape of the common spatial footprint characteristic of interictal events and of seizure onset (**Figure 7.10**). Both factors determined the slow spread of the seizures (Figure 5). Both factors also determined the fast spread of the prominent oscillations that accompany the seizures (**Figure 7.13**).

These local and distal factors likely reflect different mechanisms. Distal propagation must rely on synaptic barrages transmitted from the seizure focus through long-range, excitatory pathways connecting homotopic regions. Local propagation, in addition, can involve collapse of local inhibition (Schevon et al., 2012; Trevelyan et al., 2007), although evidence exists for a host of non-synaptic mechanisms such as gap junctions among neurons (Gyengesi et al., 2003) or astrocytes (Bedner et al., 2015), alterations in the electrochemical gradients of chloride (Huberfeld et al., 2007; Staley et al., 1995) or potassium (Voipio and Kaila, 2000), endogenous electric fields (Qiu et al., 2015; Zhang et al., 2014) and defective astrocyte calcium signalling (Carmignoto and Haydon, 2012).

The combination of widefield imaging and genetically encoded calcium indicators represents a substantial advance over electrophysiological recordings performed at a few sites (Chervin et al., 1988; Wadman and Gutnick, 1993)(Goldensohn et al., 1977), and complements the measures that can be obtained with electrode arrays(Schevon et al., 2012)(Viventi et al., 2011). Widefield imaging has long been recognized as a promising alternative, and has been applied to measure hemodynamic signals(Schwartz and Bonhoeffer, 2001), voltage-sensitive fluorescent dyes (Haglund, 2012), or organic calcium dyes (Daniel et al., 2015). These techniques, however, provide much weaker signals than genetically encoded calcium indicators. Such indicators can be targeted to specific types of neurons, have high signal to noise ratios and provide a faithful representation of the underlying neural activity, with appropriate spatial and

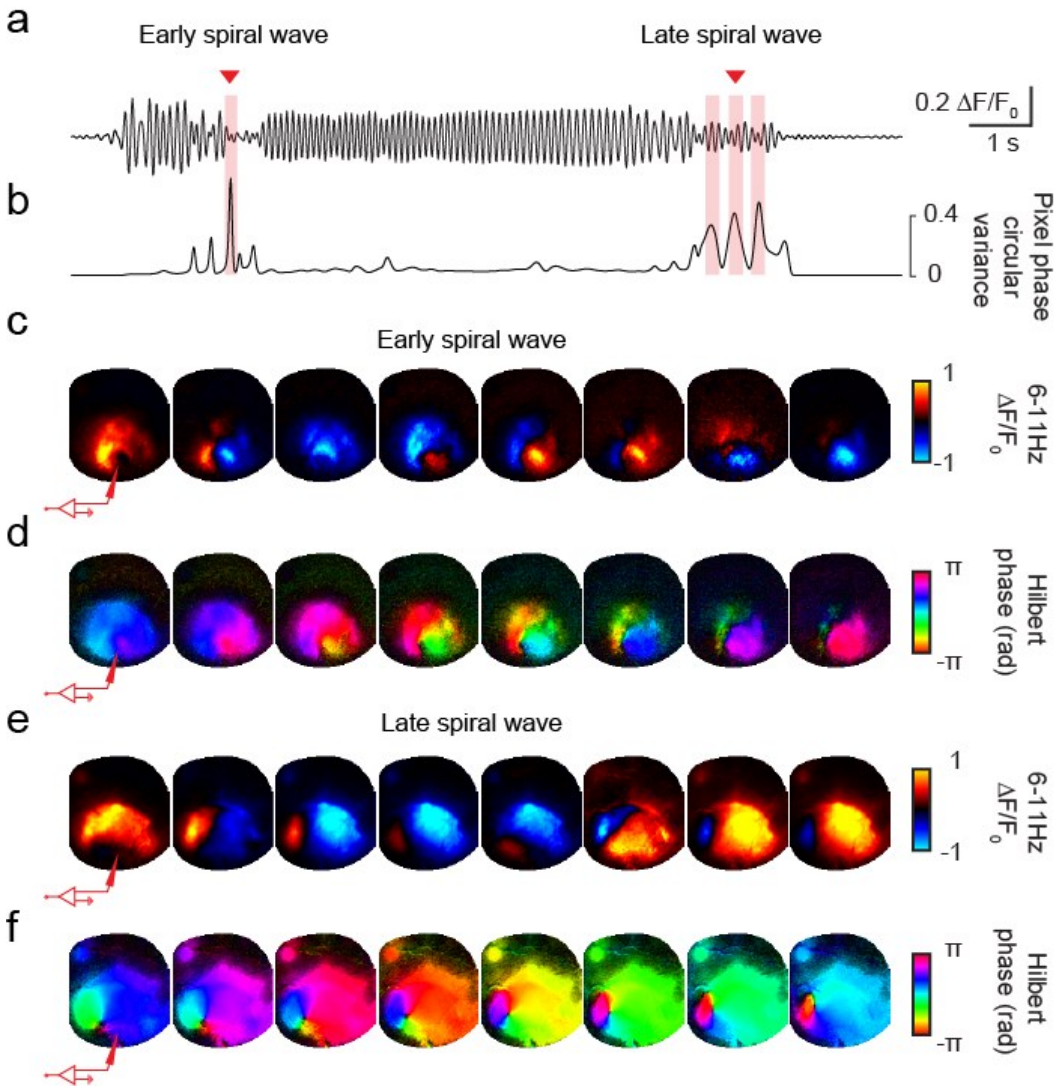

Figure 7.14 Spiral waves during seizures. (**a**) Average GCaMP6 signal from the focus during a seizure, band-pass filtered between 6 and 11 Hz. Shaded boxes highlight cycles when spiral waves were recorded. (**b**) Time course of circular variance of the phases for pixels with significant oscillation amplitude, computed across each frame. (**c**) Example oscillation cycle showing the propagation of an early spiral wave (highlighted in **a**). For each frame, pixels were normalized to the maximum absolute value for visualization purpose. (**d**) Hilbert transform representation of the example early spiral wave from panel **c**. For each pixel, hue represent the phase, while saturation represent amplitude of the oscillation. (**e, f**) Same as in **c, d** for the late spiral wave highlighted in **a**. In both spiral waves examples, note the calcium activity revolving around a pinwheel with reduced oscillation amplitude. The cartoon electrode indicates the location of the LFP pipette

temporal resolution (Carandini et al., 2015; Chen et al., 2013; Madisen et al., 2015). Indeed, the signal to noise ratio of the calcium indicators used here allowed single trial analysis without the need to average responses. Finally, recording in awake animals avoided the confounding effects of anaesthesia.

Somewhat unexpectedly, we also demonstrate that GCaMP can report oscillations as fast as 6-10 hz. Such result is less surprising when considering that the GCaMP variants deployed here have a fast rise and decay time, 45 ms and 140ms respectively for GCaMP6f, with GCaMP3 being just few tens of milliseconds slower (Akerboom et al., 2009; Chen et al., 2013), and that one of the major sources of widefield imaging recordings are dendrites and axons, where calcium dynamics are much faster than at neuronal somas. Furthermore, recruitment of silent populations of neurons into the seizure, progressing at each cycle of a fast oscillation, could create a gradual ramping activity, by means of successive sharp increases in fluorescence, which would eventually contribute to the oscillations after filtering.

These differences in methods may explain a difference between my results and those of earlier studies. Whereas we found a strong relationship between the propagation of epileptiform activity and the underlying functional architecture, previous widefield imaging studies found only a weak relationship (Haglund, 2012) or no relationship(Schwartz, 2003; Schwartz and Bonhoeffer, 2001). In addition to the choice of indicators, these discrepancies could be due to differences in the types of functional architecture taken into consideration. Our study, in mouse, asked how propagation depends on the organization of visual cortex into retinotopic areas, whereas the previous studies(Haglund, 2012; Schwartz, 2003; Schwartz and Bonhoeffer, 2001), in carnivores, asked whether propagation depends on the organization of V1 into regions with similar orientation preference. It is likely that connectivity is stronger between two homotopic regions in different visual areas than between two V1 regions having the same orientation preference.

We did not observe decreases in fluorescence in regions surrounding epileptiform activity, as one might have expected from an "inhibitory surround" (Prince and Wilder, 1967). This finding may seem to be in contradiction with an earlier study of hemodynamic signals, which were found to be decreased in the region around the focus(Schwartz and Bonhoeffer, 2001). Neither our study nor the previous study, however, employed the ideal methods to probe inhibition. Indeed, decreases in hemodynamic signals cannot be interpreted as increases in inhibition, because interneuron activation has the opposite effect (Anenberg et al., 2015). Our study, in turn, measured calcium signals only in excitatory neurons, and these signals reflect mostly supra-threshold activity and may be insensitive to hyperpolarization below threshold. The question of what interneurons do in the region surrounding the focus thus remains open, and can be addressed in future studies by genetically targeting those neurons for widefield imaging.

The striking similarity that we found between interictal events and the onset of seizures suggests that the two are mechanistically related. Interictal events have long been recognized as an electrophysiological marker of epilepsy(Muldoon et al., 2015), but have no or only subtle clinical correlates (Kleen et al., 2013). They have been proposed either to prevent seizure initiation (De Curtis and Avanzini, 2001)or to act as a prelude to seizures(Staley et al., 2011). It has, furthermore, been proposed that interictal events dominated by GABAergic signalling give way to glutamatergic pre-ictal events (Huberfeld et al., 2011). Our results do not reveal any detectable differences between interictal events and seizures during the first few hundred milliseconds: both are well modelled as standing waves involving the same temporal profile over a fixed spatial territory. It remains to be determined whether a qualitative or quantitative difference in the underlying cellular mechanisms lead to these events dying down (and thus become interictal) or turning into propagating seizures. A plausible distinction is that seizures result from escape from an inhibitory restraint(Trevelyan et al., 2006). Indeed, the smaller peak of activity in LM during interictal events is consistent with a barrage of feed-forward activity that fails to

recruit a self-sustaining discharge. To test this hypothesis, once again, it would be useful to express the calcium indicator in inhibitory neurons and compare their activity in interictal events and seizures.

The seizures induced in our preparation also bear similarities with seizures observed in patients. Their speed of propagation across the cortex, ~0.5 mm s-1, is consistent with measurements obtained with high-density electrode arrays from seizures recorded in humans with cortical epilepsy (Schevon et al., 2012). Moreover, propagation to LM is consistent with recruitment of more distant areas at short latency. Further, our results demonstrate that cortico-cortical connections that support higher visual processing have an important role in determining the propagation of seizures originating in V1. The involvement of higher-order visual cortex is consistent with seizures seen in occipital epilepsy, which commonly includes both elemental symptoms in specific areas of the visual field and the more complex visual hallucinations(Blume et al., 2005) that might be expected from the engagement of higher visual areas. Nonetheless, it remains an open question whether homotopic spread to higher visual areas can rest entirely on cortico-cortical connections or if it requires subcortical signaling through common thalamic relays.

Despite these similarities with human focal epilepsy, one should be careful when interpreting the effects of acute application of chemoconvulsants. For instance, small variations in the extent and direction of chemoconvulsant spread could determine differences in the pathways that are recruited in each experiment. Moreover, the acute disinhibition or overexcitation at the focus seen with chemoconvulsants may be fundamentally different from the mechanisms causing focal epilepsy in humans. Here we aimed to reduce these risks by minimizing the amount of picrotoxin released at the focus, and indeed, we observed similar effects across experiments. Moreover, we observed similar epileptiform events following the administration of both picrotoxin and pilocarpine, two compounds with markedly different pharmacological profile. Finally, much of our analysis focuses on seizure propagation into healthy cortical territories, well beyond the pharmacologically-altered focus. In addition, some of

the seizure we recorded generalised across the cortex, and triggered behavioural correlates typical of secondary generalisation such as extreme pupil dilation, abnormal running and tonic limb and tail movements (Wykes et al., 2012). Such observations confirmed that, while our experimental model is based on an acutely disinhibited epileptic focus, the mice were experiencing full behavioural seizures as opposed to mild acute cortical hyperactivity. These considerations increase the likelihood that the dynamics of the distal propagation we describe could be common to human focal epilepsies.

7.4 Supplementary Movies

Supplementary movies can be downloaded from the hyperlink associated to each label.

Supplementary Movie 6.1: Example interictal events from 3 example animals. *Leftmost panels*: the retinotopic maps for each example animal. *Right panels*: 4 representative interictal events for each animal. The frame rate is 35 frames/s, two times slower compared to real time. Each event was normalized to its maximum $\Delta F/F$ value.

Supplementary Movie 6.2. Example seizures from 3 example animals. *Left column*: retinotopic maps for each example animal. *Remaining panels*: 4 representative seizures for each animal. The frame rate is 35 frames/s, 2 times slower compared to real time. Each event was normalized to its maximum $\Delta F/F$ value.

Supplementary Movie 6.3. Hilbert analysis of propagation of 6-11Hz oscillations from the example seizure in Figure 6 a,b and Suppl. Figure 8. *Top left panel*: GCaMP6f $\Delta F/F_0$ movie. *Top right panel*: 6-11Hz band pass filtered GCaMP6f signal. *Bottom left panel:* Hilbert amplitude of 6-11Hz oscillations during the same seizure. *Bottom right panel*: Hilbert phase of 6-11Hz oscillations for the same seizure. For each pixel, the color indicates the phase of the oscillation, while the saturation is proportional to the amplitude of the oscillation. For this panel only, the saturation was clipped at the 70^{th} percentile of the maximum amplitude for display purposes.

Supplementary Movie 6.4. Example cycle average of 6-11 Hz oscillations during one seizure. *Left panel*: cycle average of the filtered 6-11Hz GCaMP oscillation, normalized to maximum and with retinotopic map superimposed. *Right panel*: cycle average of the Hilbert transform phase of the oscillation. The saturation indicates the amplitude of the oscillation for each pixel.

Chapter 8

Conclusions

This thesis investigated the neuronal circuits underlying visual processing and epileptic activity propagation in the mouse visual cortex. In the first part of the Thesis, I discussed the functional principles that organise the connectivity between visual neurons: these principles form the anatomical substrate of visual computations, and constrain the flow of physiological activity in circuits that process salient features of visual stimuli. In the second part of the Thesis, I asked how the very same principles relate to epileptic seizures, which represent a dramatic transition from normal propagation of neuronal signals to activity spreading in a pathological and escalating manner. In this Conclusions, I discuss the importance of these findings and outline future directions of investigation that will stem from this Thesis.

8.1 Functional organisation of presynaptic networks in V1, and beyond

This Thesis expands the neuroscience toolbox with novel methods to achieve robust single cell initiated monosynaptic circuit tracing and recording *in vivo*. I devised an efficient experimental pipeline that coordinates neuroanatomical reconstruction, connectivity tracing and volumetric two-photon imaging in awake animals to yield simultaneous recordings from single cortical neurons, their presynaptic networks and the surrounding neuronal population. Such pipeline, in my hands, nearly triplicate the success rate of rabies virus connectivity tracing *in vivo* with respect to published protocols.

The detailed technical protocol I provided promises to be a powerful tool for the field of functional connectomics (Reid, 2012). Functional connectomics, have mostly focused on primary sensory areas, because of their well characterised

physiology and relatively straightforward methods to elicit sensory neuronal responses (Harris and Mrsic-Flogel, 2013; Reid, 2012). Nonetheless, recent research is starting to reveal how more complex neuronal dynamics in brain association areas such as secondary visual cortical areas or parietal regions support navigation or decision making during tasks (Carandini and Churchland, 2013; Wang, 2012). In these areas, the neuronal code appears as sequences of neuronal activity signalling the animal's progression through the task's events (Hanks et al., 2015; Harvey et al., 2012). How the neuronal connectivity determines such neuronal code is entirely an open questions. I envision that the combination of physiology and neuroanatomical tracing presented herein will prove a fundamental tool to answer this questions, in particular with high-yield and accurate behavioural paradigms (Burgess et al., 2017; Hanks et al., 2015).

Importantly, in this dissertation, I deployed a tracing strategy to uncover a potential novel principle of cortical connectivity, which underlies the development of orientation selective responses in visual neurons in the primary visual cortex (V1). I provided a complete description of the functional architecture of presynaptic networks upstream of L2 intra-telencephalon pyramidal neurons in V1. I traced detailed neuroanatomical reconstructions of the target L2 neurons and their presynaptic networks, and described with simple mathematical models their statistics in cortical space. Importantly, by interpreting these reconstructions in the context of the retinotopic map, I characterised for the first time the architecture of presynaptic networks in the retinotopic space, and showed that they form elongated clusters whose orientation correlates with the preferred orientation of the corresponding postsynaptic neurons. A similar functional connectivity rule has been described in the visual cortex of ferrets, whereby retinotopy and orientation columns can be mapped to predict the connection patterns between L4 neurons with center-sorround RF and L2/3 neurons with elongated, orientation selective RF (Mooser et al., 2004). Nonetheless, whether such principle applied to the mouse V1 was unknown, and has never been demonstrated on a single neurons basis in any species.

Moreover, I found that tuning of neurons in each presynaptic network is heterogeneous and is not necessarily aligned to the orientation preference of the corresponding starter neuron. While these finding are partially in contrast with the existing literature (Cossell et al., 2015; Ko et al., 2011, 2013), they support the idea that visual neurons receive a bulk of inputs from presynaptic partners with variant tuning (Haider et al., 2013; Kaschube, 2014; Wertz et al., 2015). It has been speculated that such feature-variant networks could be more plastic, and that such flexibility could be instrumental for learning (Harris and Mrsic-Flogel, 2013; Wertz et al., 2015). Another explanation is that L2 neurons represent more abstract features than simple motion of gratings, which are stereotyped stimuli that rarely occur naturally. Variant tuning in a presynaptic network could be the substrate of visual contour integration and object grouping (Iacaruso et al., 2017). From this viewpoint, the drifting gratings used in this study are not the optimal stimulus to understand the function of circuits in the mouse visual cortex. Supporting this possibility, I found that only ~50% of the neurons in a presynaptic network significantly responded to gratings.

Finally, whether neurons that are part of the same presynaptic network correspond to patterns of neurons that tend to be coactive remains an open question. Moreover, whether these patterns correspond to specific sensory representations, and how such patterns of neuronal activation vary with brain state will remain to be explored (Harris, 2012; Harris and Mrsic-Flogel, 2013; Hofer et al., 2011). Indeed, driver and modulatory synapses (which are weaker but constitute the bulk of the inputs) might be weighted differently during different brain states, and change the correlations between neurons and therefore sensory representations (Harris and Shepherd, 2015). While my experiments did not attempt to answer these questions, our datasets include recordings of the animal behaviour during functional imaging. Our setup allowed recorded pupil dilations, whisker movements and locomotion, which can be used as a proxy for the behavioural state of the animal (Harris and Thiele, 2011; Niell and Stryker, 2010; Reimer et al., 2014, 2016). Further analysis of our datasets, and further experiments, hold the potential to reveal if the responses of neurons within the

same presynaptic network share common modulation by various aspects of animals' behaviours.

8.2 Imaging seizures and cortical spreading depression

In this Thesis, I provided the first high resolution characterization in space-time of the propagation of epileptic activity in the awake cortex, both for seizures and for "interictal" events that separate those seizures, and related such propagation to the underlying cortical connectivity. I discovered that the two types of event are similar at first, in that they arise without leaving the focus: both are standing waves. Seizures then transition to become propagating waves: remarkably, even though seizures were a hundred times stronger than normal activity, and likely involved a breakdown of synaptic inhibition, they propagated whilst respecting the same connectivity pathways that channel activity during physiological processing.

Our characterization of the spatiotemporal flow of activity in focal cortical seizures may provide a platform to further understand the underlying mechanisms and to test therapeutic approaches. In particular, the techniques and results introduced here may help future work on the mechanisms of secondary generalization of partial-onset epilepsy. Secondary generalization sharply reduces the efficacy of surgical removal of the primary lesion (Cendes et al., 1995) and is thus a hallmark of refractory epilepsy, with substantial impact on quality of life and increased risk of mortality (Lawn et al., 2004; Walczak et al., 2001). Although secondary generalization ultimately involves subcortical structures (Motelow et al., 2015; Sorokin et al., 2016) it is commonly preceded by invasion of cortical regions (Yoo et al., 2014). The techniques introduced here may make this process amenable to study, and may provide a platform to identify and test novel therapeutic interventions.

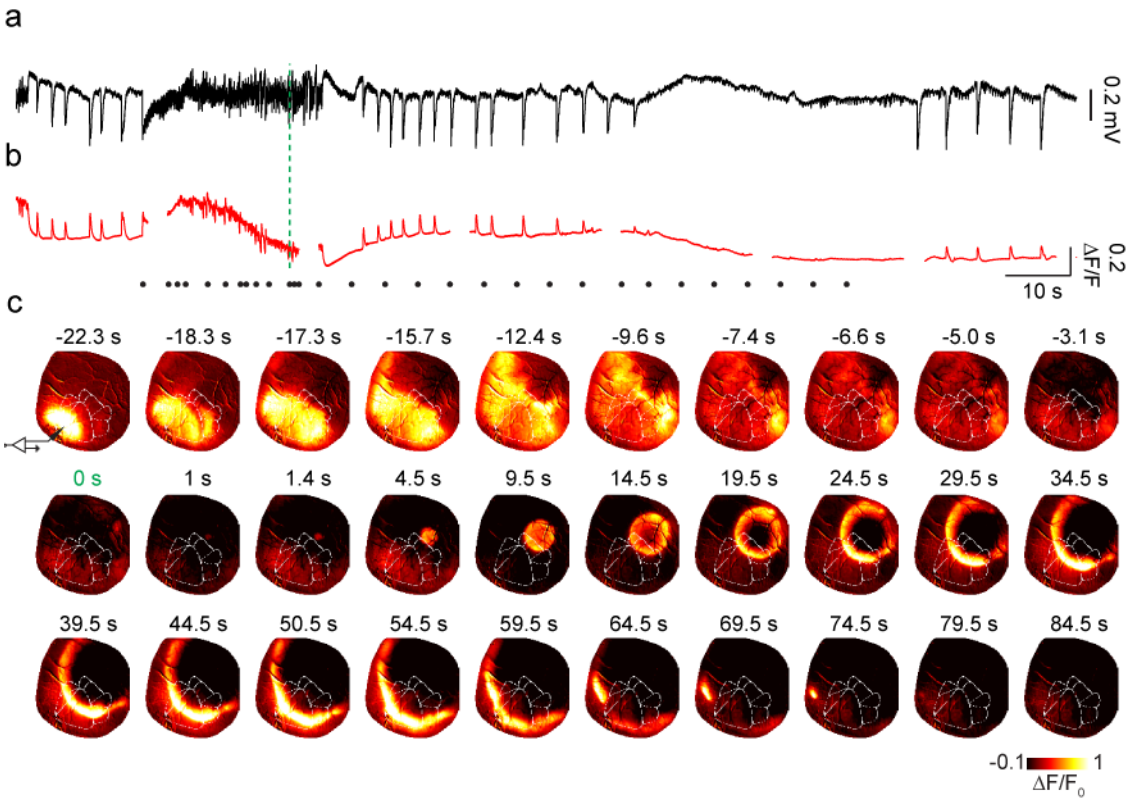

Figure 8.1: Imaging seizures and cortical spreading depression (**a**) LFP recording from the seizure focus. (**b**) GCaMP6f signal averaged across the whole imaging window, aligned to the LFP recording. The green dotted line indicates the start of the wave of cortical spreading depression. (**c**) Single frame snippets from the GCaMP6f movie, corresponding to the black dots in panel **b.** The insets indicate relative time of the snippets from the start of the cortical spreading depression. The black cartoon electrode indicates the site of Picrotoxin injection and LFP recording in the primary visual cortex. The white dotted outlines on each frame represent the primary visual cortex and higher visual areas. The Supplementary Movie 8.1 associated to this figure can be downloaded from this hyperlink.

Interestingly, further preliminary analysis of my datasets suggests a potential link between seizure termination, post-ictal depression and cortical spreading depression (Figure 8.1). Cortical spreading depression (CSD) is a slowly propagating wave of depolarization followed by suppression of brain activity: it is a remarkably complex event that involves dramatic changes in neural, glial and vascular function (Charles and Baca, 2013). CSD is thought to depend on a spreading increase of extracellular K^+ concentration, which triggers transient firing of neurons before they enter depolarisation block, accompanied by the release of cytokines (Charles and Baca, 2013; Farkas et al., 2008). CSD is thought

to underlie the aura of migraine, but can also accompany pathological phenomena such as cerebral ischaemia or haemorrhage.

We recorded several seizures longer than 30s, which generalised to most of the imaging hemisphere: these seizures were often followed by post-ictal depression of neuronal activity, which even resulted in ceased interictal firing from the pharmacologically disinhibited focus (Figure 8.1**a**,**b**, Supplementary Movie 8.1). Inspection of the wide-field movies during these epochs revealed a striking wave of cortical activation, originating between the visual and somatosensory cortex (i.e. remote from the seizure focus), and spreading radially in an almost perfect circular wave at ~3.7 mm/min (Figure 8.1**c**). This propagation was much slower than the spread of the epileptic seizures wave-front measured in my study (0.5 mm/sec). Perhaps most strikingly, the wave-front left behind absolute cortical silence, shutting down even the disinhibited epileptic focus (Figure 8.1**c**).

An intriguing hypothesis is that cortical spreading depression could be the mechanism underlying post-ictal depression often seen in scalp EEG, as well as negative symptoms that can follow focal seizures such as paralysis ("Todd's paresis"). This may have an adaptive role, because suspension of activity could potentially protect against the excitotoxicity resulting from intense synaptic activity during seizures.

The relationship between CSD and focal seizures is incompletely understood, as is the co-morbidity of epilepsy and migraine. Post-ictal headache with features of migraine is common in patients with epilepsy (Charles and Baca, 2013). Further analysis of my dataset, and future experiments in genetic models of migraine, might test if CSD and post-ictal depression share mechanisms, and if CSD plays a major role in determining seizure termination or post-ictal refractoriness.

Bibliography

Aiba, I., and Noebels, J.L. (2015). Spreading depolarization in the brainstem mediates sudden cardiorespiratory arrest in mouse SUDEP models. Sci. Transl. Med. *7*, 282ra46.

Akemann, W., Mutoh, H., Perron, A., Park, Y.K., Iwamoto, Y., and Knöpfel, T. (2012). Imaging neural circuit dynamics with a voltage-sensitive fluorescent protein. J. Neurophysiol. *108*, 2323–2337.

Akemann, W., Sasaki, M., Mutoh, H., Imamura, T., Honkura, N., and Knöpfel, T. (2013). Two-photon voltage imaging using a genetically encoded voltage indicator. Sci. Rep. *3*, 2231.

Akerboom, J., Rivera, J.D.V., Rodríguez Guilbe, M.M., Malavé, E.C.A., Hernandez, H.H., Tian, L., Hires, S.A., Marvin, J.S., Looger, L.L., and Schreiter, E.R. (2009). Crystal structures of the GCaMP calcium sensor reveal the mechanism of fluorescence signal change and aid rational design. J. Biol. Chem. *284*, 6455–6464.

Akerboom, J., Chen, T.-W., Wardill, T.J., Tian, L., Marvin, J.S., Mutlu, S., Calderón, N.C., Esposti, F., Borghuis, B.G., Sun, X.R., et al. (2012). Optimization of a GCaMP calcium indicator for neural activity imaging. J. Neurosci. *32*, 13819–13840.

Alonso, J., Usrey, W.M., and Reid, R.C. (2001). Rules of Connectivity between Geniculate Cells and Simple Cells in Cat Primary Visual Cortex. *21*, 4002–4015.

Andermann, M.L., Kerlin, A.M., Roumis, D.K., Glickfeld, L.L., and Reid, R.C. (2011). Functional specialization of mouse higher visual cortical areas. Neuron *72*, 1025–1039.

Andermann, M.L., Gilfoy, N.B., Goldey, G.J., Sachdev, R.N.S., Wölfel, M., McCormick, D.A., Reid, R.C., and Levene, M.J. (2013). Chronic Cellular Imaging of Entire Cortical Columns in Awake Mice Using Microprisms. Neuron *80*, 900–913.

Anenberg, E., Chan, A.W., Xie, Y., LeDue, J.M., and Murphy, T.H. (2015). Optogenetic stimulation of GABA neurons can decrease local neuronal activity while increasing cortical blood flow. J. Cereb. Blood Flow Metab. *35*, 1579–1586.

Araque, A., Carmignoto, G., Haydon, P.G., Oliet, S.H.R., Robitaille, R., and Volterra, A. (2014). Gliotransmitters travel in time and space. Neuron *81*, 728–

739.

Arosio, D., Ricci, F., Marchetti, L., Gualdani, R., Albertazzi, L., and Beltram, F. (2010). Simultaneous intracellular chloride and pH measurements using a GFP-based sensor. Nat. Methods *7*, 516–518.

Baird-Daniel, E., Daniel, A.G.S., Wenzel, M., Li, D., Liou, J., Laffont, P., Zhao, M., Yuste, R., Ma, H., and Schwartz, T.H. (2017). Glial Calcium Waves are Triggered by Seizure Activity and Not Essential for Initiating Ictal Onset or Neurovascular Coupling. 3318–3330.

Barretto, R.P.J., Messerschmidt, B., and Schnitzer, M.J. (2009). In vivo fluorescence imaging with high-resolution microlenses. Nat. Methods *6*, 511–512.

Barth, A.L., Burkhalter, A., Callaway, E.M., Barry W. Connors, B.C., DeFelipe, J., Feldmeyer, D., Freund, T., Kawaguchi, Y., Kisvarday, Z., Kubota, Y., et al. (2016). Response to Comment on "Principles of connectivity among morphologically defined cell types in adult neocortex." Science (80-.). *353*, 1108–1108.

Bazargani, N., and Attwell, D. (2016). Astrocyte calcium signaling: the third wave. Nat. Neurosci. *19*, 182–189.

Bedner, P., Dupper, A., Huttmann, K., Muller, J., Herde, M.K., Dublin, P., Deshpande, T., Schramm, J., Haussler, U., Haas, C.A., et al. (2015). Astrocyte uncoupling as a cause of human temporal lobe epilepsy. Brain *138*, 1208–1222.

Beltramo, R., D'Urso, G., Dal Maschio, M., Farisello, P., Bovetti, S., Clovis, Y., Lassi, G., Tucci, V., De Pietri Tonelli, D., and Fellin, T. (2013). Layer-specific excitatory circuits differentially control recurrent network dynamics in the neocortex. Nat. Neurosci. *16*, 227–234.

Benucci, A., Frazor, R. a, and Carandini, M. (2007). Standing waves and traveling waves distinguish two circuits in visual cortex. Neuron *55*, 103–117.

Blume, W.T., Wiebe, S., and Tapsell, L.M. (2005). Occipital epilepsy: Lateral versus mesial. Brain *128*, 1209–1225.

Bock, D.D., Lee, W.-C.A., Kerlin, A.M., Andermann, M.L., Hood, G., Wetzel, A.W., Yurgenson, S., Soucy, E.R., Kim, H.S., and Reid, R.C. (2011). Network anatomy and in vivo physiology of visual cortical neurons. Nature *471*, 177–182.

Bonin, V., Histed, M.H., Yurgenson, S., and Reid, R.C. (2011). Local diversity and fine-scale organization of receptive fields in mouse visual cortex. J. Neurosci. *31*, 18506–18521.

Bouchard, M.B., Chen, B.R., Burgess, S. a, and Hillman, E.M.C. (2009). Ultra-

fast multispectral optical imaging of cortical oxygenation, blood flow, and intracellular calcium dynamics. Opt. Express *17*, 15670–15678.

Bower, M.R., Stead, M., Meyer, F.B., Marsh, W.R., and Worrell, G.A. (2012). Spatiotemporal neuronal correlates of seizure generation in focal epilepsy. *53*, 807–816.

Brown, S.P., and Hestrin, S. (2009). Intracortical circuits of pyramidal neurons reflect their long-range axonal targets. Nature *457*, 1133–1136.

Burgess, C.P., Lak, A., Steinmetz, N.A., Zatka-Haas, P., Bai Reddy, C., Jacobs, E.A.K., Linden, J.F., Paton, J.J., Ranson, A., Schröder, S., et al. (2017). High-Yield Methods for Accurate Two-Alternative Visual Psychophysics in Head-Fixed Mice. Cell Rep. *20*, 2513–2524.

Busse, L., Ayaz, A., Dhruv, N.T., Katzner, S., Saleem, A.B., Schölvinck, M.L., Zaharia, A.D., and Carandini, M. (2011). The detection of visual contrast in the behaving mouse. J. Neurosci. *31*, 11351–11361.

Carandini, M., and Churchland, A.K. (2013). Probing perceptual decisions in rodents. Nat. Publ. Gr. *16*, 824–831.

Carandini, M., and Heeger, D. (2012). Normalization as a canonical neural computation.

Carandini, M., Demb, J.B., Mante, V., Tolhurst, D.J., Dan, Y., Olshausen, B. a, Gallant, J.L., and Rust, N.C. (2005). Do we know what the early visual system does? J. Neurosci. *25*, 10577–10597.

Carandini, M., Shimaoka, D., Rossi, L.F., Sato, T.K., Benucci, X., Kno, X.T., Benucci, A., and Knopfel, T. (2015). Imaging the Awake Visual Cortex with a Genetically Encoded Voltage Indicator. J. Neurosci. *35*, 53–63.

Carmignoto, G., and Haydon, P.G. (2012). Astrocyte calcium signaling and epilepsy. Glia *60*, 1227–1233.

Cavanaugh, J.R. (2002). Nature and Interaction of Signals From the Receptive Field Center and Surround in Macaque V1 Neurons. J. Neurophysiol. *88*, 2530–2546.

Cendes, F., Cook, M.J., Watson, C., Andermann, F., Fish, D.R., Shorvon, S.D., Bergin, P., Free, S., Dubeau, F., and Arnold, D.L. (1995). Frequency and characteristics of dual pathology in patients with lesional epilepsy. Neurology *45*, 2058–2064.

Chan, K.Y., Jang, M.J., Yoo, B.B., Greenbaum, A., Ravi, N., Wu, W., Sánchez-guardado, L., Lois, C., Mazmanian, S.K., Deverman, B.E., et al. (2017). Engineered

adeno-associated viruses for efficient and noninvasive gene delivery throughout the central and peripheral nervous systems. Nat. Publ. Gr. *20*, 1–30.

Charles, A.C., and Baca, S.M. (2013). Cortical spreading depression and migraine. Nat. Rev. Neurol. *9*, 637–644.

Chen, T.-W., Wardill, T.J., Sun, Y., Pulver, S.R., Renninger, S.L., Baohan, A., Schreiter, E.R., Kerr, R.A., Orger, M.B., Jayaraman, V., et al. (2013). Ultrasensitive fluorescent proteins for imaging neuronal activity. Nature *499*, 295–300.

Chervin, R.D., Pierce, P. a, and Connors, B.W. (1988). Periodicity and directionality in the propagation of epileptiform discharges across neocortex. J. Neurophysiol. *60*, 1695–1713.

Ciabatti, E., Gonza, A., Mariotti, L., Morgese, F., and Tripodi, M. (2017). Life-Long Genetic and Functional Access to Neural Circuits Using Self-Inactivating Rabies Virus. Cell *170*, 1–11.

Cossell, L., Iacaruso, M.F., Muir, D.R., Houlton, R., Sader, E.N., Ko, H., Hofer, S.B., and Mrsic-flogel, T.D. (2015). Functional organization of excitatory synaptic strength in primary visual cortex. Nature.

Cruz-Martín, A., El-danaf, R.N., Osakada, F., Sriram, B., Dhande, O.S., Nguyen, P.L., Callaway, E.M., Ghosh, A., Huberman, A.D., Cruz-martı, A., et al. (2014). A dedicated circuit links direction-selective retinal ganglion cells to the primary visual cortex. Nature *507*, 358–361.

De Curtis, M., and Avanzini, G. (2001). Interictal spikes in focal epileptogenesis. Prog. Neurobiol. *63*, 541–567.

Dana, H., Mohar, B., Sun, Y., Narayan, S., Gordus, A., Hasseman, J.P., Tsegaye, G., Holt, G.T., Hu, A., Walpita, D., et al. (2016). Sensitive red protein calcium indicators for imaging neural activity. Elife *5*, e12727.

Daniel, A.G.S., Laffont, P., Zhao, M., Ma, H., and Schwartz, T.H. (2015). Optical electrocorticogram (OECoG) using wide-field calcium imaging reveals the divergence of neuronal and glial activity during acute rodent seizures. Epilepsy Behav. *49*, 61–65.

DeBruin, K.A., and Krassowska, W. (1999). Modeling Electroporation in a Single Cell. I. Effects of Field Strength and Rest Potential. Biophys. J. *77*, 1213–1224.

Denk, W., Strickler, J., and Webb, W. (1990). Two-photon laser scanning fluorescence microscopy. Science (80-.). *248*, 73–76.

Douglas, R.J., and Martin, K.A.C. (2004). Neuronal Circuits of the Neocortex.

Annu. Rev. Neurosci. *27*, 419–451.

Drager, U.C. (1975). Receptive fields of single cells and topography in mouse visual cortex. J. Comp. Neurol. *160*, 269–290.

England, M.J., Liverman, C.T., Schultz, A.M., and Strawbridge, L.M. (2012). Epilepsy across the spectrum: Promoting health and understanding. A summary of the Institute of Medicine report. Epilepsy Behav. *25*, 266–276.

Farkas, E., Pratt, R., Sengpiel, F., and Obrenovitch, T.P. (2008). Direct, Live Imaging of Cortical Spreading Depression and Anoxic Depolarisation Using a Fluorescent, Voltage-Sensitive Dye. J. Cereb. Blood Flow Metab. *28*, 251–262.

Feng, L.L., Zhao, T., and Kim, J. (2014). neuTube 1.0: A New Design for Efficient Neuron Reconstruction Software Based on the SWC Format. eNeuro 1–10.

Garrett, M.E., Nauhaus, I., Marshel, J.H., Callaway, X.E.M., and Callaway, E.M. (2014). Topography and Areal Organization of Mouse Visual Cortex. J. Neurosci. *34*, 12587–12600.

Georgopoulos, A.P., Schwartz, A.B., and Kettner, R.E. (1986). Neural population coding of movement direction. Science (80-.). *233*, 1416–1419.

Glickfeld, L.L., Andermann, M.L., Bonin, V., and Reid, R.C. (2013). Cortico-cortical projections in mouse visual cortex are functionally target specific. Nat. Neurosci. *16*, 219–226.

Göbel, W., Kampa, B.M., and Helmchen, F. (2007). Imaging cellular network dynamics in three dimensions using fast 3D laser scanning. Nat. Methods *4*, 73–79.

Goldensohn, E.S., Zablow, L., and Salazar, A. (1977). The penicillin focus. I. Distribution of potential at the cortical surface. Electroencephalogr. Clin. Neurophysiol. *42*, 480–492.

Goldey, G.J., Roumis, D.K., Glickfeld, L.L., Kerlin, A.M., Reid, R.C., Bonin, V., and Andermann, M.L. (2014). Versatile cranial window strategies for long-term two-photon imaging in awake mice. Nat. Protoc. *9*, 2515–2538.

Gómez-Gonzalo, M., Losi, G., Chiavegato, A., Zonta, M., Cammarota, M., Brondi, M., Vetri, F., Uva, L., Pozzan, T., de Curtis, M., et al. (2010). An excitatory loop with astrocytes contributes to drive neurons to seizure threshold. PLoS Biol. *8*.

Goodfellow, M., Rummel, C., Abela, E., Richardson, M.P., Schindler, K., and Terry, J.R. (2016). Estimation of brain network ictogenicity predicts outcome from

epilepsy surgery. Sci. Rep. *6*, 1–13.

Goodkin, H.P. (2005). Status Epilepticus Increases the Intracellular Accumulation of GABAA Receptors. J. Neurosci. *25*, 5511–5520.

Gorski, J. a, Talley, T., Qiu, M., Puelles, L., Rubenstein, J.L.R., and Jones, K.R. (2002). Cortical excitatory neurons and glia, but not GABAergic neurons, are produced in the Emx1-expressing lineage. J. Neurosci. *22*, 6309–6314.

Grienberger, C., and Konnerth, A. (2012). Imaging Calcium in Neurons. Neuron *73*, 862–885.

Guizar-Sicairos, M., Thurman, S.T., and Fienup, J.R. (2008). Efficient subpixel image registration algorithms. Opt. Lett. *33*, 156–158.

Gyengesi, G.Z., Hermesz, E., Ks, A., and Szente M (2003). Involvement of Gap Junctions in the Manifestation and Control of the Duration of Seizures in Rats In Vivo. Epilepsia *44*, 1596–1600.

Haglund, M.M. (2012). Optical imaging of visual cortex epileptic foci and propagation pathways. Epilepsia *53*, 87–97.

Haider, B., Häusser, M., and Carandini, M. (2013). Inhibition dominates sensory responses in the awake cortex. Nature *493*, 97–100.

Han, Y., and Mrsic-flogel, T. (2013). A finely tuned cortical amplifier. Nat. Neurosci. *16*, 1166–1168.

Hanks, T.D., Kopec, C.D., Brunton, B.W., Duan, C.A., Erlich, J.C., and Brody, C.D. (2015). Distinct relationships of parietal and prefrontal cortices to evidence accumulation. Nature *520*, 220–223.

Harris, K.D. (2012). Cell assemblies of the superficial cortex. Neuron *76*, 263–265.

Harris, K.D., and Mrsic-Flogel, T.D. (2013). Cortical connectivity and sensory coding. Nature *503*, 51–58.

Harris, K.D., and Shepherd, G.M.G. (2015). The neocortical circuit: themes and variations. Nat. Neurosci. *18*, 170–181.

Harris, K.D., and Thiele, A. (2011). Cortical state and attention. Nat. Rev. Neurosci. *12*, 509–523.

Hartline, H.K. (1937). The response of single optic nerve fibers of the vertebrate eye to illumination of the retina. Am. J. Physiol. 400–415.

Harvey, C.D., Coen, P., and Tank, D.W. (2012). Choice-specific sequences in parietal cortex during a virtual-navigation decision task. Nature *484*, 62–68.

Helmchen, F., Imoto, K., and Sakmann, B. (1996). Ca2+ buffering and action potential-evoked Ca2+ signaling in dendrites of pyramidal neurons. Biophys. J. *70*, 1069–1081.

Hillier, D., Fiscella, M., Drinnenberg, A., Trenholm, S., Rompani, S.B., Raics, Z., Katona, G., Juettner, J., Hierlemann, A., Rozsa, B., et al. (2017). Causal evidence for retina-dependent and -independent visual motion computations in mouse cortex. Nat. Neurosci. *20*.

Hofer, S.B., Ko, H., Pichler, B., Vogelstein, J., Ros, H., Zeng, H., Lein, E., Lesica, N. a, and Mrsic-Flogel, T.D. (2011). Differential connectivity and response dynamics of excitatory and inhibitory neurons in visual cortex. Nat. Neurosci. *14*, 1045–1052.

Van Hooser, S.D. (2007). Similarity and diversity in visual cortex: is there a unifying theory of cortical computation? Neurosci. *13*, 639–656.

Horton, J.C., and Adams, D.L. (2005). The cortical column: a structure without a function. Philos. Trans. R. Soc. B Biol. Sci. *360*, 837–862.

Huang, X., Xu, W., Liang, J., Takagaki, K., Gao, X., and Wu, J. young (2010). Spiral Wave Dynamics in Neocortex. Neuron *68*, 978–990.

Hubel, D.H., and Wiesel, T.N. (1962). Receptive fields, binocular interaction and functional architecture in the cat's visual cortex. J. Physiol. *160*, 106–154.

Hübener, M. (2003). Mouse visual cortex. Curr. Opin. Neurobiol. *13*, 413–420.

Huberfeld, G., Wittner, L., Clemenceau, S., Baulac, M., Kaila, K., Miles, R., and Rivera, C. (2007). Perturbed chloride homeostasis and GABAergic signaling in human temporal lobe epilepsy. J. Neurosci. *27*, 9866–9873.

Huberfeld, G., Menendez de la Prida, L., Pallud, J., Cohen, I., Le Van Quyen, M., Adam, C., Clemenceau, S., Baulac, M., and Miles, R. (2011). Glutamatergic pre-ictal discharges emerge at the transition to seizure in human epilepsy. Nat. Neurosci. *14*, 627–634.

Iacaruso, M.F., Gasler, I.T., and Hofer, S.B. (2017). Synaptic organization of visual space in primary visual cortex. Nature.

Ji, N., Freeman, J., and Smith, S.L. (2016). Technologies for imaging neural activity in large volumes. Nat. Neurosci. *19*, 1154–1164.

Jia, H., Rochefort, N.L., Chen, X., and Konnerth, A. (2010). Dendritic organization of sensory input to cortical neurons in vivo. Nature *464*, 1307–1312.

Jiang, X., Shen, S., Cadwell, C.R., Berens, P., Sinz, F., Ecker, a. S., Patel, S., and

Tolias, a. S. (2015). Principles of connectivity among morphologically defined cell types in adult neocortex. Science (80-.). *350*, aac9462-aac9462.

Juavinett, A.L., and Callaway, E.M. (2015). Pattern and Component Motion Responses in Mouse Visual Cortical Areas. Curr. Biol. *25*, 1759–1764.

Judkewitz, B., Rizzi, M., Kitamura, K., and Häusser, M. (2009). Targeted single-cell electroporation of mammalian neurons in vivo. Nat. Protoc. *4*, 862–869.

Kalatsky, V. a, and Stryker, M.P. (2003). New paradigm for optical imaging: temporally encoded maps of intrinsic signal. Neuron *38*, 529–545.

Kaschube, M. (2014). Neural maps versus salt-and-pepper organization in visual cortex. Curr. Opin. Neurobiol. *24*, 95–102.

Kätzel, D., Nicholson, E., Schorge, S., Walker, M.C., and Kullmann, D.M. (2014). Chemical–genetic attenuation of focal neocortical seizures. Nat. Commun. *5*.

Kim, E.J., Juavinett, A.L., Kyubwa, E.M., Jacobs, M.W., and Callaway, E.M. (2015). Three Types of Cortical Layer 5 Neurons That Differ in Brain-wide Connectivity and Function. Neuron *88*, 1253–1267.

Kim, E.J., Jacobs, M.W., Ito-cole, T., and Callaway, E.M. (2016). Improved Monosynaptic Neural Circuit Tracing Using Engineered Rabies Virus Glycoproteins. CellReports *15*, 1–8.

Kim, M.-H., Znamenskiyn, P., Iacaruso, M.F., and Mrsic-Flogel, T.D. (2017). Exclusive functional subnetworks of intracortical projections neurons in primary visual cortex. bioRxiv (Unpublished).

Kitamura, K., Judkewitz, B., Kano, M., Denk, W., and Ha, M. (2008). Targeted patch-clamp recordings and single-cell electroporation of unlabeled neurons in vivo. *5*, 61–67.

Kleen, J.K., Scott, R.C., Holmes, G.L., Roberts, D.W., Rundle, M.M., Testorf, M., Lenck-Santini, P.P., and Jobst, B.C. (2013). Hippocampal interictal epileptiform activity disrupts cognition in humans. Neurology *81*, 18–24.

Ko, H., Hofer, S.B., Pichler, B., Buchanan, K. a, Sjöström, P.J., and Mrsic-Flogel, T.D. (2011). Functional specificity of local synaptic connections in neocortical networks. Nature *473*, 87–91.

Ko, H., Cossell, L., Baragli, C., Antolik, J., Clopath, C., Hofer, S.B., and Mrsic-Flogel, T.D. (2013). The emergence of functional microcircuits in visual cortex. Nature *496*, 96–100.

Koester, H.J., and Sakmann, B. (2000). Calcium dynamics associated with action potentials in single nerve terminals of pyramidal cells in layer 2/3 of the young rat neocortex. J. Physiol. *529*.

Kondo, S., and Ohki, K. (2015). Laminar differences in the orientation selectivity of geniculate afferents in mouse primary visual cortex. Nat. Neurosci. *19*, 1–6.

Kondo, S., Yoshida, T., and Ohki, K. (2016). Mixed functional microarchitectures for orientation selectivity in the mouse primary visual cortex. Nat. Commun. *7*, 13210.

Kremkow, J., Jin, J., Wang, Y., and Alonso, J.M. (2016). Principles underlying sensory map topography in primary visual cortex. Nature *533*, 52–57.

Krook-Magnuson, E., and Soltesz, I. (2015). Beyond the hammer and the scalpel: selective circuit control for the epilepsies. Nat. Neurosci. *18*, 331–338.

Krook-Magnuson, E., Armstrong, C., Oijala, M., and Soltesz, I. (2013). On-demand optogenetic control of spontaneous seizures in temporal lobe epilepsy. Nat. Commun. *4*, 1376.

Lawn, N.D., Bamlet, W.R., Radhakrishnan, K., O'Brien, P.C., and So, E.L. (2004). Injuries due to seizures in persons with epilepsy: A population-based study. Neurology *63*, 1565–1570.

Laxer, K.D., Trinka, E., Hirsch, L.J., Cendes, F., Langfitt, J., Delanty, N., Resnick, T., and Benbadis, S.R. (2014). The consequences of refractory epilepsy and its treatment. Epilepsy Behav. *37*, 59–70.

Lee, W.-C.A., Bonin, V., Reed, M., Graham, B.J., Hood, G., Glattfelder, K., and Reid, R.C. (2016). Anatomy and function of an excitatory network in the visual cortex. Nature *532*, 1–18.

Lien, A.D., and Scanziani, M. (2013). Tuned thalamic excitation is amplified by visual cortical circuits. Nat. Neurosci. *16*, 1315–1323.

Lin, M.Z., and Schnitzer, M.J. (2016). Genetically encoded indicators of neuronal activity. Nat. Neurosci. *19*, 1142–1153.

Liou, A.J., Ma, H., Wenzel, M., Zhao, M., Baird-daniel, E., and Schevon, C.A. (2017). Role of inhibitory control in modulating spread of focal ictal activity. bioRxiv (Unpublished).

Losi, G., Mariotti, L., Sessolo, M., and Carmignoto, G. (2017). New Tools to Study Astrocyte Ca2+ Signal Dynamics in Brain Networks In Vivo. Front. Cell. Neurosci. *11*, 1–7.

Luczak, A., Barthó, P., and Harris, K.D. (2009). Spontaneous events outline the realm of possible sensory responses in neocortical populations. Neuron *62*, 413–425.

Madisen, L., Garner, A.R., Shimaoka, D., Chuong, A.S., Klapoetke, N.C., Li, L., van der Bourg, A., Niino, Y., Egolf, L., Monetti, C., et al. (2015). Transgenic Mice for Intersectional Targeting of Neural Sensors and Effectors with High Specificity and Performance. Neuron *85*, 942–958.

Maravall, M., Mainen, Z.F., Sabatini, B.L., and Svoboda, K. (2000). Estimating intracellular calcium concentrations and buffering without wavelength ratioing. Biophys. J. *78*, 2655–2667.

Marshel, J.H., Mori, T., Nielsen, K.J., and Callaway, E.M. (2010). Targeting single neuronal networks for gene expression and cell labeling in vivo. Neuron *67*, 562–574.

Marshel, J.H., Garrett, M.E., Nauhaus, I., and Callaway, E.M. (2011). Functional specialization of seven mouse visual cortical areas. Neuron *72*, 1040–1054.

Martin, K.A.C., and Schroder, S. (2013). Functional Heterogeneity in Neighboring Neurons of Cat Primary Visual Cortex in Response to Both Artificial and Natural Stimuli. J. Neurosci. *33*, 7325–7344.

Martinez, L.M., and Alonso, J.-M. (2003). Complex Receptive Fields in Primary VIsual Cortex. Neuroscientist.

Marvin, J.S., Borghuis, B.G., Tian, L., Cichon, J., Harnett, M.T., Akerboom, J., Gordus, A., Renninger, S.L., Chen, T.-W., Bargmann, C.I., et al. (2013). An optimized fluorescent probe for visualizing glutamate neurotransmission. Nat. Methods *10*, 162–170.

McCormick, D.A., and Contreras, D. (2001). On the cellular and network bases of epileptic seizures. Ann. Rev. Physiol.

Mechler, F., and Ringach, D.L. (2002). On the classification of simple and complex cells. Vision Res. *42*, 1017–1033.

Merricks, E.M., Smith, E.H., McKhann, G.M., Goodman, R.R., Bateman, L.M., Emerson, R.G., Schevon, C.A., and Trevelyan, A.J. (2015). Single unit action potentials in humans and the effect of seizure activity. Brain *138*, 2891–2906.

Mitra, P., and Bokil, H. (2008). Observed Brain Dynamics.

Mohajerani, M.H., Chan, A.W., Mohsenvand, M., LeDue, J., Liu, R., Mcvea, D.A., Boyd, J.D., Wang, Y.T., Reimers, M., and Murphy, T.H. (2013). Spontaneous

cortical activity alternates between motifs defined by regional axonal projections. Nat. Neurosci. *16*, 1426–1435.

Mooser, F., Bosking, W.H., and Fitzpatrick, D. (2004). A morphological basis for orientation tuning in primary visual cortex. Nat. Neurosci. *7*, 872–879.

Motelow, J.E., Li, W., Zhan, Q., Mishra, A.M., Sachdev, R.N.S., Liu, G., Gummadavelli, A., Zayyad, Z., Lee, H.S., Chu, V., et al. (2015). Decreased subcortical cholinergic arousal in focal seizures. Neuron *85*, 561–572.

Mountcastle, V. (1956). Modality and topographic properties of single neurons of cat's somatic sensory cortex. J. Physiol.

Muldoon, S.F., Villette, V., Tressard, T., Malvache, A., Reichinnek, S., Bartolomei, F., and Cossart, R. (2015). GABAergic inhibition shapes interictal dynamics in awake epileptic mice. Brain *138*, 2875–2890.

Nakai, J., Ohkura, M., and Imoto, K. (2001). A high signal-to-noise Ca(2+) probe composed of a single green fluorescent protein. Nat. Biotechnol. *19*, 137–141.

Nauhaus, I., Nielsen, K.J., and Callaway, E.M. (2012). Nonlinearity of two-photon Ca2+ imaging yields distorted measurements of tuning for V1 neuronal populations. J. Neurophysiol. *107*, 923–936.

Neher, E., and Augustine, G.J. (1992). Calcium gradients and buffers in bovine chromaffin cells. J. Physiol. *450*, 273–301.

Nevian, T., and Helmchen, F. (2007). Calcium indicator loading of neurons using single-cell electroporation. Pflugers Arch. Eur. J. Physiol. *454*, 675–688.

Niell, C. (2015). Cell Types, Circuits, and Receptive Fields in the Mouse Visual Cortex. Annu. Rev. Neurosci. 413–431.

Niell, C.M., and Stryker, M.P. (2008). Highly selective receptive fields in mouse visual cortex. J. Neurosci. *28*, 7520–7536.

Niell, C.M., and Stryker, M.P. (2010). Modulation of visual responses by behavioral state in mouse visual cortex. Neuron *65*, 472–479.

O'Keefe, J., and Dostrovsky, J. (1971). The hippocampus as a spatial map. Preliminary evidence from unit activity in the freely-moving rat. Brain Res. *34*, 171–175.

Ohki, K., Chung, S., Ch'ng, Y.H., Kara, P., and Reid, R.C. (2005). Functional imaging with cellular resolution reveals precise micro-architecture in visual cortex. Nature *433*, 597–603.

Okun, M., Steinmetz, N. a., Cossell, L., Iacaruso, M.F., Ko, H., Barthó, P., Moore, T., Hofer, S.B., Mrsic-Flogel, T.D., Carandini, M., et al. (2015). Diverse coupling of neurons to populations in sensory cortex. Nature.

Osakada, F., and Callaway, E.M. (2013). Design and generation of recombinant rabies virus vectors. Nat. Protoc. *8*, 1583–1601.

Osakada, F., Mori, T., Cetin, A.H., Marshel, J.H., Virgen, B., and Callaway, E.M. (2011). New rabies virus variants for monitoring and manipulating activity and gene expression in defined neural circuits. Neuron *71*, 617–631.

Ouzounov, D.G., Wang, T., Wang, M., Feng, D.D., Horton, N.G., Cruz-Hernández, J.C., Cheng, Y., Reimer, J., Tolias, A.S., Nishimura, N., et al. (2017). In vivo three-photon imaging of activity of GCaMP6-labeled neurons deep in intact mouse brain. Nat. Methods 20–24.

Oyama, K., Ohara, S., Sato, S., Karube, F., Fujiyama, F., Isomura, Y., Mushiake, H., Iijima, T., and Tsutsui, K.-I. (2013). Long-lasting single-neuron labeling by in vivo electroporation without microscopic guidance. J. Neurosci. Methods *218*, 139–147.

Pachitariu, M., Stringer, C., Schröder, S., Dipoppa, M., Rossi, L.F., Carandini, M., and Harris, K.D. (2016). Suite2p: beyond 10,000 neurons with standard two-photon microscopy. bioRxiv 61507.

Packer, A.M., Roska, B., and Häusser, M. (2013). Targeting neurons and photons for optogenetics. Nat. Neurosci. *16*, 805–815.

Packer, A.M., Russell, L.E., Dalgleish, H.W.P., and Häusser, M. (2014). Simultaneous all-optical manipulation and recording of neural circuit activity with cellular resolution in vivo. *12*.

Payne, H.L., and Raymond, J.L. (2017). Magnetic eye tracking in mice. Elife *6*, 1–24.

Paz, J.T., and Huguenard, J.R. (2015). Microcircuits and their interactions in epilepsy: is the focus out of focus? Nat. Neurosci. *18*, 351–359.

Perin, R., Berger, T.K., and Markram, H. (2011). A synaptic organizing principle for cortical neuronal groups. Proc. Natl. Acad. Sci. U. S. A. *108*, 5419–5424.

Peron, S.P., Freeman, J., Iyer, V., Guo, C., and Svoboda, K. (2015). A Cellular Resolution Map of Barrel Cortex Activity during Tactile Behavior. Neuron *86*, 783–799.

Perucca, P., and Gilliam, F.G. (2012). Adverse effects of antiepileptic drugs.

Lancet Neurol. *11*, 792–802.

Petersen, C.C.H. (2017). Whole-Cell Recording of Neuronal Membrane Potential during Behavior. Neuron *95*, 1266–1281.

Pfeffer, C.K., Xue, M., He, M., Huang, Z.J., and Scanziani, M. (2013). Inhibition of inhibition in visual cortex: the logic of connections between molecularly distinct interneurons. Nat. Neurosci. *16*, 1068–1076.

Polack, P.-O., and Contreras, D. (2012). Long-range parallel processing and local recurrent activity in the visual cortex of the mouse. J. Neurosci. *32*, 11120–11131.

Pologruto, T.A., Sabatini, B.L., and Svoboda, K. (2003). ScanImage: flexible software for operating laser scanning microscopes. Biomed. Eng. Online *2*, 13.

Priebe, N.J. (2016). Mechanisms of Orientation Selectivity in the Primary Visual Cortex. Annu. Rev. Vis. Sci.

Priebe, N.J., Mechler, F., Carandini, M., and Ferster, D. (2004). The contribution of spike threshold to the dichotomy of cortical simple and complex cells. Nat. Neurosci. *7*, 1113–1122.

Prince, D.A., and Wilder, B.J. (1967). Control Mechanisms of Cortical Epileptogenic Foci.

Qiu, C., Shivacharan, R.S., Zhang, M., and Durand, D.M. (2015). Can Neural Activity Propagate by Endogenous Electrical Field? J. Neurosci. *35*, 15800–15811.

Rancz, E. a, Franks, K.M., Schwarz, M.K., Pichler, B., Schaefer, A.T., and Margrie, T.W. (2011). Transfection via whole-cell recording in vivo: bridging single-cell physiology, genetics and connectomics. Nat. Neurosci. *14*, 527–532.

Ratzlaff, E.H., and Grinvald, A. (1991). A tandem-lens epifluorescence macroscope: Hundred-fold brightness advantage for wide-field imaging. J. Neurosci. Methods *36*, 127–137.

Reid, R.C. (2012). From functional architecture to functional connectomics. Neuron *75*, 209–217.

Reimer, J., Froudarakis, E., Cadwell, C.R., Yatsenko, D., Denfield, G.H., and Tolias, A.S. (2014). Pupil Fluctuations Track Fast Switching of Cortical States during Quiet Wakefulness. Neuron *84*, 355–362.

Reimer, J., McGinley, M.J., Liu, Y., Rodenkirch, C., Wang, Q., McCormick, D.A., and Tolias, A.S. (2016). Pupil fluctuations track rapid changes in adrenergic and cholinergic activity in cortex. Nat. Commun. *7*, 13289.

Rossi, L.F., Harris K.D., Carandini, M. Functional organization of presynaptic networks in primary visual cortex. Program No. 402.14. 2017 Neuroscience Meeting Planner. Washington, DC: Society for Neuroscience, 2017. Online.

Rossi, L.F., Wykes, R.C., Kullmann, D.M., and Carandini, M. (2017). Focal cortical seizures start as standing waves and propagate respecting homotopic connectivity. Nat. Commun. *1*, 217.

Rossi, L.F., Kullmann, D.M., Carandini, M., and Wykes, R, Widefield imaging of sensory and epileptiform activity in mouse visual cortex. Program No. 419.04. 2014 Neuroscience Meeting Planner. Washington, DC: Society for Neuroscience, 2014. Online.

Rossi, L.F., Shimaoka, D., Sato, T., Knöpfel, T., Carandini, M., and Benucci, A. Imaging visual cortex in awake mice with genetically-encoded voltage and calcium indicators. Program No. 359.06. 2013 Neuroscience Meeting Planner. San Diego, CA: Society for Neuroscience, 2013. Online.

Schevon, C. a, Weiss, S. a, McKhann, G., Goodman, R.R., Yuste, R., Emerson, R.G., and Trevelyan, A.J. (2012). Evidence of an inhibitory restraint of seizure activity in humans. Nat. Commun. *3*, 1060.

Schindelin, J., Arganda-Carreras, I., Frise, E., Kaynig, V., Longair, M., Pietzsch, T., Preibisch, S., Rueden, C., Saalfeld, S., Schmid, B., et al. (2012). Fiji: an open-source platform for biological-image analysis. Nat. Methods *9*, 676–682.

Schwartz, T.H. (2003). Optical Imaging of Epileptiform Events in Visual Cortex in Response to Patterned Photic Stimulation. Cereb. Cortex *13*, 1287–1298.

Schwartz, T.H., and Bonhoeffer, T. (2001). In vivo optical mapping of epileptic foci and surround inhibition in ferret cerebral cortex. Nat. Med. *7*, 1063–1067.

Sessolo, M., Marcon, I., Bovetti, S., Losi, G., Cammarota, M., Ratto, G.M., Fellin, T., and Carmignoto, G. (2015). Parvalbumin-Positive Inhibitory Interneurons Oppose Propagation But Favor Generation of Focal Epileptiform Activity. J. Neurosci. *35*, 9544–9557.

Sherrington, C.S. (1906). Observations on the scratch-reflex in the spinal dog. J. Physiol. *34*, 1–50.

Skottun, B.C., De Valois, R.L., Grosof, D.H., Movshon, J.A., Albrecht, D.G., and Bonds, A.B. (1991). Classifying simple and complex cells on the basis of response modulation. Vision Res. *31*, 1079–1086.

Smith, S.L., and Häusser, M. (2010). Parallel processing of visual space by neighboring neurons in mouse visual cortex. Nat. Neurosci. *13*, 1144–1149.

Smith, E.H., Liou, J., Davis, T.S., Merricks, E.M., Kellis, S.S., Weiss, S.A., Greger, B., House, P.A., McKhann II, G.M., Goodman, R.R., et al. (2016). The ictal wavefront is the spatiotemporal source of discharges during spontaneous human seizures. Nat. Commun. *7*, 11098.

Song, S., Sjöström, P.J., Reigl, M., Nelson, S., and Chklovskii, D.B. (2005). Highly nonrandom features of synaptic connectivity in local cortical circuits. PLoS Biol. *3*, e68.

Sorokin, J.M., Davidson, T.J., Frechette, E., Abramian, A.M., Deisseroth, K., Huguenard, J.R., and Paz, J.T. (2016). Bidirectional Control of Generalized Epilepsy Networks via Rapid Real-Time Switching of Firing Mode. Neuron *93*, 194–210.

Staley, K.J., Soldo, B.L., and Proctor, W.R. (1995). Ionic mechanisms of neuronal excitation by inhibitory GABAA receptors. Sci. (New York, NY) *269*, 977–981.

Staley, K.J., White, A., and Dudek, F.E. (2011). Interictal spikes: Harbingers or causes of epilepsy? Neurosci. Lett. *497*, 247–250.

Steriade, M., and Contreras, D. (1998). Spike-Wave Complexes and Fast Components of Cortically Generated Seizures . I . Role of Neocortex and Thalamus. J Neurophysiol 1439–1455.

Sun, W., Tan, Z., Mensh, B.D., and Ji, N. (2015). Thalamus provides layer 4 of primary visual cortex with orientation- and direction-tuned inputs. Nat. Neurosci. *19*, 308–315.

Svoboda, K., and Yasuda, R. (2006). Principles of Two-Photon Excitation Microscopy and Its Applications to Neuroscience. Neuron *50*, 823–839.

Szabo, G.G., Schneider, C.J., and Soltesz, I. (2015). Resolution revolution: Epilepsy dynamics at the microscale. Curr. Opin. Neurobiol. *31*, 239–243.

Teruel, M.N., and Meyer, T. (1997). Electroporation-induced formation of individual calcium entry sites in the cell body and processes of adherent cells. Biophys. J. *73*, 1785–1796.

Thomson, A.M., and Lamy, C. (2007). Functional maps of neocortical local circuitry. Front. Neurosci. *1*, 19–42.

Tian, L., Hires, S.A., Mao, T., Huber, D., Chiappe, M.E., Chalasani, S.H., Petreanu, L., Akerboom, J., McKinney, S. a, Schreiter, E.R., et al. (2009). Imaging

neural activity in worms, flies and mice with improved GCaMP calcium indicators. Nat. Methods *6*, 875–881.

Trevelyan, A.J., Sussillo, D., Watson, B.O., and Yuste, R. (2006). Modular propagation of epileptiform activity: evidence for an inhibitory veto in neocortex. J. Neurosci. *26*, 12447–12455.

Trevelyan, A.J., Sussillo, D., and Yuste, R. (2007). Feedforward inhibition contributes to the control of epileptiform propagation speed. J. Neurosci. *27*, 3383–3387.

Truccolo, W., Donoghue, J. a, Hochberg, L.R., Eskandar, E.N., Madsen, J.R., Anderson, W.S., Brown, E.N., Halgren, E., and Cash, S.S. (2011). Single-neuron dynamics in human focal epilepsy. Nat. Neurosci. *14*, 635–641.

Tsodyks, M., Kenet, T., Grinvald, A., and Arieli, A. (1999). Linking Spontaneous Activity of Single Cortical Neurons and the Underlying Functional Architecture. *286*, 1943–1947.

Vanni, M.P., and Murphy, T.H. (2014). Mesoscale Transcranial Spontaneous Activity Mapping in GCaMP3 Transgenic Mice Reveals Extensive Reciprocal Connections between Areas of Somatomotor Cortex. J. Neurosci. *34*, 15931–15946.

Vélez-Fort, M., Rousseau, C.V., Niedworok, C.J., Wickersham, I.R., Rancz, E.A., Brown, A.P.Y., Strom, M., and Margrie, T.W. (2014). The Stimulus Selectivity and Connectivity of Layer Six Principal Cells Reveals Cortical Microcircuits Underlying Visual Processing. Neuron 1–13.

Viventi, J., Kim, D.-H., Vigeland, L., Frechette, E.S., Blanco, J. a, Kim, Y.-S., Avrin, A.E., Tiruvadi, V.R., Hwang, S.-W., Vanleer, A.C., et al. (2011). Flexible, foldable, actively multiplexed, high-density electrode array for mapping brain activity in vivo. Nat. Neurosci. *14*, 1599–1605.

Vogelstein, J.T., Packer, A.M., Machado, T. a, Sippy, T., Babadi, B., Yuste, R., and Paninski, L. (2010). Fast nonnegative deconvolution for spike train inference from population calcium imaging. J. Neurophysiol. *104*, 3691–3704.

Voipio, J., and Kaila, K. (2000). GABAergic excitation and K+-mediated volume transmission in the hippocampus. Prog. Brain Res. *125*, 329–338.

Wadman, W.J., and Gutnick, M.J. (1993). Non-uniform propagation of epileptiform discharge in brain slices of rat neocortex. Neuroscience *52*, 255–262.

Walczak, T.S., Leppik, I.E., D'Amelio, M., Rarick, J., So, E., Ahman, P., Ruggles, K., Cascino, G.D., Annegers, J.F., and Hauser, W. a (2001). Incidence and risk

factors in sudden unexpected death in epilepsy: a prospective cohort study. Neurology *56*, 519–525.

Wang, X.J. (2012). Neural dynamics and circuit mechanisms of decision-making. Curr. Opin. Neurobiol. *22*, 1039–1046.

Wang, Q., and Burkhalter, A. (2007). Area Map of Mouse Visual Cortex. *357*, 339–357.

Wekselblatt, J.B., Flister, E.D., Piscopo, D.M., and Niell, C.M. (2016). Large-scale imaging of cortical dynamics during sensory perception and behavior. J. Neurophysiol. jn.01056.2015.

Wenzel, M., Hamm, J.P., Peterka, D.S., and Yuste, R. (2017). Reliable and Elastic Propagation of Cortical Seizures In Vivo. Cell Rep. *19*, 2681–2693.

Wertz, A., Trenholm, S., Yonehara, K., Hillier, D., Raics, Z., Leinweber, M., Szalay, G., Ghanem, A., Keller, G., Rózsa, B., et al. (2015). PRESYNAPTIC NETWORKS: Single-cell–initiated monosynaptic tracing reveals layer-specific cortical network modules. Science (80-.). *349*.

Wickersham, I.R., Lyon, D.C., Barnard, R.J.O., Mori, T., Finke, S., Conzelmann, K.-K., Young, J. a T., and Callaway, E.M. (2007a). Monosynaptic restriction of transsynaptic tracing from single, genetically targeted neurons. Neuron *53*, 639–647.

Wickersham, I.R., Finke, S., Conzelmann, K.-K., and Callaway, E.M. (2007b). Retrograde neuronal tracing with a deletion-mutant rabies virus. Nat. Methods *4*, 47–49.

Wiebe, S., and Jette, N. (2012). Pharmacoresistance and the role of surgery in difficult to treat epilepsy. Nat. Rev. Neurol. *8*, 669–677.

Wykes, R.C., Heeroma, J.H., Mantoan, L., Zheng, K., Schorge, S., Kullmann, D.M., MacDonald, D.C., Deisseroth, K., Hashemi, K.S., Walker, M.C., et al. (2012). Optogenetic and potassium channel gene therapy in a rodent model of focal neocortical epilepsy. Sci. Transl. Med. *4*, 161ra152.

Xiao, D., Vanni, M.P., Mitelut, C.C., Chan, A.W., Ledue, J.M., Xie, Y., Chen, A.C.N., Swindale, N. V., and Murphy, T.H. (2017). Mapping cortical mesoscopic networks of single spiking cortical or sub-cortical neurons. Elife *6*, 1–28.

Ya-tang, L., Leena, I., Bao-hua, L., Li, Z., and Tao, H. (2013). Linear Transformation of Thalamocortical input by Intracortical Excitation. Nat. Neurosci. *14*, 1–14.

Yasuda, R., Nimchinsky, E. a, Scheuss, V., Pologruto, T. a, Oertner, T.G.,

Sabatini, B.L., and Svoboda, K. (2004). Imaging calcium concentration dynamics in small neuronal compartments. Sci. STKE *2004*, pl5.

Yoo, J.Y., Farooque, P., Chen, W.C., Youngblood, M.W., Zaveri, H.P., Gerrard, J.L., Spencer, D.D., Hirsch, L.J., and Blumenfeld, H. (2014). Ictal spread of medial temporal lobe seizures with and without secondary generalization: An intracranial electroencephalography analysis. Epilepsia *55*, 289–295.

Yoshimura, Y., and Callaway, E.M. (2005). Fine-scale specificity of cortical networks depends on inhibitory cell type and connectivity. Nat. Neurosci. *8*, 1552–1559.

Yoshimura, Y., Dantzker, J., and Callaway, E. (2005). Excitatory cortical neurons form fine-scale functional networks. Nature *433*.

Zariwala, H.A., Borghuis, B.G., Hoogland, T.M., Madisen, L., Tian, L., De Zeeuw, C.I., Zeng, H., Looger, L.L., Svoboda, K., and Chen, T.W. (2012). A Cre-dependent GCaMP3 reporter mouse for neuronal imaging in vivo. J Neurosci *32*, 3131–3141.

Zeng, H., and Sanes, J.R. (2017). Neuronal cell-type classification: challenges, opportunities and the path forward. Nat. Rev. Neurosci. *18*, 530–546.

Zhang, M., Ladas, T.P., Qiu, C., Shivacharan, R.S., Gonzalez-Reyes, L.E., and Durand, D.M. (2014). Propagation of epileptiform activity can be independent of synaptic transmission, gap junctions, or diffusion and is consistent with electrical field transmission. J. Neurosci. *34*, 1409–1419.

Zhuang, J., Ng, L., Williams, D., Valley, M., Li, Y., Garrett, M., and Waters, J. (2017). An extended retinotopic map of mouse cortex. Elife *6*, 1–29.

Ziburkus, J., Cressman, J.R., Barreto, E., and Schiff, S.J. (2006). Interneuron and pyramidal cell interplay during in vitro seizure-like events. J. Neurophysiol. *95*, 3948–3954.